STUDIES ON *IN-SITU* PARTICULATE REINFORCED Sn-Ag COMPOSITE SOLDERS RELEVANT TO THERMOMECHANICAL FATIGUE ISSUES

By

SUNGLAK CHOI

A DISSERTATION

Submitted to
Michigan State University
in partial fulfillment of the requirements
for the degree of

DOCTOR OF PHILOSOPHY

Department of Chemical Engineering and Materials Science

2001

ABSTRACT

STUDIES ON *IN-SITU* PARTICULATE REINFORCED Sn-Ag COMPOSITE SOLDERS RELEVANT TO THERMOMECHANICAL FATIGUE ISSUES

By

SUNGLAK CHOI

Global pressure based on environmental and health concerns regarding the use of Pb-bearing solder has forced the electronics industry to develop Pb-free alternative solders. Eutectic Sn-Ag solder has received much attention as a potential Pb-free candidate to replace Sn-Pb solder. Since introduction of surface mount technology, packaging density increased and the electronic devices became smaller. As a result, solders in electronic modules are forced to function as a mechanical connection as well as electrical contact. Solders are also exposed to very harsh service conditions such as automotive under-the-hood and aerospace applications.

Solder joints experience thermomechanical fatigue, i.e. interaction of fatigue and creep, during thermal cycling due to temperature fluctuation in service conditions. Microstructural study on thermomechanical fatigue of the actual eutectic Sn-Ag and Sn-4Ag-0.5Cu solder joints was performed to better understand deformation and damage accumulation occurring during service. Incorporation of reinforcements has been pursued to improve the mechanical and particularly thermomechanical behavior of solders, and their service temperature capability. *In-situ* Sn-Ag composite solders were developed by incorporating Cu_6Sn_5, Ni_3Sn_4, and $FeSn_2$ particulate reinforcements in the eutectic Sn-Ag solder in an effort to enhance thermomechanical fatigue resistance. *In-*

situ composite solders were investigated on the growth of interfacial intermetallic layer between solder and Cu substrate growth and creep properties.

Solder joints exhibited significant deformation and damage on free surface and interior regions during thermomechanical fatigue. Cracks initiated on the free surface of the solder joints and propagated toward interior regions near the substrate of the solder joint. Crack grew along Sn grain boundaries by grain boundary sliding. There was significant residual stress within the solder joint causing more damage. Presence of small amount of Cu and Pb phase resulting from Sn-Pb finish on electronic component did not affect thermomechanical fatigue deformation of the eutectic Sn-Ag solder joints.

In the aging study up to 5000 hours, solder matrix consisting of Sn phase and Ag_3Sn particles showed extensive coarsening. Intermetallic particles of Cu_6Sn_5 Ni_3Sn_4, and $FeSn_2$ particles in the eutectic Sn-Ag composite solder joints were effective in retarding the interfacial intermetallic layer growth at low temperature less than 150°C. Ni_3Sn_4 and $FeSn_2$ particles were stable during aging, whereas Cu_6Sn_5 particles exhibited coarsening.

In-situ composite solder joints exhibited different creep behavior depending on the type of incorporated particle, compared to the eutectic Sn-Ag solder joints. Cu_6Sn_5 and Ni_3Sn_4 reinforced composite solder joints showed weakening at room temperature creep, whereas composite solder joints reinforced with $FeSn_2$ particles exhibited strengthening at the same temperature. However, the creep strength of composite solder joints at high temperature of 85 and 125°C was similar to that of eutectic Sn-Ag solder joints, indicating that there is no substantial effect of particle at high temperatures. Cyclic creep by loading/unloading was found to significantly increase creep strength of solder joints.

to my father and the memory of my mother

to my wife for her assistance, endurance,
and encouragement

to Anne and soon-to-be-born son
for their ever-bright future

ACKNOWLEDGEMENTS

I would like to express my sincere appreciation to my academic advisor, Dr. Thomas R. Bieler, and co-advisors, Dr. K.N. Subramanian and Dr. J.P. Lucas, for their guidance and encouragement to complete this research.

I also wish to thank the members of my committee, Dr. Dahsin Liu, Department of Mechanical Engineering, and Dr. Phillip Duxbury, Physics and Astronomy Department, for their valuable suggestions and comments on this study.

Particularly, I would like to express my sincere appreciation to Composite Materials and Structures Center at MSU, Visteon Electronic Technical Center, Dearborn, MI, Mannesmann VDO Control System, Auburn, IN, and National Science Foundation.

I would like to express my deep gratitude to my wife for her patient support and encouragement during entire graduate study. I am grateful to my parent, Eunsang Choi and Oksun Lee, for giving me great talent and their never-ending love. I also thank to my daughter, Anne S. Choi, for bearing her trouble without bothering me.

TABLE OF CONTENTS

LIST OF TABLES

CHAPTER 2

CHAPTER 4

CHAPTER 5

LIST OF FIGURES

CHAPTER 2

CHAPTER 3

CHAPTER 4

CHAPTER 5

CHAPTER 7

CHAPTER 1

1.1 INTRODUCTION

Sn-Pb solders have been extensively used as joining materials in electronic applications over the past several decades [1-5]. The widespread use of Sn-Pb solders is due to several advantages such as low cost, good manufacturability, good wettability on common substrate such as Cu and Ni used in electronics [1,3,4].

However, pending regulations regarding the toxic elements threaten to ban the use of Pb-containing solders in electronic applications due to the environmental and health concerns [1]. Another concern is that Sn-Pb solders are reaching the limit of performance capability since the adoption of surface mount technology. Increasing demands for greater packaging density and high performance are being realized with the advent of surface mount technology, resulting in increase of the numbers of solder joints per package and reduction of joint dimensions [6]. However, these changes demand the solder joint to be a mechanical connection as well as an electrical contact. Reliability losses in many electronic systems were identified with mechanical failure of the solder joint rather than device malfunctions [3]. These concerns have stimulated substantial efforts in the research and development of alternative Pb-free solder alloys with reinforcements.

Eutectic Sn-Ag solder has received much attention as a potential Pb-free candidate for electronic and automotive applications. The eutectic Sn-Ag solder is non-toxic, has a high melting temperature of 221°C, and generally exhibits better mechanical properties than the eutectic Sn-Pb solder. This solder also show comparable wetting characteristics

to eutectic Sn-Pb solder. Owing to its high melting temperature, it is considered as a Pb-free replacement in high temperature applications such as automotive under-the-hood and step soldering process. In contrast, its high melting point is an obstacle to its use in current manufacturing processes utilizing Sn-Pb solders.

Since the introduction of surface mounting technology that requires solders as a mechanical as well as electrical connection, demands for strong as well as compliant solder in soldering application have increased. Incorporation of reinforcements in Pb-free solders has been pursued to improve the mechanical and particularly thermomechanical behavior of solders, and their service temperature capability. Incorporation of reinforcements has been also attempted to match Pb-free candidates to current manufacturing processes based on Sn-Pb solder such as melting temperature, wettability.

Extensive database of Sn-Pb solder on mechanical and physical properties, and on deformation behavior and damage characterization has been established during past decades. However, those for Pb-free candidate solders are still far from complete, compared to Sn-Pb solder. The lack of a database for Pb-free candidates makes difficulties in developing composite solder with appropriate reinforcements.

Mechanical properties such as creep and fatigue have been studied on eutectic Sn-Ag solder. Attempts have been made to match melting temperature to that of Sn-Pb solder as well as to improve mechanical properties by incorporating more alloying elements. However, mechanical behavior of this solder is still not well understood. Microstructural characterization on deformation and damage has not been detailed yet.

Furthermore, limited work has been conducted on the effects of reinforcements on mechanical and aging properties of this solder.

1.2 RATIONALES AND GOAL

It is important to understand the deformation modes that the solder joint undergoes during service before the Pb-free candidates are taken into account to replace Pb-bearing solders. Thermomechanical fatigue (TMF) is the major deformation mode that the solder joint experiences during service. As the electronic device is turned on and off, or as the temperature of its environment changes, the solder joint is thermally cycled. During thermal cycling, the strains are developed in the solder joint due to the mismatches in the coefficients of thermal expansion (CTE) of the solder, substrate, and component. Thus, the solder joint experiences thermal fatigue that causes the thermal strains in cyclic nature [7-9]. Another important deformation mode is creep that is time dependent and operative at high temperature above $0.5T_m$. The solders have quite a low melting temperature, resulting in a higher homologous temperature than $0.5T_m$ even at room temperature. The temperature ranges that the solder joints are operated are at 50 to 80°C for typical electronic products such as computer and home appliances [10], and are raised up to 150°C for automotive application [2]. Since the solders are used at high homologous temperatures in service, the creep deformation is significant [7-9]. Consequently, the solder joints suffer creep-fatigue interaction, i.e. thermomechanical fatigue (TMF), which is cyclic, time dependent, and predominantly shear in nature [7]. The deformation during TMF is described in the form of the hysteresis loop of stress and strain. During high temperature regimes, the stress relaxation also takes place, introducing a further factor in

the deformation behavior [8,11]. In addition, the substrate affects the deformation of the solder joint by imposing the mechanical constraint and causing residual stress [12,13].

The deformation behavior of the solder joint becomes more complicate due to the complexity of microstructure of the solder joint in service. The solder is used in an as-solidified microstructure depending upon the processing history [7]. The microstructure of the solder is also altered due to the dissolution of substrate materials in the solder matrix during reflow [14,15]. Because of the high homologous temperatures during service condition, the as-solidified microstructure of the solder changes continuously [15,16]. As a result, the mechanical properties of the solder joint during service are different from those of the as-made solder joint. The microstructural evolution of the solder causes the deformation complicate and reliability analysis of the solder joint difficult.

A Pb-free solder candidate should have a steady microstructure exhibiting improved thermal fatigue resistance and creep strength. There are also other factors that should be considered such as melting temperature, solderability, thermal expansion coefficient, interfacial IMC layer growth, cost, etc for a Pb-free solder candidate to be acceptable in the industry-wide application. The shortcomings in the required properties can increase the possibility of solder joint failures during manufacturing and service, causing open circuits and/or mechanical failure of electronic modules [1].

The Pb-free candidates must be tested for various requirements discussed above to determine whether they are suitable for a Pb-free replacement. Since the solder joint undergo the creep-fatigue interaction, i.e. TMF, in actual service condition, it is important to identify the deformation behavior during creep and fatigue and responsible

mechanisms. And then appropriate models should be developed to assess the reliability of the solder joint based on lifetime estimation in the development of a superior Pb-free alternate. Since the solders are susceptible to changes in microstructure affecting mechanical properties during service, the microstructural evolutions should be taken into account in the analysis of solder joint reliability.

Although several Pb-free solder candidates have been considered over the last few years, there is no drop-in replacement for Pb-bearing solders yet. The database required to develop suitable Pb-free solder replacement is still far from complete. The goal of this research is to identify deformation behavior of the eutectic Sn-Ag and particulate reinforced Sn-Ag solder joints. Understanding of the deformation of the solder joint warrants how to improve the reliability of the solder joint. Another important factor affecting the reliability of the solder joint, interfacial IMC layer growth, was also conducted.

1.3 RESEARCH STRATEGY

This research aims to improve understanding of deformation behavior of the eutectic Sn-Ag and its *in-situ* composite solder joints. In order to understand deformation behavior of actual Sn-Ag solder joints in service conditions, thermomechanical fatigue (TMF) utilizing actual solder joints was carried out. Microstructural characterization of deformation behavior and damage accumulation occurring during thermal cycling was conducted. Using the eutectic Sn-Ag solder as a model system, the eutectic Sn-Ag solders reinforced with Cu_6Sn_5, Ni_3Sn_4, and $FeSn_2$, known as composite solders, were examined in the form of single shear lap solder joint made with two Cu substrates. Creep

deformation and interfacial IMC layer growth were investigated on eutectic Sn-Ag and its *in-situ* composite solder joints. The effects of intermetallic reinforcements on creep deformation and interfacial IMC layer growth were characterized. Properties of *in-situ* Sn-Ag composite solders were compared to the eutectic Sn-Ag solder.

In chapter two, the eutectic Sn-Ag solder is reviewed in terms of crystal structure, microstructure, creep, fatigue, interfacial intermetallic layers, and effects of reinforcement. In the review of creep, creep data for the eutectic Sn-Ag solder are summarized showing discrepancy in experimental results. Different viewpoints in the analysis of creep data are revealed. It is also shown that microstructural characterization of creep deformation did not support the measured creep data. Fatigue of the eutectic Sn-Ag solder is reviewed in terms of isothermal mechanical fatigue and thermomechanical fatigue. Important factors affecting fatigue behavior are summarized. Several features about thermomechanical fatigue of actual solder joints are emphasized to make a contrast to isothermal fatigue of bulk specimen and simplified solder joints.

In chapter three, detailed microstructural characterizations of thermomechanical fatigue deformation and damage occurring in actual Sn-Ag solder joints are presented. Several factors affecting thermomechanical fatigue are analyzed and discussed. Eutectic Sn-Ag and Sn-4Ag-0.5Cu solder joints are compared to identify the effect of the small amount of Cu on thermomechanical behavior.

Chapters four and five present effects of intermetallic reinforcements on interfacial intermetallic compound (IMC) layer growth during aging of solder joints. Growth of interfacial IMC layers is characterized during aging for time scale up to 5000 hours. Chapter four compares the IMC layer growth behaviors of eutectic Sn-Ag and eutectic

Sn-Pb solder joints, and their corresponding composite solder joints with Cu_6Sn_5 particulate reinforcements. Chapter five evaluates the effect of different types of reinforcement (Ni_3Sn_4 and $FeSn_2$) on IMC layer growth in the eutectic Sn-Ag solder joints.

Chapter six presents creep behavior of the eutectic Sn-Ag and three different Sn-Ag composite solder joints. Effects of different type of reinforcement on creep behavior are discussed. Difference between cyclic creep and monotonic creep are illustrated.

In chapter seven, possible mechanistic issues that could account for the observed creep behavior are discussed. Future works are suggested to verify hypotheses regarding mechanistic issues that determine creep properties of eutectic Sn-Ag and composite solder joints.

Finally, important observations on thermomechanical fatigue, interfacial IMC layer growth, and creep behavior of eutectic Sn-Ag and composite solder joints are summarized.

CHAPTER 2

OVERVIEW OF EUTECTIC Sn-Ag SOLDER and SOLDER JOINT

2.1 INTRODUCTION

Several Pb-free solders have been considered for the replacement of Sn-Pb solders. They include eutectic Sn-Ag, Sn-In, Sn-Zn, Sn-Bi, Sn-Sb, and Sn-Cu solders etc., and have Sn in common as a base metal [10,17]. Table 2.1 summarizes physical properties and cost of potential Pb-free solders [1,18-20]. The eutectic Sn-Ag solder is one of the leading Pb-free candidates. It generally exhibits better wetting characteristics than the eutectic Sn-Pb solder [4]. It has a higher melting temperature of 221°C in comparison to the eutectic Sn-Pb solder as highlighted in Table 2.1 and is suitable for high temperature applications such as automotive under-the-hood. In contrast, its high melting point is an obstacle to its use in other electronic assembly applications [10,21]. In this chapter, a literature review of eutectic Sn-Ag solder and solder joints will be given in terms of crystal structure, microstructure, creep, fatigue, interfacial IMC layer, and reinforcement strategies.

2.2 CRYSTAL STRUCTURE AND MICROSTRUCTURE

The eutectic Sn-Ag solder (96.5Sn-3.5Ag in wt%) alloy consists of two phases, β-Sn phase and Ag_3Sn intermetallic compound, with a melting temperature 221°C. As shown in Figure 2.1, β-Sn phase has a body-centered tetragonal structure with 4 Sn atoms in the unit cell at 000;0 ½ ¼ ; ½ ½ ½ ; ½ 0 ¾ and c/a ratio of 0.546 [22]. Ag_3Sn intermetallic compound is known as orthorhombic structure with lattice constants of a =

Table 2.1 Physical properties and cost of potential Pb-free eutectic solders [1,18-20].

Solders	M.P. (°C)	CTE (10^{-6}/°C)	Density (g/cm^3)	Cost ($/kg)
63Sn-37Pb	183	21	8.4	5.87
96.5Sn-3.5Ag	**221**	**22**	**7.36**	**13.73**
48Sn-52In	118	20	7.3	
42Sn-58Bi	138	15	8.7	7.79
91Sn-9Zn	199			7.99
99.3Sn-0.7Cu	227			8.62
95Sn-5Sb*	245	27		8.36

M.P. = Melting Point, CTE = Coefficient of thermal expansion.
*Near-peritectic composition.

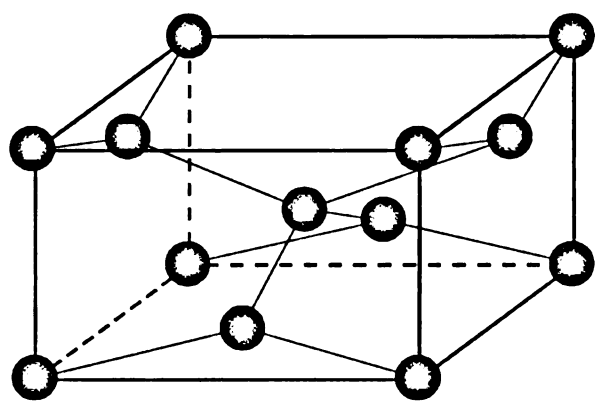

Figure 2.1 Unit cell of β-Sn phase (lattice parameter a=5.832 Å, c=3.182 Å) [22].

5.968 Å, b = 4.7802 Å, and c = 5.1843 Å, and 8 atoms in the unit cell, six atoms of Ag and two of Sn [23]. However, a complete configuration of atoms in the Ag_3Sn unit cell has not been reported yet.

The eutectic Sn-Ag solder has an equilibrium microstructure consisting of Ag_3Sn intermetallic aciculae dispersed in an almost pure β-Sn phase with less than 0.04 wt% Ag [24]. However, depending on the cooling rate during solidification process, it shows either essentially pure β-Sn with rod-like Ag_3Sn intermetallics or primary β-Sn dendrites with interdendritic eutectic microstructure, which is the mixture of Ag_3Sn particles and β-Sn phase [5,10,14,16,25]. The solder joint commonly contains the microstructure of the primary β-Sn dendrites with interdendritic eutectic mixture resulting from the faster cooling rate. Figure 2.2 illustrates a typical microstructure of the eutectic Sn-Ag solder matrix in a joint with Cu substrate [25].

The eutectic Sn-Ag microstructure was found to change due to aging at high temperature. During aging, the Ag_3Sn intermetallics coarsened, showing a decrease in number and increase in size [16,25]. The dendritic morphology of primary Sn phase also disappeared, resulting in the microstructure of Sn phase with coarsened Ag_3Sn intermetallics [25]. The coarsening was more significant at higher temperature, while it was very limited at room temperature. Figure 2.3 illustrates the microstructure of the eutectic Sn-Ag solder matrix in a joint with Cu substrate after aging for 100 hours at 150°C [25].

The microstructure and composition of the solder are altered when it is soldered to a substrate due to the dissolution of the substrate. During soldering of the eutectic Sn-Ag solder with a Cu substrate, Cu dissolves in the liquid solder and reacts with Sn, forming

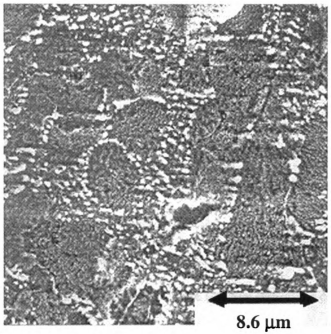

Figure 2.2 Typical microstructure of the eutectic Sn-Ag solder matrix in a joint with Cu substrate [25].

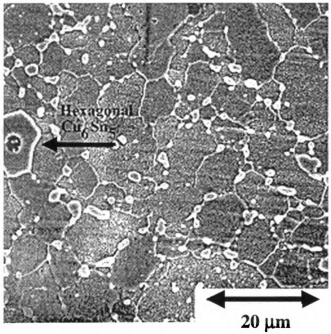

Figure 2.3 Microstructure of the eutectic Sn-Ag solder matrix in a joint with Cu substrate after aging for 100 hours at 150°C [25].

Cu_6Sn_5 intermetallic dendrites or particles in solder matrix during solidification [14-16,26]. The amount and size of the Cu_6Sn_5 dendrites in a solder joint were dependent on the maximum soldering temperature [15]. The overall amount of the Cu_6Sn_5 particles also depended on the cooling rate [14]. The Cu_6Sn_5 dendrites exhibited a coarsening behavior similar to Ag_3Sn particles [16].

The microstructure of the solder joint significantly affected the mechanical properties. The microstructure containing fine Ag_3Sn particles showed higher microhardness, higher maximum shear strength, and slightly reduced ductility compared to that with coarse Ag_3Sn rods [14-16]. The large Cu_6Sn_5 dendrites considerably reduced the ductility and slightly increased the maximum strength [15]. It is apparent that the microstructure produced by fast cooling rate and low soldering temperature would give better mechanical properties. However, the solder joint may not preserve the mechanical properties during service because of the changes in the microstructure such as coarsening.

2.3 CREEP

2.3.1 Overview of Creep Deformation

Creep is a time dependent deformation of a material when it is subjected to a constant load at constant temperature and is important at temperatures greater than $0.5T_m$. Creep strain is measured as a function of time and the slope of the creep strain-time curve is referred as a creep strain-rate. The creep curve is commonly described by reference to three different stages as shown in Figure 2.4, i.e. primary, secondary, and tertiary stages [27]. With a constant load applied to a specimen, the strain-rate decreases during the primary stage after an instantaneous strain on loading, indicating that the material

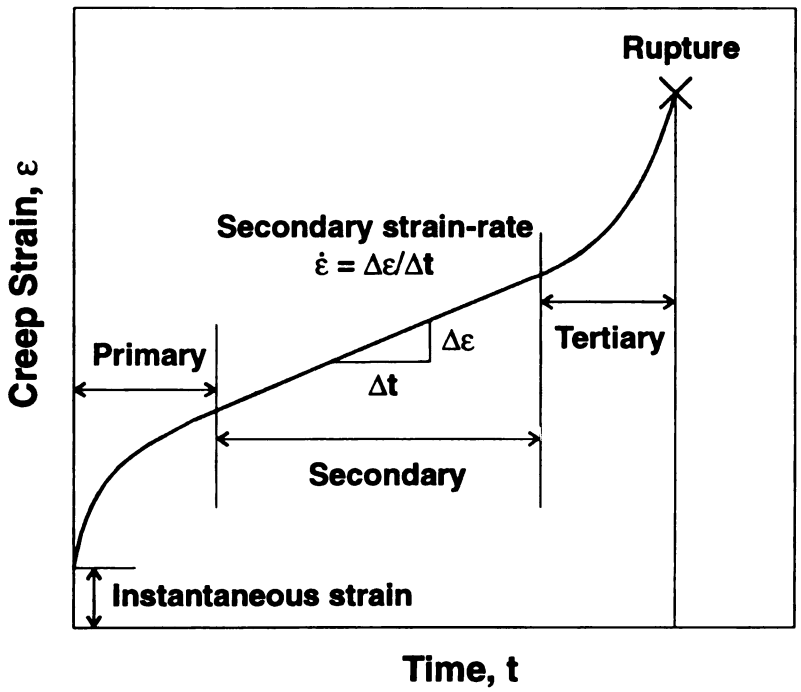

Figure 2.4 Schematic representation of a creep curve illustrating different creep deformation stages [27].

experiences an increase in creep resistance or strain hardening. After primary stage, strain-rate reaches a secondary stage where the strain-rate is constant. The constant strain-rate in the secondary stage is explained on the basis of a balance between the competing processes of strain hardening and recovery, and in some sample alloys a steady state microstructure develops. The secondary stage often has the longest duration in the lifetime of a material during creep deformation. During the tertiary stage, the strain-rate rapidly increases with time leading to fracture. An increase in strain-rate in the tertiary stage is related to microstructural changes such as grain boundary separation, the formation of cracks, cavities, voids, and neck formation, resulting in a decrease in the effective load-carrying area.

The creep resistance of a material is often described by the minimum strain-rate in secondary (or steady-state) stage. Both temperature and the level of applied stress influence the creep characteristics. With either increasing stress or temperature, the steady-state strain-rate is increased [29]. The stress dependence of strain-rate is expressed using an empirical relationship,

$$\dot{\gamma}_s = K_1 \tau^n ,$$

where K_1 is the constant and n is the material constant denoted as stress exponent. This equation provides the basis for the "power-law" relationship between strain-rate and stress, which have been used to describe high temperature creep behavior. The stress exponent, n, can be obtained from the slope of a straight line in the plot of $log\ \dot{\gamma}_s$ versus $log\ \tau$. The influence of temperature on strain-rate is described by an Arrhenius relationship,

$$\dot{\gamma}_s = K_2 \exp\left(\frac{-Q_c}{kT}\right),$$

where K_2 is the constant, k is Boltzmann's constant, and Q_c is the activation energy for creep. This equation shows that the strain-rate increases exponentially with increasing temperature. The activation energy, Q_c, can be evaluated from the slope of *log* $\dot{\gamma}_s$ versus *(1/T)* plot. Combining the above two equations gives a phenomenological power-law equation,

$$\dot{\gamma}_s = A' \tau^n \exp\left(\frac{-Q_c}{kT}\right),$$

where A' is a constant. Like the Mukherjee-Bird-Dorn power-law equation, this phenomenological power-law equation also shows the dependence of the steady-state strain-rate on both stress and temperature. The value of n and Q_c in both power-law equations varies depending on the applied stress and temperature.

Models for creep deformation based on steady-state are commonly expressed in the form of a generalized, dimensionless rate equation called the Mukherjee-Bird-Dorn power-law equation [28],

$$\frac{\dot{\gamma}_s kT}{DGb} = A\left(\frac{\tau}{G}\right)^n \left(\frac{b}{d}\right)^p \quad \text{or} \quad \frac{\dot{\gamma}_s kT}{D_o Gb} = A\left(\frac{\tau}{G}\right)^n \left(\frac{b}{d}\right)^p \exp\left(\frac{-Q_c}{kT}\right),$$

where $\dot{\gamma}_s$ is the steady-state shear strain-rate, k is Boltzmann's constant, T is absolute temperature, G is shear modulus, b is the magnitude of Burgers vector, A is a material-related constant, τ is the applied shear stress, n is the stress exponent, d is the grain size of a material, and p is a constant related to grain size. This equation determines both the minimum strain-rate exhibited by a sample at given stress and maximum stress that can be borne by a sample tested at given strain-rate [7]. D is the diffusion coefficient related to rate-controlling diffusional processes during creep deformation and expressed as following,

$$D = D_o \exp\left(\frac{-Q_c}{kT}\right),$$

where D_o is the pre-exponential constant and Q_c is the activation energy of the rate-limiting diffusion process for creep.

While the power law generally fits data at low and intermediate stresses, it breaks down at very high stress level. Figure 2.5 illustrates normalized steady-state behavior of eutectic Sn-Ag BGA (Ball Grid Array) solder joints where the power law breaks down at high stress levels [30]. The Dorn or phenomenological power law equation fits well up to stress levels of $10^{-3}\tau/G$, however, it breaks down at stress levels above $10^{-3}\tau/G$ due to non-linear increase of normalized shear strain-rate. This non-linear increase in strain-rate with increasing stress is often referred to as "power-law breakdown". The power-law breakdown regions can be described by a single expression using sinh function,

$$\dot{\gamma}_s = C_1\left(\frac{T}{G}\right)\left[\sinh\left(\alpha\frac{\tau}{G}\right)\right]^n \exp\left(\frac{-Q_c}{kT}\right),$$

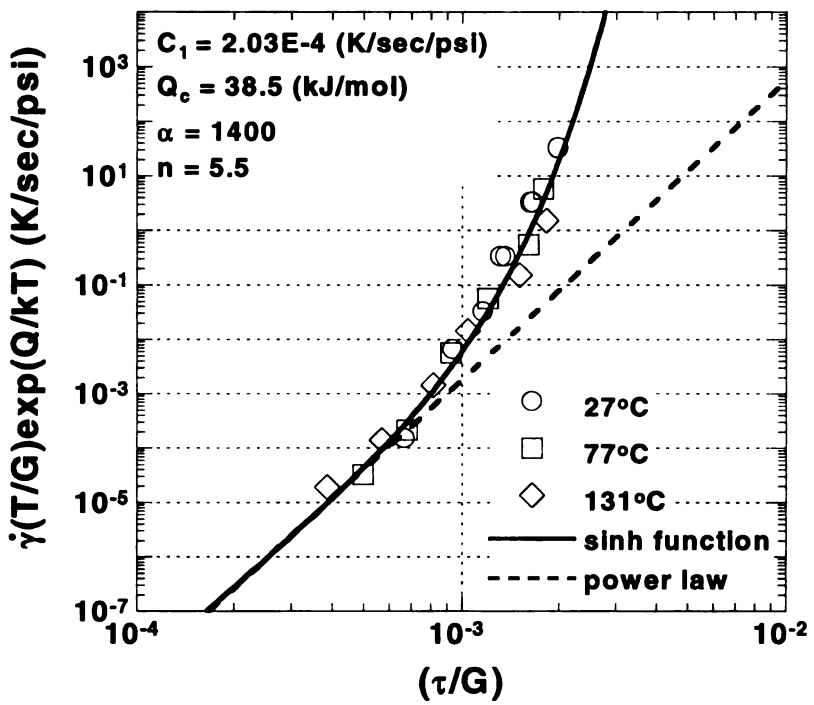

Figure 2.5 Normalized steady-state behavior of eutectic Sn-Ag BGA (Ball Grid Array) solder joints. Power-law breaks down at stress levels above $10^{-3}\tau/G$, while a sinh function fits all data well [30].

where α describes the stress level at which the power-law dependence breaks down, and C_l is a constant.

Several mechanisms can be responsible for creep. The rate-controlling mechanism depends both on stress level and temperature. The mechanisms responsible for creep can be conveniently described as a function of the applied stress and be divided into four major groups ; Diffusion creep, Dislocation creep, Dislocation glide, and Grain boundary sliding [31,32].

Diffusion creep involves the flow of vacancies and interstitials through a crystal under the influence of applied stress. It becomes the controlling mechanism at high temperatures and relatively low stresses, $\sigma/G < 10^{-4}$. Two mechanisms are considered important in this region ; Nabarro-Herring creep and Coble creep. Nabarro-Herring creep involves the stress-directed vacancy flow inside the grain. The vacancies move from regions experiencing tensile stresses to those which have compressive stresses under the applied stress. Simultaneously, there is a corresponding flow of atoms in the opposite direction, leading to elongation of the grain. Coble creep is based on diffusion along the grain boundaries instead of inside the grain. Coble creep predominates at relatively lower temperatures than those at which Nabarro-Herring creep is operative. Diffusion creep predicts a stress exponent close to unity, and activation energy (Q_c) close to that of lattice self-diffusion (Q_l) for Nabarro-Herring creep and grain boundary diffusion (Q_{gb}) for Coble creep. When diffusion creep processes dominate, the resistance to creep increases with increasing grain size.

Dislocation creep involves the movement of dislocations which overcome barriers by the diffusion of vacancies or interstitials. It occurs for stress ranges of $10^{-4} < \sigma/G <$

10^{-2}. The treatment given by Weertman [32] constitutes the fundamental theory for dislocation creep. It is based on a mechanism where dislocation climb is the rate-controlling step. At high temperature, if a gliding dislocation is held up by an obstacle, a small amount of climb may permit it to surmount the obstacle, allowing it to glide to the next set of obstacles where the process is repeated. In the sequential process of gliding and climbing, the gliding step produces almost all of the strain but the climbing step controls the velocity. Since dislocation climb requires diffusion of vacancies or interstitials, the rate-controlling step depends on the rate of atomic diffusion. This model predicts the stress exponent of 3, however, creep experiments with a range of metals show the stress exponent varying from 3 to 8, with a value of 5 most common. It also can be applied for both high temperature creep where activation energy for creep (Q_c) is that of lattice self-diffusion (Q_l), and for low temperature creep where activation energy for creep (Q_C) is that of pipe diffusion along dislocation cores (Q_{pd}).

Dislocation glide occurs at stress levels which are high relative to those normally considered in creep deformation, $\sigma/G > 10^{-2}$. At a certain stress level the power-law breaks down. It was observed in such a stress level that dislocation climb was replaced by dislocation glide, which does not depend on atomic diffusion. The creep-rate resulting from a dislocation glide mechanism is established by the ease with which dislocations are impeded by obstacles such as precipitates, solute atoms, and other dislocations. The thermally activated dislocation glide is considered to be the rate-controlling step in creep at such high stress levels.

Grain boundary sliding usually does not contribute significantly to secondary creep. However, it contributes in tertiary creep to the initiation and propagation of

intercrystalline cracks. Another deformation process where grain boundary sliding plays a significant role is superplasticity [33]. Most of superplastic deformation takes place by grain boundary sliding. Superplastic deformation requires a fine grain size, a relatively slow strain-rate (about 10^{-4} to 10^{-2} s^{-1} for many alloys), and a high homologous temperature. A characteristic of the superplastic deformation is that the strain-rate sensitivity m, which is the reciprocal of stress exponent n, is high (about 0.3 to 0.9). In addition to grain boundary sliding, some accommodation process is required to maintain material continuity during the sliding process such as diffusion and boundary migration. It has been known that grain boundary sliding must be also present during diffusion creep process to maintain material continuity.

More than one creep mechanism can operate at the same time [34,35]. If several mechanisms are operating independently of each other, then the overall creep rate is the sum of all the rates of the independent processes involved, i.e.

$$\dot{\gamma}_s = \sum_i \dot{\gamma}_i ,$$

where $\dot{\gamma}_i$ is the creep rate for the ith mechanism. For mechanisms operating parallel the fastest mechanism will dominate the creep behavior. When the deformation depends on a series of events occurring sequentially, with each event necessary for deformation to continue, the creep rate is

$$\dot{\gamma}_s = \frac{1}{\sum_i \left(1/\dot{\gamma}_i \right)} .$$

If there are i mechanisms operating in series, the slowest mechanism will control the creep deformation.

Although two independent processes can contribute to the overall creep rate, one of these processes is defined as dominant when the contribution made by other process is so small that it can be ignored. The dominant creep mechanism can be identified by comparing the experimentally measured values of n and Q_c with the values predicted theoretically for different creep mechanisms, since each creep mechanism predicts unique values of n and Q_c [36].

For instance, dislocation creep models generally lead to an n value of about 5, whereas diffusion creep theories give n values of unity. Thus, a transition from $n = 5$ to $n = 1$ with decreasing stress is usually taken as evidence for a change in the dominant mechanism from dislocation to diffusion creep processes. Then, in the $n = 5$ regime, when a change from $Q_c \cong Q_l$ to $Q_c < Q_l$ occurs, it is interpreted that lattice self-diffusion is becoming more difficult with decreasing temperature until the deformation behavior is controlled by preferential diffusion along dislocation core. Again, when diffusion creep dominates creep deformation exhibiting n values close to unity, a transition from $Q_c \cong Q_l$ to $Q_c < Q_l$ is related with a change in the dominant mechanism from Nabarro-Herring to Coble creep. In the diffusion creep regime, atomic flow occurs predominantly through the lattice at high temperatures giving $Q_c \cong Q_l$, but predominantly along grain boundaries as the temperature decreases below $0.6T_m$ giving $Q_c \cong Q_{gb}$. The n and Q_c values related to different creep mechanisms for pure metals are listed in Table 2.2 [37], together with the general stress and temperature conditions for each dominant creep process.

Table 2.2 Values of n and Q_c related with different creep mechanisms occurring with pure metals [37].

Creep mechanism	Stress	Temperature	n value	Q_c value
low temperature diffusion creep (Coble creep)	low	$0.4 \sim 0.7T_m$	~ 1	Q_{gb}
high temperature diffusion creep (Nabarro-Herring creep)	low	above $0.7T_m$	~ 1	Q_l
low temperature dislocation creep	intermediate/high	$0.4 \sim 0.7T_m$	> 3	Q_{pd}
high temperature dislocation creep	intermediate/high	above $0.7T_m$	> 3	Q_l

T_m = melting temperature, Q_l = the activation energy for lattice self-diffusion, Q_{gb} = the activation energy for grain boundary diffusion, Q_{pd} = the activation energy for diffusion along dislocation cores (often termed pipe-diffusion, $Q_{pd} \cong Q_{gb}$)

Sn-Pb solder is a good example showing the variations in n and Q_c values depending on stress and temperature. Figure 2.6 illustrates the different set of n and Q_c values in three distinct regions that have been identified in the eutectic Sn-Pb solder with a superplastic microstructure of 5.8 μm grain size [38]. The low stress regime called Region I exhibited a stress exponent of 3 and activation energy for creep close to that for lattice self-diffusion. The mechanism that controls the creep process in Region I is unknown. It was speculated that Region I is a distinct deformation mode intermediate between the superplastic region II and the diffusion creep processes [40]. In the middle range of strain-rates called Region II, a stress exponent in the range from 1.6 to 2.4 was reported in literature. Most of reported activation energies for Region II lie between 44 and 57 kJ/mol [41]. These values are comparable to the activation energies for grain boundary diffusion, which is approximately one-half that for lattice self-diffusion [39]. The mechanism controlling creep deformation in Region II is grain boundary sliding accommodated by grain boundary diffusion, and is responsible for superplastic deformation. At high strain-rates, the reported stress exponents are high, ranging from 4 to 7, and the activation energies are nearly equal to that for lattice self-diffusion [7]. Dislocation climb controlled by lattice self-diffusion is known as the deformation mechanism for Region II.

Solid solutions with a single phase have been investigated for stress ranges of $10^{-4} < \sigma/G < 10^{-2}$. Two very distinct responses were observed in solid solutions, referring to class M alloys (also called class II alloys) and class A alloys (also called class I alloys) [42]. Class M alloys show creep characteristics controlled by climb of dislocations, as in the case of pure metals, giving $n \cong 5$. Class A alloys show creep behavior where the

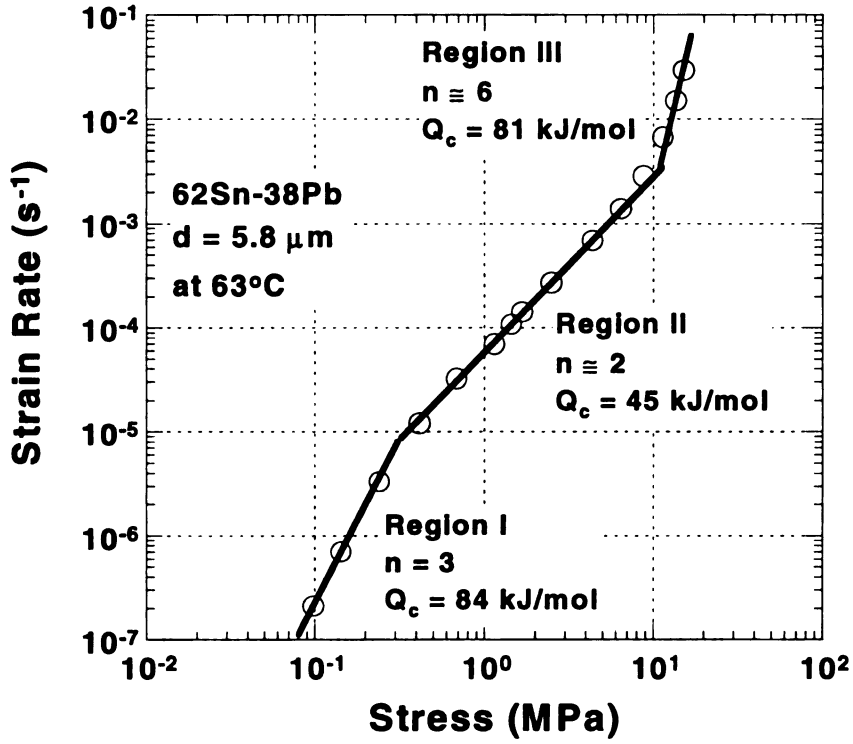

Figure 2.6 A plot of shear strain-rate vs. applied shear stress for the eutectic Sn-Pb solder alloy with a grain size of 5.8 μm at 63°C. Note that Q_l in Pb = 101 kJ/mol and Q_l in Sn = 94 kJ/mol [38,39].

dislocation movement is controlled by the drag of solutes, producing $n \cong 3$.

Comparing solid solutions with pure metals gives a good understanding of creep behavior of solid solutions [43]. In a pure metal showing a creep curve given in Figure 2.4, the initial strain-rate is very high because the existing and newly generated dislocations can freely move. As the creep deformation proceeds to the secondary stage, the dislocation density increases and the strain-rate decreases. The decrease in the strain-rate is due to an increased density of barriers, resulting in strain hardening. For class A alloys, each dislocation is pinned by a great number of solute atoms because the initial density of dislocations is low, leading to a low initial strain-rate. As the deformation proceeds, the dislocation density increases and the number of pinning solute atoms per unit length of dislocation decreases. Hence, the strain-rate increases due to an increase in mobile dislocation density with deformation. For class M alloys, dislocations are initially controlled by drag of solute atoms, resulting in a low initial strain-rate. However, dislocation creep becomes the rate-controlling mechanism after some deformation. Alloy additions may not alter the creep characteristics in class M alloys and there is no change in n value and creep mechanism, although a great number of solute atoms present in the parent lattice increases creep resistance by impeding dislocation glide and recovery processes.

Particle-hardened alloys (also called dispersion-strengthened alloys) are another form of material which can significantly increase the creep strength, compared with pure metals and solid solutions [44]. The improvements in creep resistance are achieved by introducing a fine dispersion of precipitates or insoluble particles which provide effective obstacles to dislocation movement. For particle-hardened alloys, dislocations can rarely

cut through the particles and consequently, dislocations attempt to surmount the obstacles by climb and cross slip. When dislocation creep is dominant, the creep properties are generally improved by increasing the volume fraction of particles. When diffusion creep is rate-controlling process, particles can also improve creep properties by pinning grain boundaries. Particles pinning grain boundaries can impede grain boundary sliding and affect the ease that vacancies can be generated at grain boundaries. Particle-hardened alloys are also characterized by a stress exponent higher than 7, considerably greater than the values expected for the appropriate matrix alloys. For applications requiring high creep resistance, it is essential that the particles do not coarsen rapidly during long exposure at the service temperatures. Particle coarsening increases both the average particle size and the mean interparticle spacing, so that it causes a decrease in the creep resistance due to fewer particles being present to impede dislocation movement.

2.3.2 Creep Deformation of Eutectic Sn-Ag Solder and Solder Joints

The creep properties of the eutectic Sn-3.5Ag solder have been investigated by several researchers in the form of a bulk solder specimen or a solder joint. Table 2.3 lists all reported experimental creep data for the eutectic Sn-Ag solder. From the review of the published data, it becomes apparent that there is no clear agreement in the experimental data, resulting in the discrepancy for the rate-controlling mechanism. The eutectic Sn-Ag solder was regarded as either pure Sn or a dispersion-strengthened alloy in the analysis of the creep properties.

Mathew *et al.* [45] reported that the eutectic Sn-Ag bulk with 20 μm average grain size exhibited the stress exponent of 5 and 60.7 kJ/mol activation energy in the constant

Table 2.3 Summary of published data for creep deformation of the eutectic Sn-Ag bulk solder and joint.

specimen	condition	n	Q_c	mechanism	T	σ	mode	[ref]
actual joint (ball grid array)	aged for several month or 100 hrs at 100°C	5.5	38.5	dislocation climb	27, 77, 131	3~42	shear	[30]
schematic single lap joint	water quenched	12 at RT 5 at 158°C			RT, 158	3~50	shear	[15]
bulk	aged for 3 hrs at 180°C	10	50	dislocation climb	25, 54, 150, 180	1~30	tension	[12]
bulk*	aged more than 3 months at RT	7.83	69.5	dislocation climb	23, 100, 150	3~20	tension	[46]
bulk	20 μm Sn grain	5	60.7	dislocation climb	23, 54, 100	1~30	tension	[45]
bulk	slow cooled, no aging	8.4 at RT 6.7 at other temp	62.6		20 ~ 160	2~50	tension	[47]
bulk	aged for 24 hrs at 150°C followed by 6 ~ 10 days at RT	11.3	82.3		25, 80	10~22	tension	[11]
bulk	1 μm Sn grain	6			20, 75, 125	10~30	compression	[48]

*95Sn-5Ag bulk solder was used instead of the eutectic Sn-Ag solder.
The units are Q_c (kJ/mol), T(°C), and σ (MPa).

load creep tests. In their tests, the method of increasing stress in steps when the steady state was reached on a single specimen was used until fracture. They compared with the creep data of pure Sn with 150 μm grain size obtained from the same tests, which are n = 7.6, Q_c = 60.3 kJ/mol, and the dislocation climb controlled by lattice self-diffusion as the deformation mechanism. And it was concluded that creep deformation of the eutectic Sn-Ag solder took place by the same mechanism as that for pure Sn. It should be noted that similar activation energy of about 60 kJ/mol was observed for the eutectic Sn-Ag solder and pure Sn despite the large difference in the grain size. The 60 kJ/mol activation energy was assumed to be that for lattice self-diffusion in pure Sn although it is more comparable to one half that for lattice self-diffusion in pure Sn, 94 kJ/mol [39]. In their analysis, the creep deformation controlled by grain boundary diffusion or dislocation pipe diffusion was excluded due to high homologous testing temperature up to $0.8T_m$.

Yang *et al.* [12] and Liang *et al.* [46] regarded the Sn-3.5Ag solder as a particle-hardened alloy. The Sn-Ag bulk specimens were aged to stabilize microstructures prior to testing in both studies as shown in Table 2.3. Yang *et al.* found n = 10 and Q_c = 50 kJ/mol in constant load creep tests of the eutectic Sn-Ag bulk. The activation energy value of 50 kJ/mol was approximately one half that for lattice self-diffusion in pure Sn, 94 kJ/mol. Along with a high stress exponent, dislocation climb over the Ag_3Sn particle, controlled by either grain boundary or dislocation pipe diffusion, was interpreted as the creep mechanism despite high homologous testing temperatures ranging from $0.6T_m$ to $0.92T_m$. Liang *et al.* observed n = 7.83 and Q_c = 69.5 kJ/mol in the creep tests of 95Sn-5Ag bulk. Dislocation climb was considered as the prevailing deformation mechanism with a stress exponent of 7.83.

The creep properties of the eutectic Sn-Ag solder greatly depended on the microstructure. Yang *et al.* [15] reported that the morphology of the Ag_3Sn particles resulting from different cooling rate greatly affected the creep behavior of the eutectic Sn-Ag single shear lap joints as shown in Figure 2.7. At room temperature, the water-quenched joints with fine Ag_3Sn particles exhibited almost three magnitudes lower strain-rate than the furnace-cooled ones with rod-like Ag_3Sn intermetallics. At 158°C, the water-quenched joints showed a lower strain-rate at high stresses and a higher strain-rate at low stresses than the furnace-cooled ones. On the other hand, the furnace-cooled joints had a higher total strain-to-failure compared to water-quenched joints at both temperatures.

It has been typically found that eutectic Sn-Ag solder is more creep resistant than pure Sn due to the additional Ag_3Sn particles [12, 47]. However, in the study of Mathew *et al.* [45], the eutectic Sn-Ag solder was less creep resistant as shown in Figure 2.8 than pure Sn. They used pure Sn with a 150μm grain size, and the eutectic Sn-Ag with fine rod-shaped Ag_3Sn and a grain size of 20 μm. The observations in Mathew *et al.*'s study indicate that rod-shaped Ag_3Sn particles do not play any role in the creep deformation, and deformation along grain boundary might be significant, resulting in higher strain-rate.

Solder joints are more creep resistant than the bulk solder. Figure 2.9 shows a comparison of the stress vs. strain-rate data of the eutectic Sn-Ag bulk, and actual or schematic shear lap solder joints along with additional pure Sn data [12,15,30,46-50]. Since the solder joints were tested in shear and bulk in tension or compression, the appropriate comparison was made using following two equations,

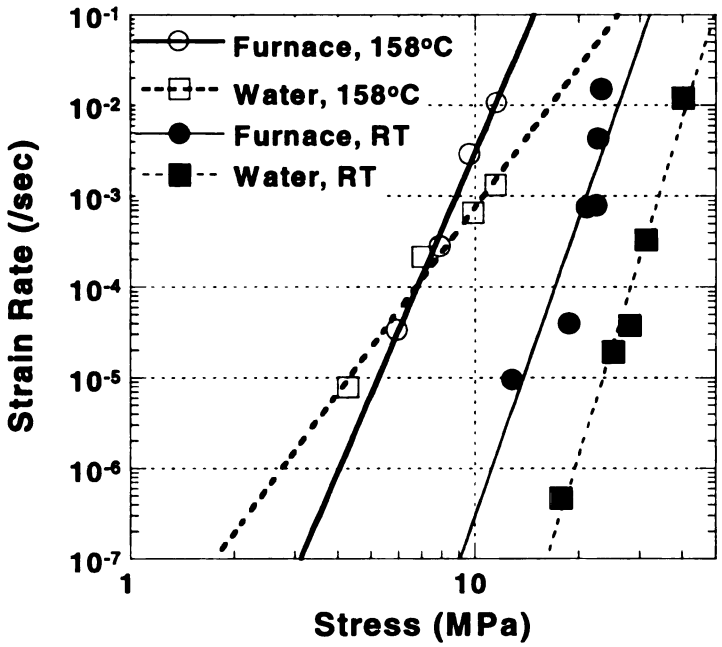

Figure 2.7 A plot of applied stress vs. strain-rate for the eutectic Sn-Ag single shear lap joints illustrating the influence of different Ag_3Sn morphology on the creep behavior [15].

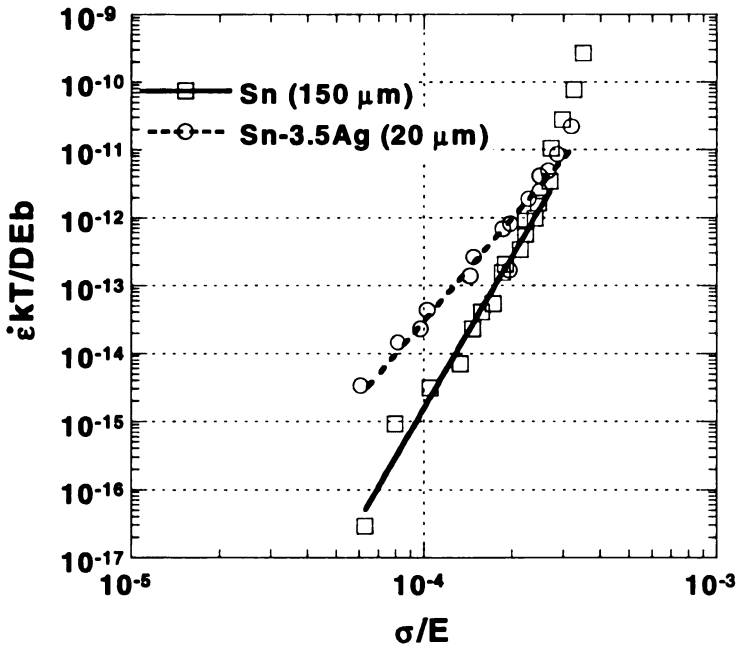

Figure 2.8 A plot of normalized stress vs. strain-rate for pure Sn and the eutectic Sn-Ag solder illustrating the effects of different microstructure on creep behavior [45].

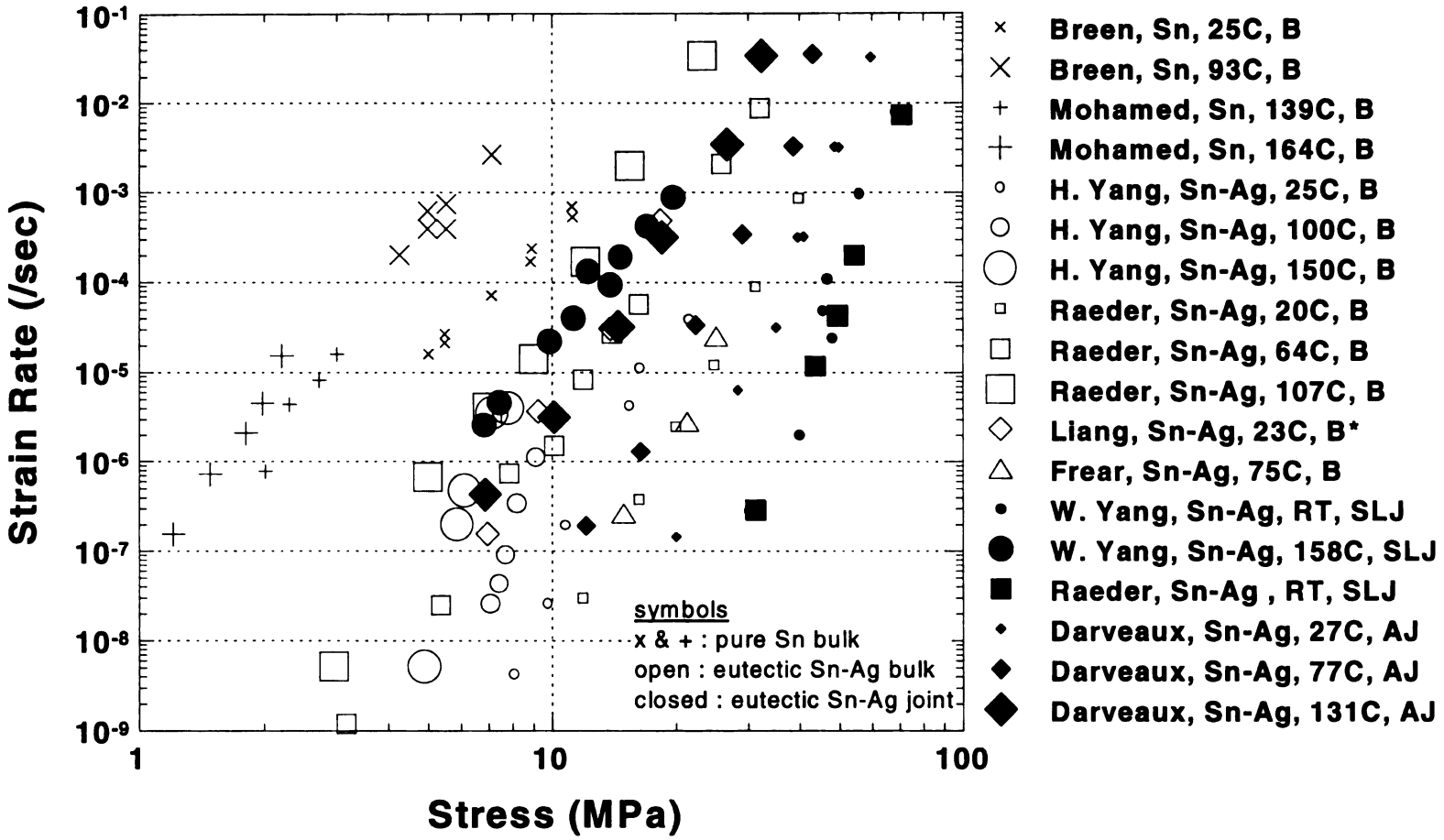

Figure 2.9 A comparison of the creep behavior of eutectic Sn-Ag solders along with pure Sn data [12,15,30,46-50]. In legends, B denotes bulk, SLJ denotes schematic single shear lap joint, and AJ denotes actual joint. *95Sn-5Ag bulk solder was used instead of the eutectic Sn-Ag solder.

$$\sigma = \tau\sqrt{3} \text{ and } \dot{\varepsilon} = \dot{\gamma}/\sqrt{3}$$

neglecting microstructural differences. The Following reasons were attributed for difference in creep behavior between bulk and the solder joint [12,30,47] ; (i) change in solder composition due to the dissolution of substrate in the solder matrix during soldering, (ii) formation of intermetallics in the solder matrix due to reaction of solder and dissolved substrate element, resulting in dispersion-strengthening effect, (iii) the mechanical constraint imposed by substrate and/or interfacial intermetallic layer between solder/substrate, (iv) different microstructure of the solder joint depending on the soldering parameters compared to that of bulk solder.

The creep data of actual solder joints are very limited at present. The creep properties of actual solder joints are greatly affected by the specification of solder joint such as geometry, materials to be attached, and metallization on attached materials. Darveaux *et al.* [30] utilized the actual eutectic Sn-Ag solder joints used in flip chip applications joining two ceramic substrates with a metallization consisting of Cu-Ni-Au. They tested double lap shear specimens comprised of 9 joints in each interface. Prior to testing, the solder joints were aged for several months at room temperature or 100 hours at 100°C.

Results of Darveaux *et al.* study are shown in Figure 2.5 in a plot of normalized strain-rate vs. normalized stress. In their study, the stress exponent of 5.5 was found, indicative of dislocation climb controlled deformation. However, the activation energy of 38.5 kJ/mol was considerably lower than the expected values of lattice self-diffusion

(106 kJ/mol), or grain boundary or pipe diffusion (63 kJ/mol) in pure Sn. They interpreted that the activation energy might be stress dependent since the data in the stress range more than $10^{-3}\tau/G$ lies in the power law break down regime, causing lower activation energy.

One important microstructural feature in the solder joints used by Darveaux *et al.* is rod-like gold-tin intermetallic compounds formed by the reaction of Sn with Au from gold metallization during soldering. Gold was found to significantly affect the mechanical properties of the eutectic Sn-Ag solder in the study of Harada *et al.* [51]. As given in Figure 2.10, when more than 6 mass% Au was added to the Sn-3.5Ag solder, the fracture elongation was reduced to less than 5%, while the tensile strength of Sn-3.5Ag solder increased gradually with the addition of gold. The gold-tin intermetallic compounds at grain boundaries may provide sites for the stress concentration and crack nucleation through grain boundary sliding process even with deformation as small as 0.2% [52]. In the study of Darveaux *et al.*, if the gold-tin compounds were susceptible sites for crack nucleation, an accumulation of damage may begin in early stage of creep deformation and this may be the reason for low activation energy.

Igoshev *et al.* [52] have shown the discrepancy between the experimental results and expected ones using the transition homologous temperature (η_t) from lattice diffusion controlled creep to dislocation pipe diffusion controlled creep. It is commonly observed that as the homologous temperature (T/T_m) is decreased, there is a transition from lattice self-diffusion controlled creep to dislocation pipe diffusion controlled creep. The transition homologous temperature (η_t) is proportional to the applied stress and is usually about 0.5 ~ 0.6 for most metals. According to the discussion given by Igoshev *et al.*, the

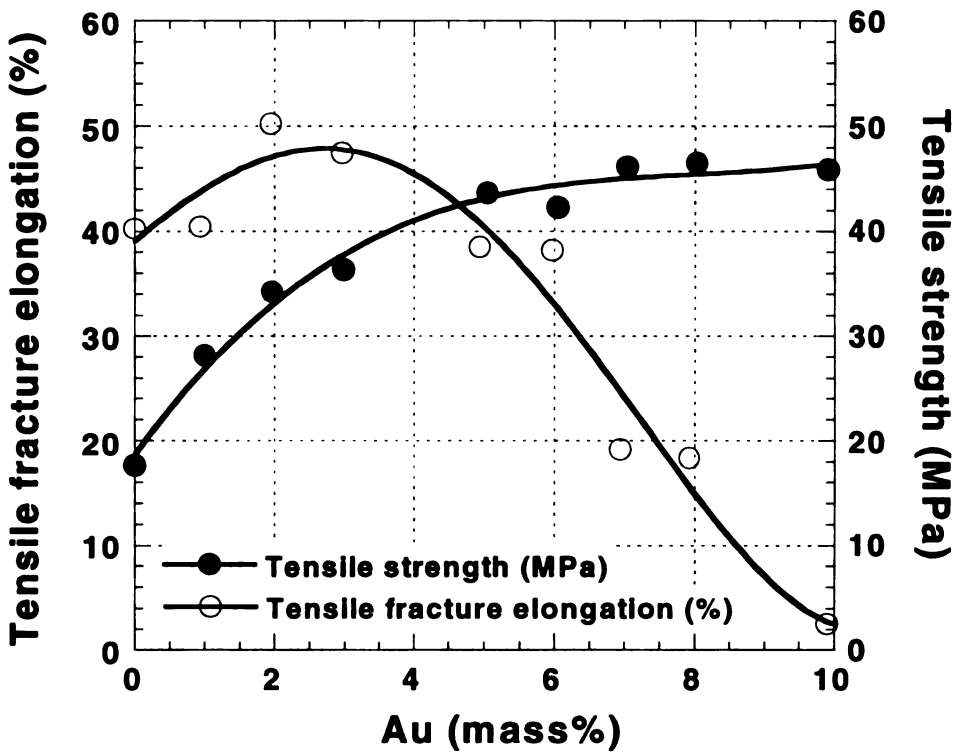

Figure 2.10 Effect of gold content on tensile fracture elongation and tensile strength [51].

dislocation pipe diffusion with Q_{pd} = 44 kJ/mol. Igoshev *et al.* predicted that the activation energy for creep of Sn-3.5Ag solder should be slightly or considerably higher than for pure Sn due to Ag_3Sn intermetallics, depending on the microstructure. As listed in Table 2.3, the activation energy measured by Darveaux *et al.* is slightly lower than the expected one for pure Sn, while others have observed a much higher activation energy.

Igoshev *et al.* [52,53] suggested that in the analysis of the creep of Sn-3.5Ag solder, some other mechanisms such as grain boundary sliding should be considered as well as dislocation movement to account for the discrepancy in the creep data. The microstructural studies of creep deformation appear to support this suggestion. Frear [48] reported that the creep strain was accommodated through the Sn matrix with a grain size of approximately 1 μm, at Sn-Sn grain boundaries, in compressive creep testing on the eutectic Sn-Ag right-circular bulk sample. Igoshev *et al.* [53] noticed that microcracks accumulated at grain boundaries due to grain boundary sliding, leading to intercrystalline fracture during creep deformation of the eutectic Sn-Ag bulk specimen. The accumulation of defects along grain boundary started at an earlier stage of creep and lasted for at least 70 ~ 80% of the lifetime. In the study of Mathew *et al.* [45], the eutectic Sn-Ag solder with 20 μm grain size exhibited a higher strain-rate than pure Sn with 150 μm grain size. Even with additional Ag_3Sn intermetallic phase, the fact that the eutectic Sn-Ag solder was less creep resistant indicates that the deformation along grain boundary significantly reduces the creep strength. However, such processes as grain boundary sliding largely depend on microstructural features such as grain size. The Sn grain size of Sn-3.5 Ag bulk used in the study of Frear [48] was about 1 μm, comparable to the size of Ag_3Sn particle formed by rapid cooling during soldering [15,16,25].

Although a great deal of efforts has been performed to understand creep deformation of Sn-Ag solder, large discrepancies between experimental results still remain. While the analysis of creep deformation mostly relies on the measured creep data, there is no substantial study on the characterization of microstructures occurring during creep deformation. Observed microstructural feature such as grain boundary sliding does not support the measured creep data. In order to clearly understand creep deformation of the eutectic Sn-Ag solder, systematic studies should be conducted by using a consistent microstructure and specimen geometry. Study on microstructural characterization must be conducted to verify measured creep data.

2.4 FATIGUE

2.4.1 Overview of Fatigue

Fatigue is defined as the phenomenon of failure of a material under cyclic loading [54]. It is known that failure under cyclic stress or strain occurs at a stress level much lower than that under conditions on monotonic loading. A fatigue failure is also insidious because it occurs without any obvious warning, resulting in a brittle-appearing fracture with no gross deformation at the fracture. Three basic factors are necessary to cause fatigue failure, which are a maximum tensile stress of sufficiently high value, a large enough variation or fluctuation in the applied stress, and a sufficiently large number of cycles of the applied stress. There are some important parameters, as shown in Figure 2.11, which is useful in analysis of the fatigue phenomenon [55]. These parameters are

Cyclic stress range : $\Delta\sigma = \sigma_{max} - \sigma_{min}$,

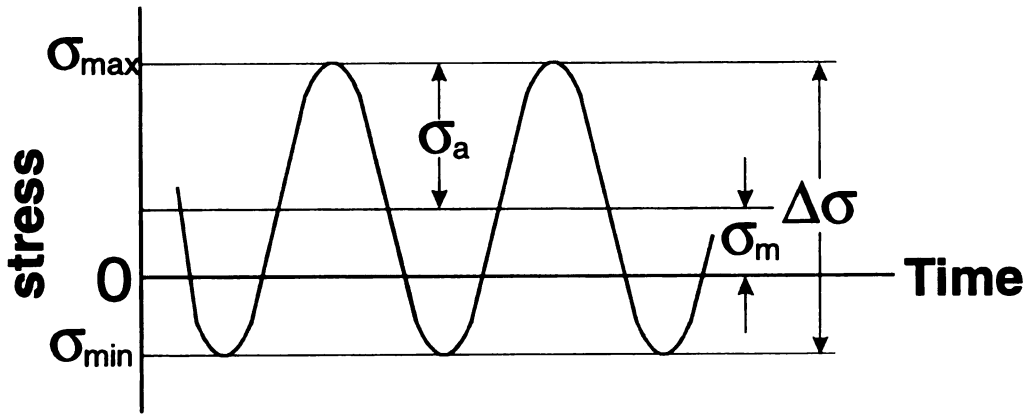

Figure 2.11 Fatigue parameters [55].

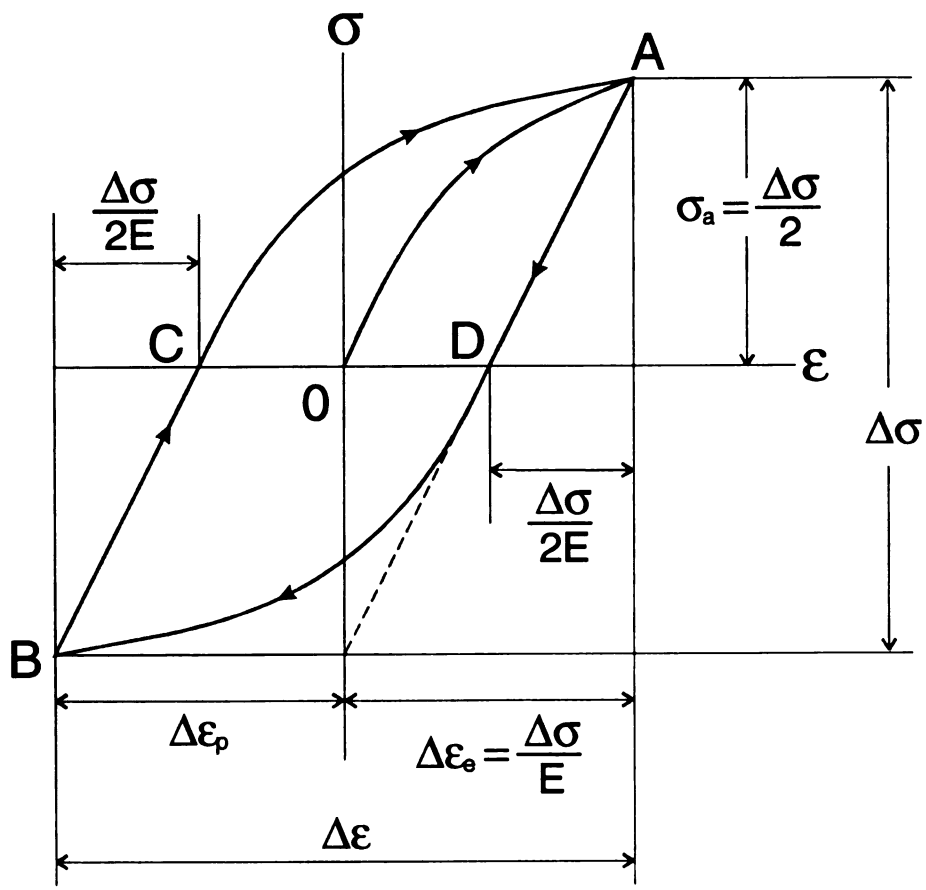

Figure 2.12 Notation for a symmetric hysteresis loop [56].

Cyclic stress amplitude or alternating stress : $\sigma_a = \frac{\sigma_{max} - \sigma_{min}}{2} = \frac{\Delta\sigma}{2}$,

Mean stress : $\sigma_m = \frac{\sigma_{max} + \sigma_{min}}{2}$.

In the cyclic loading in elastic regimes, stress and strain are related through the elastic modulus. In such case, for any controlling factor, σ or ε, the signal goes from 0 to (σ, ε) to ($-\sigma$, $-\varepsilon$) and back to zero. For any cyclic loading that produces plastic strains, however, the responses from a material are more complex. Figure 2.12 illustrates the results schematically [56]. During initial loading in tension, the stress-strain curve is O to A. On unloading and yielding in compression, we get to point B. On reloading in tension from B and returning to point A, a hysteresis loop develops. The dimensions of the hysteresis loop are described by the total stress range ($\Delta\sigma$) and the total strain range ($\Delta\varepsilon$). The total strain range ($\Delta\varepsilon$) consists of elastic and plastic strains. The elastic component is $\Delta\varepsilon_e = \Delta\sigma/E$, where E is the elastic modulus, and the plastic component is expressed as $\Delta\varepsilon_p = \Delta\varepsilon - \Delta\varepsilon_e$. The area of the hysteresis loop is equal to the work done or energy loss per cycle.

There are two types of cyclic loading as shown in Figure 2.13 and 2.14 schematically, stress-controlled cycling and strain-controlled cycling [57]. In the case of stress-controlled cycling, the controlling factor is the stress that oscillates between two extremes, that is, the cyclic stress amplitude σ_a is constant. However, the strain amplitude is not constant. In the strain-controlled cycling, the strain range is constant and the stress changes.

Since the plastic deformation produced during cyclic loading is not completely

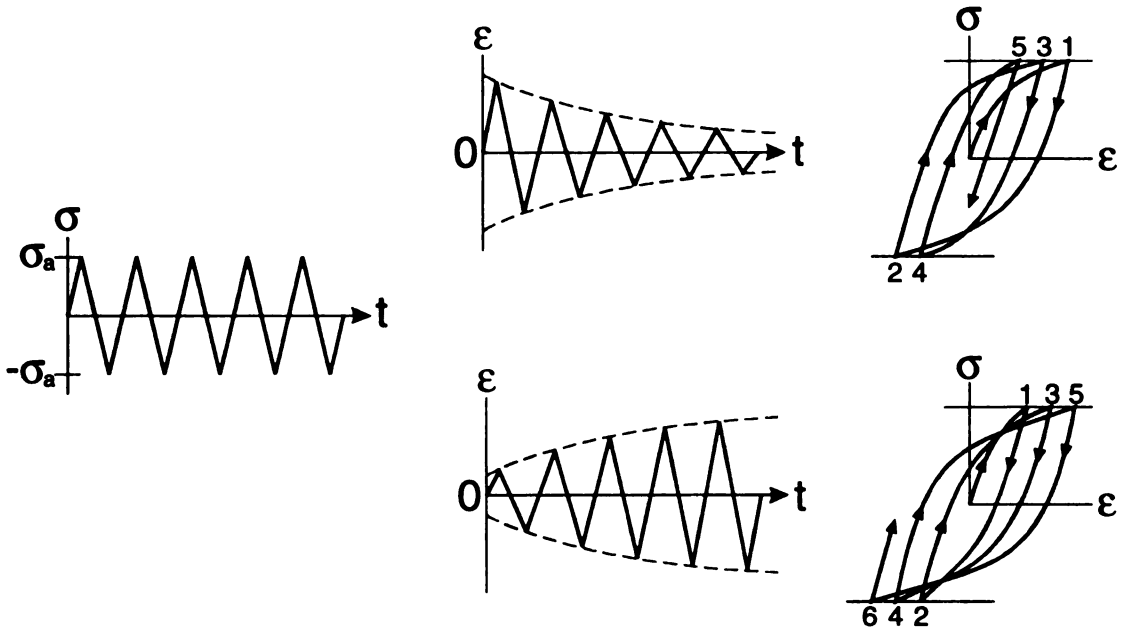

Figure 2.13 Cyclic behavior of a material under stress control [57].

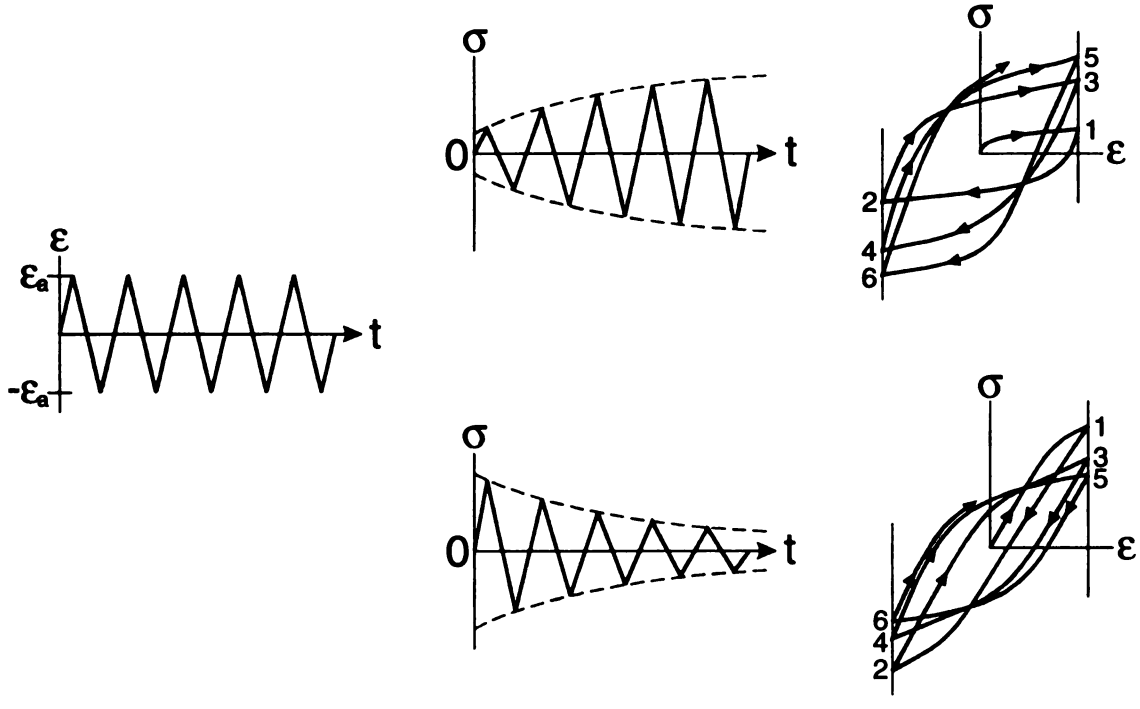

Figure 2.14 Cyclic behavior of a material under strain control [57].

reversible, the structural modifications occur during cyclic loading and these can result in changes in the stress-strain responses. Depending on the initial state a metal may undergo cyclic hardening, cyclic softening, or remain cyclically stable. In the stress-controlled cycling, the cyclic hardening occurs when a material increases in resistance to further deformation with cycling. The cyclic strain then becomes smaller under the same stress amplitude. On the other hand, cyclic softening occurs when a material shows an increasing deformation with cycling under stress control. Figure 2.13 depicts the phenomenon of cyclic hardening and cyclic softening under stress control. Figure 2.14 shows the cases of cyclic hardening and cyclic softening under strain control. The cyclic hardening under strain control implies that resistance of materials to deformation increases with cycling causing increase in stress to deform the material to the imposed strain limits. The cyclic softening under strain control indicates that the material deforms easily, resulting in a decrease in stress to deform to the imposed strain limits.

The behavior of a material under conditions of fatigue has been studied by means of the S-N curve, a plot of stress S versus the number of cycles to failure N [58]. The stress value in the S-N plot can be σ_a, σ_{max}, or σ_{min}, and the S-N relationship is determined for a specified value of σ_m. The S-N curve is mainly involved with fatigue failure at high number of cycles ($N > 10^5$ cycles) where the nominal stress and strain are elastic. Figure 2.15 gives typical S-N curves for ferrous and non-ferrous metals [59]. The number of cycle to failure increases with decreasing stress. There is a fatigue limit or endurance limit given by a horizontal line which represents a stress level. Below this stress, the material can be cycled without failure. The ferrous metals show a fatigue limit, while non-ferrous metal does not have a true fatigue limit. The S-N curve in the high cycle

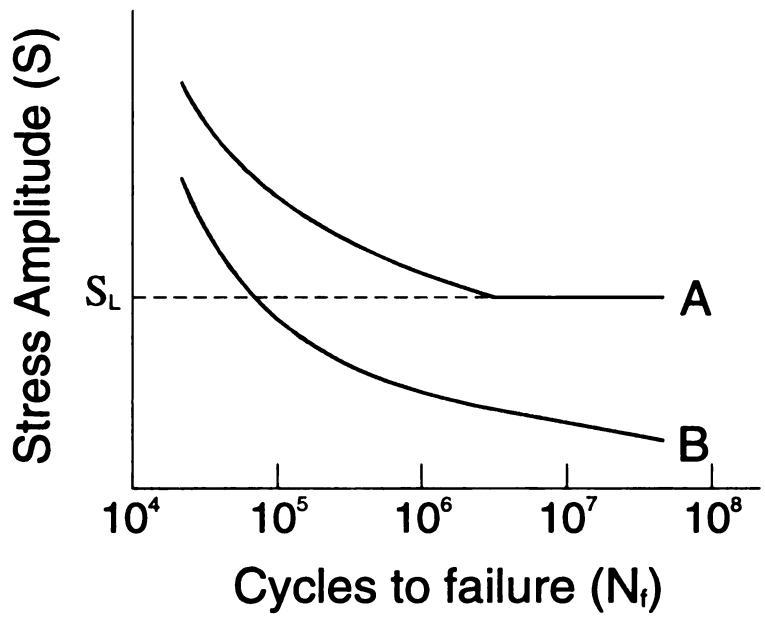

Figure 2.15 Stress (S) – cycles to failure (N) curves. A is for ferrous metals and B is for nonferrous metals. S_L is the fatigue or endurance limit [59].

region is described by the Basquin equation [60],

$$N\sigma_a^p = C \ ,$$

where σ_a is the stress amplitude, and p and C are empirical constants.

When fatigue life or fatigue strength is considered, it is convenient to consider the elastic and the plastic components of strain separately. It is also common to distinguish by high cycle fatigue ($N > 10^5$ cycles) and low cycle fatigue ($N < 10^4$ or 10^5 cycles). For high cycle regime, the stress and strain on a gross scale are elastic. However, the material deforms plastically in a highly localized region along persisted slip bands. The conditions of low cycle fatigue are frequently caused by a thermal origin. Since the thermal stress arise from the thermal expansion of the material, in this case the fatigue results from cyclic strain rather than from cyclic stress.

The elastic component is readily described using the true stress amplitude and the number of reversal (i.e. twice the number of cycles) [61],

$$\frac{\Delta\varepsilon_e}{2} = \frac{\sigma_a}{E} = \left(\frac{\sigma_f'}{E}\right)(2N_f)^b$$

where $\Delta\varepsilon_e$ is the elastic strain amplitude, σ_a the true stress amplitude, σ_f' the fatigue strength coefficient (equal to stress intercept at $2N_f = 1$), N_f the number of cycles to failure, and b the fatigue strength exponent. This relation is an empirical representation of the S-N curve above the fatigue limit. A smaller value of b results in longer fatigue lives. The plastic strain component is described by Coffin-Manson relation [62],

$$\frac{\Delta\varepsilon_p}{2} = \varepsilon_f'(2N_f)^c$$

where $\Delta\varepsilon_p$ is the plastic strain amplitude, ε_f' is the ductility coefficient (equal to strain intercept at $2N_f=1$), $2N_f$ is the number of reversals to failure, and c the ductility exponent. A smaller value of c results in a longer fatigue life. A valid equation for the entire range (elastic plus plastic strain) of fatigue life is obtained by superposition of the elastic and plastic strain component, which is,

$$\frac{\Delta\varepsilon_t}{2} = \frac{\Delta\varepsilon_e}{2} + \frac{\Delta\varepsilon_p}{2} = \left(\frac{\sigma_f'}{E}\right)(2N_f)^b + \varepsilon_f'(2N_f)^c .$$

Figure 2.16 schematically illustrates that the superposition of elastic and plastic curves gives the fatigue life in terms of total strain [63]. The fatigue life curve in terms of total strain tends toward the plastic curve at large total strain amplitudes, whereas it will tend to the elastic curve at low total strain amplitudes. Figure 2.17 shows the application of this equation to 95Pb-5Sn solder when tested in torsion from 0.05% to 2.0% at 25°C [64].

2.4.2 Fatigue Deformation of Solder Joints

The fatigue failure of solder joints in an electronic device results from the imposition of strain due to different coefficients of thermal expansion of the joining materials. The fatigue process in a device is controlled by the total strain, i.e. a solder

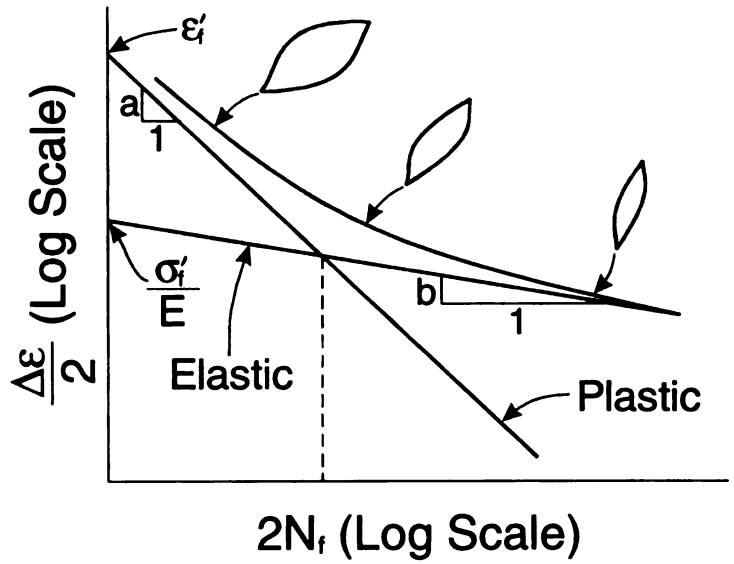

Figure 2.16 Fatigue life in terms of total strain obtained by superposition of elastic and plastic curves [63].

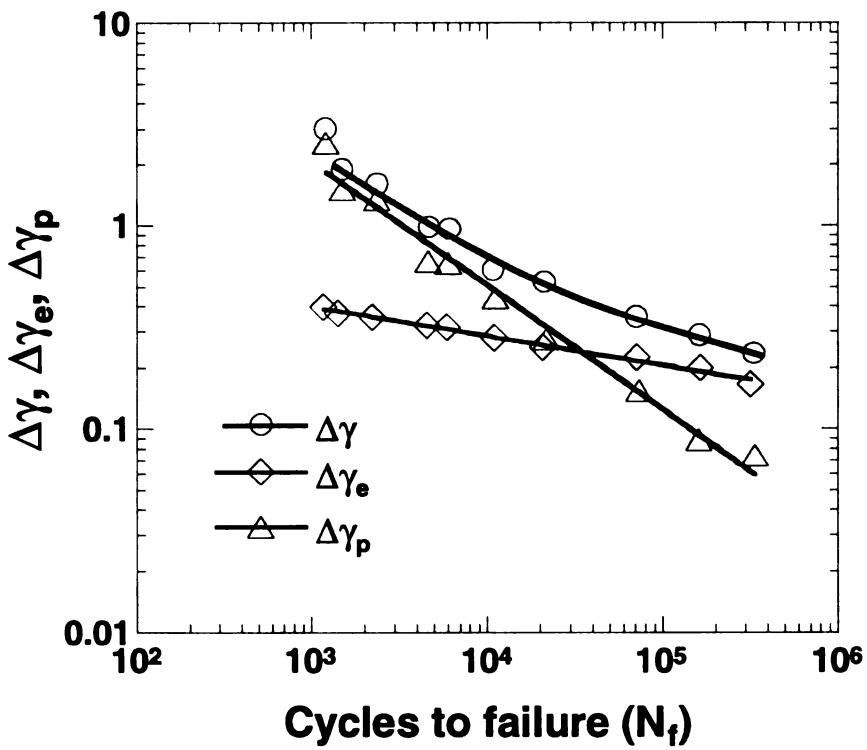

Figure 2.17 Number of cycles versus strain for 95Sn-5Pb solder. Torsion tests without hold time 25°C. [64].

joint experiences constant strain-controlled fatigue with dwell times at the strain extremes [65]. The strain levels are determined by thermal expansion mismatch of joining materials, thermal gradients in a package, temperature excursions during service, the geometry of the solder joint, and compliance of the joint system [66].

The fatigue properties of solder materials used in electronic packaging are measured by two different modes, isothermal fatigue and thermomechanical fatigue [67]. Isothermal fatigue is performed by mechanically cycling under a constant total or plastic strain control at a constant temperature since a solder joint in a package undergo strain-controlled fatigue. Thermomechanical fatigue is conducted by thermally cycling between two temperature extremes, which is closer to the actual service conditions of electronic packages and assemblies. However, the isothermal fatigue is easier to control, conduct, and interpret, and less costly than thermomechanical fatigue tests.

2.4.2.1 Fatigue Failure Criteria of Solder Joints

The criteria of fatigue failure of a solder joint vary, causing difficulty in making a comparison between data from studies that employed different variables. They can be categorized as follows : catastrophic failure, surface cracks, load drop, and electrical failure [67]. The catastrophic failure is the case when the specimen is separated into two parts. The surface cracks are related to earlier processes in the failure sequence. In the evolution toward a catastrophic failure, microcracks initiate at flaws, propagate, coalesce to form a well-behaved crack that advances a certain amount per cycle and grows to failure. This definition of failure was found to correspond to 1 mm of surface crack trace per 1 mm2 of surface area in 96.5Pb-3.5Sn solder. Load drop is defined as the number of

cycles to reduce the total load range to 75%, 50%, or 25% of that of the first cycle in hysteresis loop. When a different value of load drop is used as a criterion of fatigue failure, it leads to a different number of cycles to failure. In industry, devices are thermally cycled and solder joint integrity is monitored by mean of electrical resistance measurements [68]. The electric failure criterion does not correlate well with load drop because the load can drop 100% while the fracture surfaces are still in intimate electrical contact, showing little or no change in resistance. Studies on the relationship between load drop and resistance changes have shown that fatigue failure by load drop preceded failure by an electrical criterion [68]. It is desirable to use isothermal fatigue for estimates of thermomechanical fatigue life due to its convenience. However, studies attempting to correlate isothermal fatigue data to thermomechanical fatigue data should use the same failure criteria so that the comparison can be meaningful.

2.4.2.2 Isothermal Mechanical Fatigue of Solder Joints

To understand fundamental fatigue properties of solders, and to form a basis for understanding thermomechanical fatigue properties, isothermal fatigue studies have been performed in the strain and temperature ranges of interest. The most important factors affecting fatigue properties include strain range, ramp time, hold time, temperature, and aging [69].

Increasing strain range during cycling of materials leads to a decrease in the number of cycles to failure. It is also obvious in the Coffin-Manson relation to have an inverse relationship between strain range and number of cycles to failure. Effect of ramp time to extremes of strain or stress in isothermal fatigue is considered by means of frequency in

the cycle. Frequency is usually taken as the number of cycles per unit time. However, this definition of frequency needs a correction because the duration of a cycle consists of both the ramp time and the hold time. Thus frequency is defined as the reciprocal of twice the ramp time, separating frequency from the number of cycles per unit time [65]. This definition also makes frequency as a strain-rate variable. The reduction in frequency is found to decrease the number of cycles to failure in isothermal fatigue. The effect of frequency becomes more significant at high temperatures (> 0.5 M.P.) because at high temperatures, time dependent processes such as creep play important roles in deformation and/or damage accumulation.

Hold times introduced in the cycle at maximum, minimum, or both strains, stresses, or temperatures affect the fatigue life of materials. The number of cycles to failure decreases with increasing hold time [65]. The reduction in fatigue life due to hold time is attributed mainly to time-dependent creep deformation occurring during hold time. When the effects of ramp time and hold time on fatigue life are compared, the effect of hold time is much more dramatic than that of ramp time. The difference in the effects of ramp time and hold time on fatigue life is attributed to differences in strain-rates operating during ramp time and hold time. Strain-rates during very short hold times are much slower than strain-rates during even very long ramp times. Since the fatigue failure for solders are very sensitive to strain-rates, the effects of hold time and ramp time on fatigue of solders thus are found to be dramatically different.

As temperature increases, the isothermal fatigue life is considered to decrease. However, the degree to which fatigue life is affected depends on the material and testing conditions. For near eutectic Sn-Pb solders, the effect of temperature is insignificant for

all strain ranges employed. The temperature effect on fatigue of low Sn Sn-Pb solders such as 95Pb-5Sn and 96.5Sn-3.5Sn is observed to be more pronounced than for near eutectic Sn-Pb solders. The effect of temperature on fatigue life is also a function of frequency and hold time. It is observed to be more significant for fatigue under low strain-rate conditions, which correspond to long ramp time (or low frequency) and hold time in the cycle.

The effect of aging on solder behavior is a function of composition and the initial microstructure of the solder. Solders are generally two-phase materials with a low melting point, where the solubility in each phase decreases with a decrease in temperature. Precipitation of the second phase out of solid solution and phase coarsening occur even at room temperature after the solder joint is solidified. When there is a precipitation of the second phase during aging, the mechanical and fatigue strength increase, while phase coarsening due to aging decreases mechanical properties of solders. The fine microstructure of rapidly cooled solders leads to higher initial strength. However, aging leads to a coarsened microstructure, causing reduction in strength. Thus, aging is considered to neutralize the effects of initial microstructure on mechanical properties of solders.

2.4.2.3 Thermomechanical Fatigue of Solder Joints

Thermomechanical fatigue of a solder joint arises when temperature fluctuations are encountered in service, imposing cyclic strains in the solder joint due to the mismatch of CTE. In contrast, isothermal fatigue involves imposition of mechanical strains at a constant temperature. The testing methods of thermomechanical fatigue are divided into

four types depending on how the temperature is cycled and how the strain is imposed [70].

- Thermal cycling of actual component
- Thermal cycling of simplified specimen
- Thermomechanical fatigue of bulk solder
- Thermomechanical fatigue of solder joint

Thermal cycling of actual component uses circuit boards as test vehicles for solder joints. The whole electronic assembly is thermally cycled to impose strains on the solder joints by the difference in CTE between the joined materials. The great advantage of this technique is that the resistance to fatigue damage can be directly evaluated for a given assembly system by monitoring the electrical and thermal continuity as a function of the number of cycles. A difficulty with this method is that the strain and stress states in the solder joints are very complex due to the specific geometry of the solder joints, which makes the measurement and analysis of mechanical properties very difficult.

The time-temperature profile used in thermal cycling of actual component is usually one of the three patterns illustrated in Figure 2.18 ; sine wave, sawtooth, and sawtooth with hold times [71]. There are also three ways to apply temperature to the electronic assembly ; thermal shock, thermal cycling, and power cycling. In thermal shock mode, the solder joints are cycled with extremely short ramp times and some hold time at the temperature extremes, resulting in very rapid deformation rate due to the rapid transfer of heat. This could damage some electronic components. However, this is an easy test to perform and accelerated results are achievable. In thermal cycling mode, the temperature is cycled with a moderate ramp time to temperature extremes. Heat is transferred less

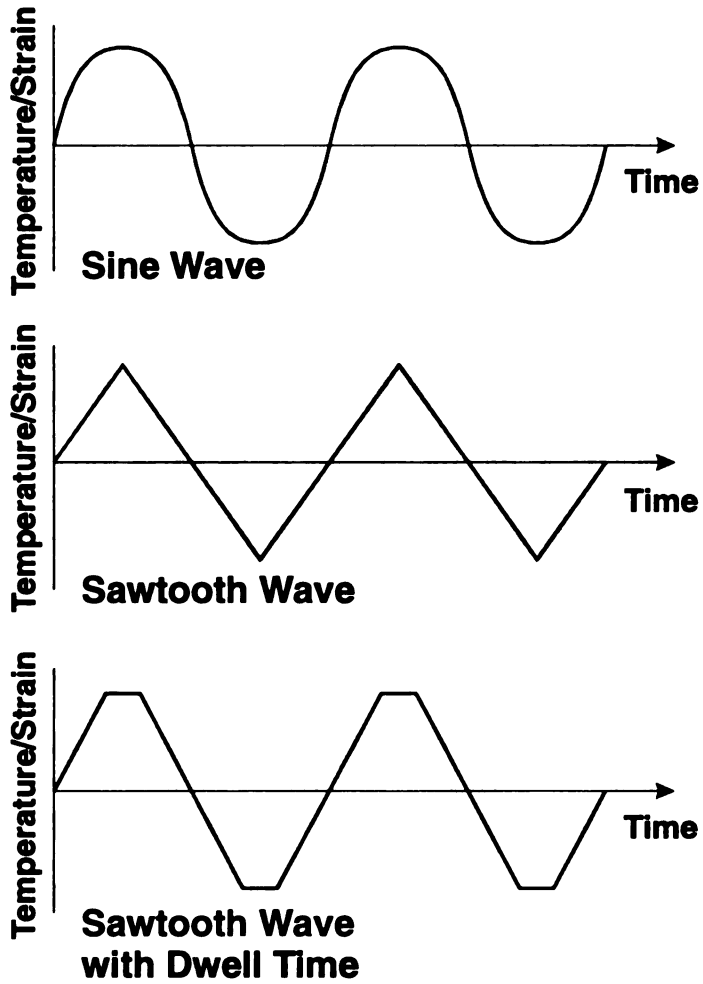

Figure 2.18 Schematic illustration of the three time-temperature profile in thermal cycling. In these cycles, the strain and temperature follow one another [71].

rapidly and the deformation rate is slower than in thermal shock mode, resulting in reduced possibility of damage of the solder joints during testing. Power cycling is conducted by turning the electronic device on and off. The high temperature portion of the cycle is generated by dissipating heat out of the package and into the solder joints when the device is turned on. The low temperature portion is typically room temperature or the temperature of the device when it is turned off. Power cycling is considered as the primary source of thermomechanical fatigue, especially for consumer electronics [72].

Thermal cycling of a simplified specimen avoids the problem of complex strain distributions in actual solder joints by employing a specimen with simplified state of strain. Prototype solder joints are made by soldering materials of different thermal expansion and thermally cycled between two temperature extremes. Figure 2.19 shows a simplified test specimen to impose shear strain on the solder joint [73]. Normally the strain imposed is either in simple shear or in a tension-compression orientation, as defined by sample geometry. The advantage of this type of testing is the simplified strain state in the solder joint such that microstructural evolution and failure characterization can be studied easily. However, characterization of mechanical properties and the number of cycles to failure is practically difficult in this method.

Thermomechanical fatigue of bulk solder is performed by externally applying strains and temperature cycle simultaneously. Lawson applied this method to bulk solders in flat dogbone design [74]. The temperature was cycled by generating heat by radio-frequency heating coils in the grips and by forcing refrigerated freon through machined chambers in the grips that hold the specimen. A tension-tension strain was imposed by a load-frame. The advantages of this method are that a simplified tension-

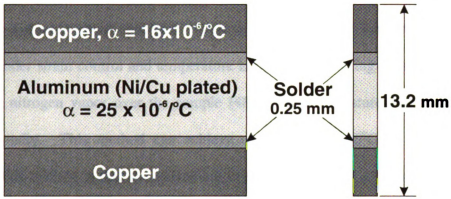

Figure 2.19 Simplified test specimen used by Tribula *et al.* to impose shear strain on the solder joints [73].

tension strain state can be achieved and mechanical data can be obtained during testing. This method is similar to isothermal fatigue testing method so that a correlation between thermal and isothermal fatigue can be made. However, the specimen used in this method is fairly massive compared to a small solder joint, and it is most easily tested in tension-tension mode, and not in shear mode.

Thermomechanical fatigue of solder joints attempts to collect mechanical data from smaller scale solder joint having a simplified strain state. Frear proposed a testing method using a double shear specimen where a servo-hydraulic load-frame imposes cyclic strain under strain control and temperature is cycled by blowing resistively heated air and liquid nitrogen vapor over the sample [48]. The temperature and strain were controlled digitally. This method can achieve cycling from –55°C to 150°C. The advantage of this method is that the strains are in simple shear and mechanical data are easily measured with the load-frame. The drawback of this method is that the test is very difficult because it is time consuming and needs special gas handling equipment and control systems to be coordinated with the load-frame system.

2.4.3 Fatigue Properties of Eutectic Sn-Ag Solder and Solder Joints

2.4.3.1 Isothermal Mechanical Fatigue

The database of mechanical and fatigue properties of solder materials have been established based on Sn-Pb solders during the past decade. However, those for lead-free solders are still far from complete. Coffin-Manson low cycle fatigue law was often used in the analysis of fatigue properties of bulk solders or solder joints. The form of Coffin-Manson relation,

$$N_f^{\alpha}\Delta\varepsilon = C,$$

where N_f is the number of cycles to failure, $\Delta\varepsilon$ total or plastic strain range, and α and C are materials constants, has been frequently used to predict solder fatigue lifetimes [75]. The load drop in the hysteresis loop was considered to be correlated with the development and growth of fatigue cracks and used as a measure of the fatigue failure [75-76]. The load drop was characterized by the load drop parameter Φ given by,

$$\Phi = 1 - \left(\Delta P / \Delta P_m \right),$$

where ΔP is the load range at any number of cycle and ΔP_m is the maximum load range.

Solomon [75] performed isothermal mechanical fatigue testing of single shear lap Sn-3.5Ag solder joints, which were made by soldering two brass or Cu blocks together, at 35°C and 150°C under plastic strain control. The microstructure of the solder joints consisted of primary Sn dendrites with interdendritic eutectic phases. All the loading was done with equal positive/negative plastic strain limit and loading rates (fully reversed ramp loading), and a cycling frequency of 0.3Hz with no dwell time at strain extremes. He examined load drop behavior from the hysteresis loop during fatigue testing and analyzed fatigue lifetime on the basis of a 50% load drop as a fatigue failure criterion.

Solomon observed the load drop after the first cycle, or at most, after a few cycles. It was found that the load drop followed a relationship of

$$\Phi = AN^B,$$

where N is the number of cycles, A and B are constants. B was measured to be 0.5 for Sn-3.5Ag solder joints, so it was predicted that the crack growth rate will decrease as cycling progresses and cracks grow larger. Figure 2.20 shows the comparison of fatigue lives of Sn-3.5Ag and Sn-40Pb solder joints at 35°C and 150°C using 50% load drop failure criterion. The number of cycles to failure was decreased with increasing plastic strain range, following a Coffin-Manson low cycle fatigue law. The fatigue life of both solders was lower at 150°C. At all strain ranges, the Sn-3.5Ag solder exhibited longer fatigue life at both temperatures except that Sn-40Pb solder showed longer fatigue life at the lowest strain range at 150°C. The fracture of the Sn-3.5Ag solder joints was observed to occur by ductile hole growth and coalescence, which were more prevalent at 150°C.

Guo *et al.* [76] conducted isothermal mechanical cycling testing at room temperature on the Sn-4Ag and Sn-37Pb single lap solder joint specimens. Testing was performed under constant total shear strain control ($\Delta\gamma$ = 0.04 ~ 0.79), fully reversed ramp cycling, and 0.1 Hz cycling frequency without dwell time at strain extremes. In their study, the fatigue life was estimated using a 50% load drop criterion and the crack growth rate was examined using load drop behavior in hysteresis loop during fatigue testing.

Guo *et al.* compared the fatigue lives of the Sn-4Ag and Sn-37Pb solder joints at 50% load drop failure criterion as shown in Figure 2.21. The data followed the Coffin-Manson type relation. The Sn-4Ag solder joint exhibited a higher fatigue resistance for high strain ranges ($\Delta\gamma \geq 0.1$) while it had lower fatigue resistance at low strain ranges compared to Sn-37Pb solder joint. The relative fatigue resistance given for the load drop Φ = 50% also occurred at other values of Φ.

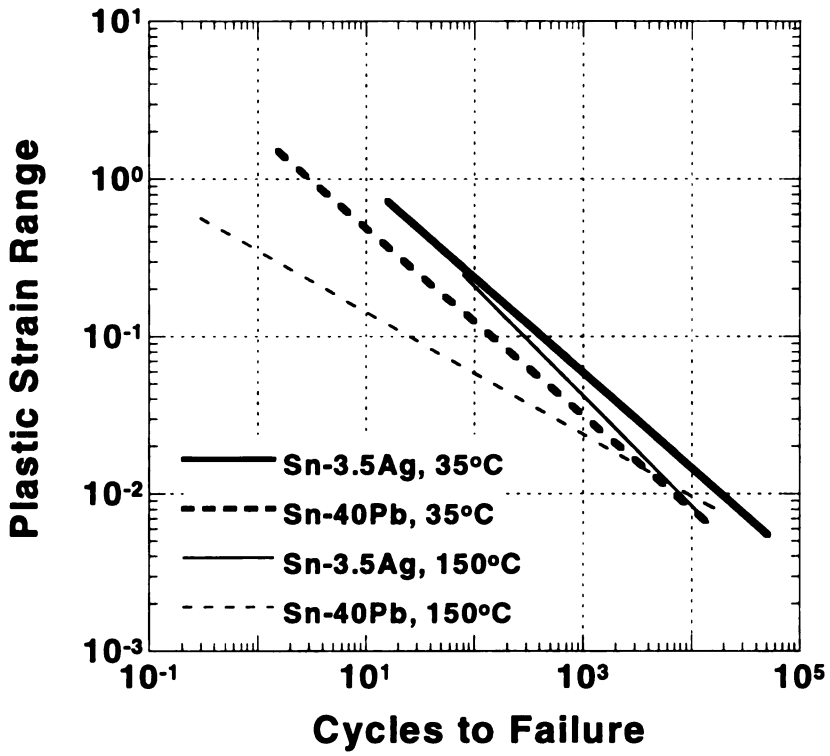

Figure 2.20 Comparison of the fatigue life behavior of Sn-3.5Ag and Sn-40Pb solder joints at 35°C and 150°C using a 50% load drop failure criterion [75].

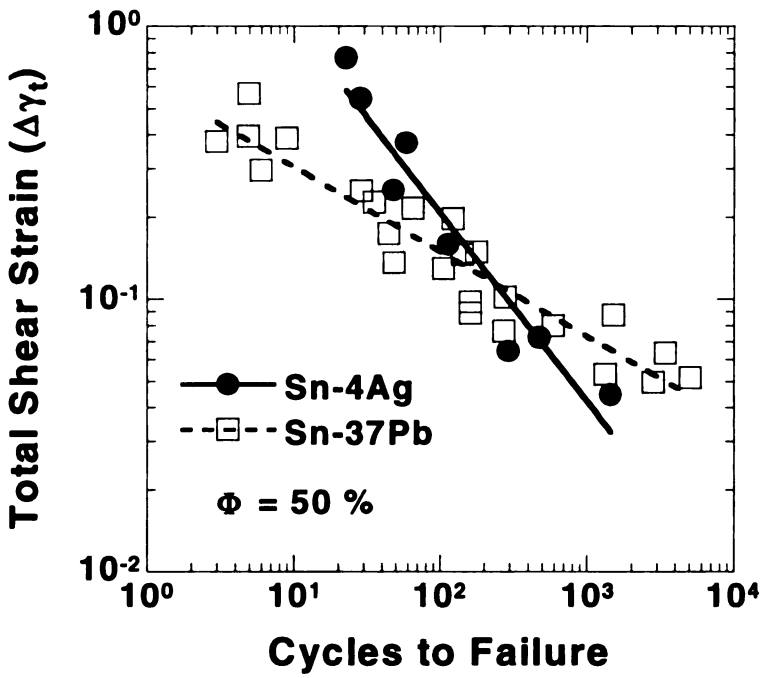

Figure 2.21 Comparison of fatigue lives of Sn-4Ag and Sn-37Pb solder joints at room temperature using 50% load drop failure criterion [76].

Guo *et al.* proposed that the fraction of the fatigue-cracked area is directly proportional to the load drop as follows

$$\Phi = A_c / A_o ,$$

where A_c is the cracked area and A_o the original area. It indicated that the shear stress ($\Delta\tau$) acting on the solder joints remains essentially constant throughout a fatigue test with a given $\Delta\gamma$. Further, an estimation of the crack growth rate was obtained from the estimate of the rate of crack area growth, which then can be obtained from the change in the load drop with number of cycles. By taking an approximation for an average crack length (a_c) given by,

$$2a_c = A_c^{1/2} ,$$

the crack growth rate was estimated by

$$\frac{da_c}{dN} = \frac{(A_o\Phi)^{1/2}}{4N} \frac{d\log\Phi}{d\log N} .$$

Figure 2.22 shows a plot of the crack growth rate (da_c/dN) versus stress intensity parameter ($\Delta K_{II} = \Delta\tau\sqrt{\pi a_c}$) as s function of Φ for the Sn-37Pb solder joints. The Sn-4Ag exhibited the similar behavior in crack growth rate. For a constant $\Delta\gamma$, da_c/dN decreased with increasing Φ, i.e. the crack growth rate became smaller as the total crack area (A_c) increased. This finding corresponds to Solomon's prediction on the crack growth rate [75]. On the other hand, for a constant Φ (i.e. constant A_c), da_c/dN increased with increasing $\Delta\gamma$, i.e. with increase in $\Delta\tau$ or ΔK_{II}. A comparison of the crack growth rate at Φ = 50% is given in Figure 2.23 for the Sn-4Ag and Sn-37Pb solder joints.

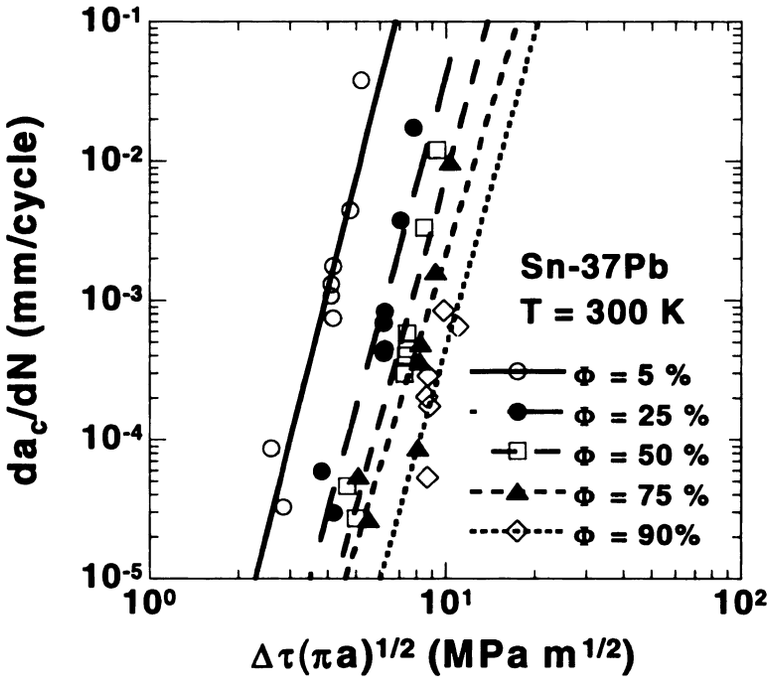

Figure 2.22 Fatigue crack growth rate (da_c/dN) versus stress intensity factor ($\Delta\tau\sqrt{\pi a}$) as a function of Φ for Sn-37Pb solder joints [76].

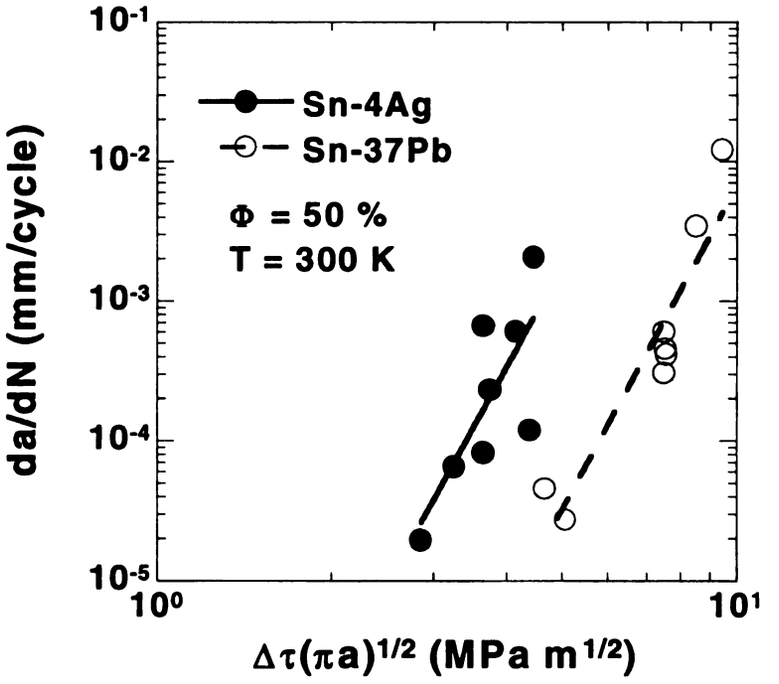

Figure 2.23 Comparison of the crack growth rate at Φ = 50% for the Sn-4Ag and Sn-37Pb solder joints [76].

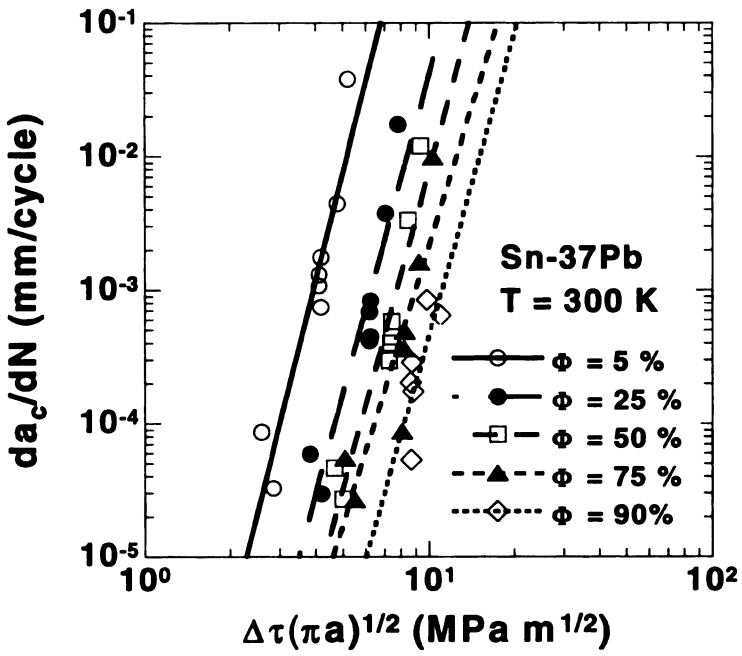

Figure 2.22 Fatigue crack growth rate (da_c/dN) versus stress intensity factor ($\Delta\tau\sqrt{\pi a}$) as a function of Φ for Sn-37Pb solder joints [76].

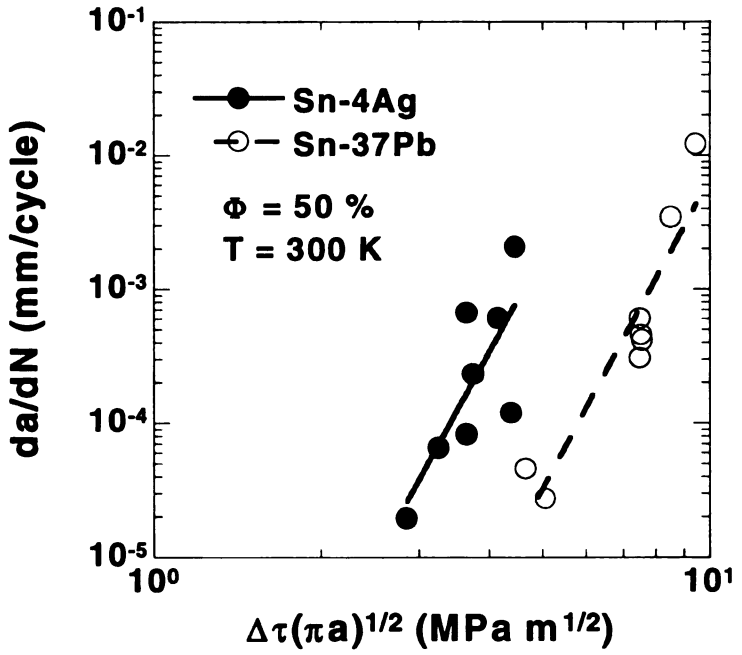

Figure 2.23 Comparison of the crack growth rate at Φ = 50% for the Sn-4Ag and Sn-37Pb solder joints [76].

Apparently, the Sn-4Ag solder joints exhibited a higher crack growth rate for all strain ranges studied. Thus it was suggested that the superior fatigue resistance of Sn-4Ag solder joint at large strain ranges shown in Figure 2.21 is due to a higher resistance to crack initiation.

Mavoori *et al.* [65, 77-78] tested the dogbone shaped bulk specimen of Sn-3.5Ag and Sn-37Pb solders which were heat treated at 150°C for 24 hours followed by aging at room temperature for a week. The specimens were tested for isothermal fatigue under uniaxial loading and total strain control conditions ($\Delta\varepsilon_t$ = 0.002 ~ 0.02) at 25°C and 80°C in sawtooth pattern. The ramp time of 1 sec to strain extremes (i.e. 0.5 Hz cycling frequency) was employed for tests with/without dwell time at maximum strain except for tests where the ramp time was a variable. In their study, the number of cycles prior to 50% reduction in σ_{max} was used as a failure criterion (same fully reversed ramp cycling as that used by Solomon [75] and Guo *et al.* [76] because Mavoori *et al.* used initial cross section for stress calculation.

As shown in Figure 2.24, Mavoori *et al.* observed that the fatigue lives of the Sn-3.5Ag solder was longer than that of Sn-37Pb solder in the test without dwell time at 25°C, following the Coffin-Manson type relation. However, the fatigue lives were comparable at very low strain ranges. Figure 2.25 shows the effects of dwell time on the fatigue lives during tests with $\Delta\varepsilon_t$ = 0.006 at 25°C. An increase in tensile dwell time dramatically reduced the number of cycles to failure. Beyond a certain dwell time, there was no further reduction in the number of cycles to failure. The effect of dwell time is greater for the Sn-3.5Ag solder. Figure 2.26 shows the effect of ramp time on the fatigue lives during tests with $\Delta\varepsilon_t$ = 0.01 and no dwell time at 25°C. Increasing time per cycle

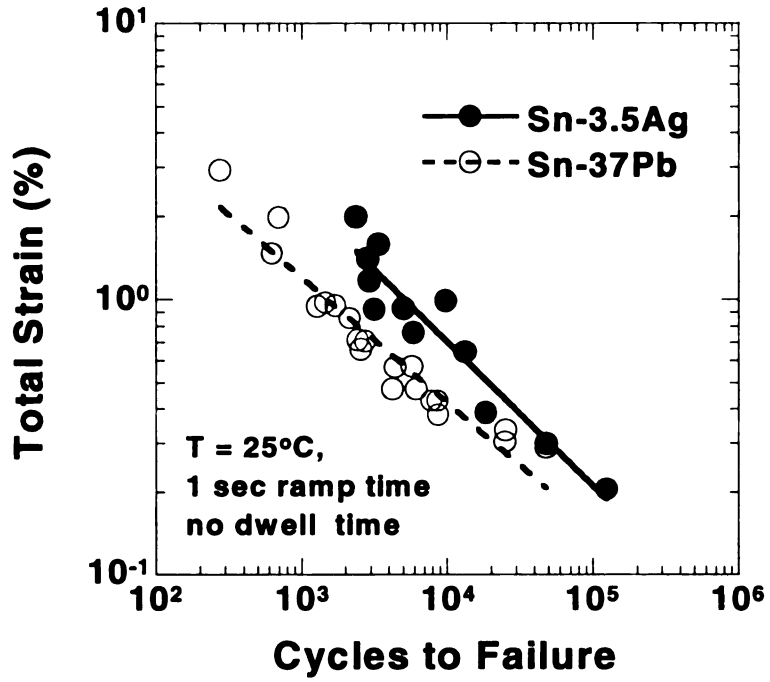

Figure 2.24 Fatigue lives of Sn-3.5Ag and Sn-37Pb bulk solders at 25°C and with 1 sec ramp time and no dwell time using 50% σ_{max} [77]

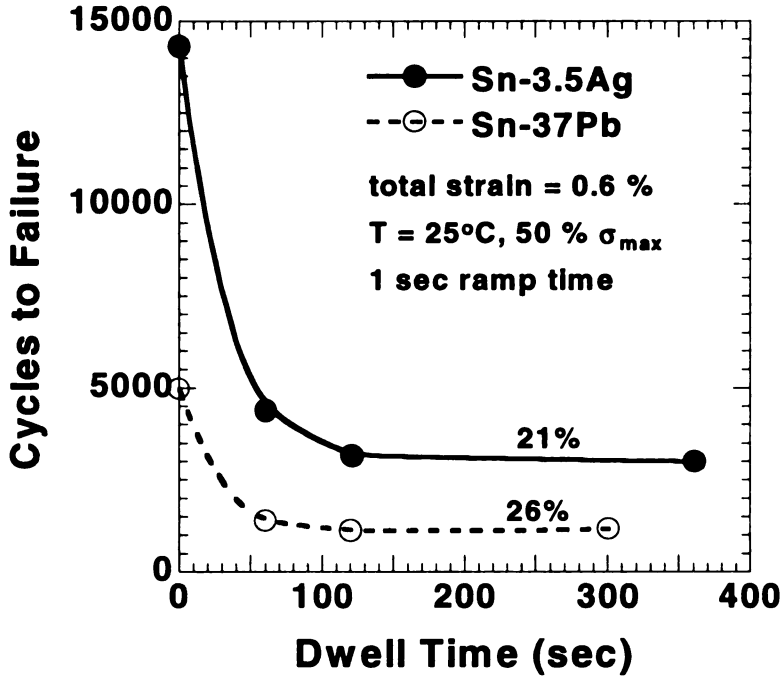

Figure 2.25 Effect of dwell time on the fatigue lives using 50% σ_{max} failure criterion during tests with $\Delta\varepsilon_t$ = 0.006 and 1 sec ramp time at 25°C [77].

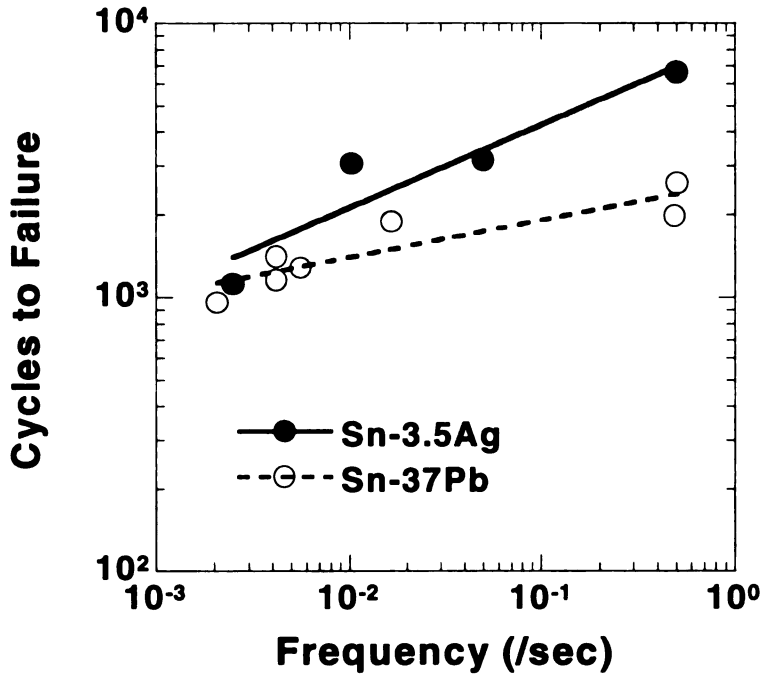

Figure 2.26 Effect of ramp time (frequency) on the fatigue lives during tests with $\Delta\varepsilon_t = 0.01$ and no dwell time at 25°C [78].

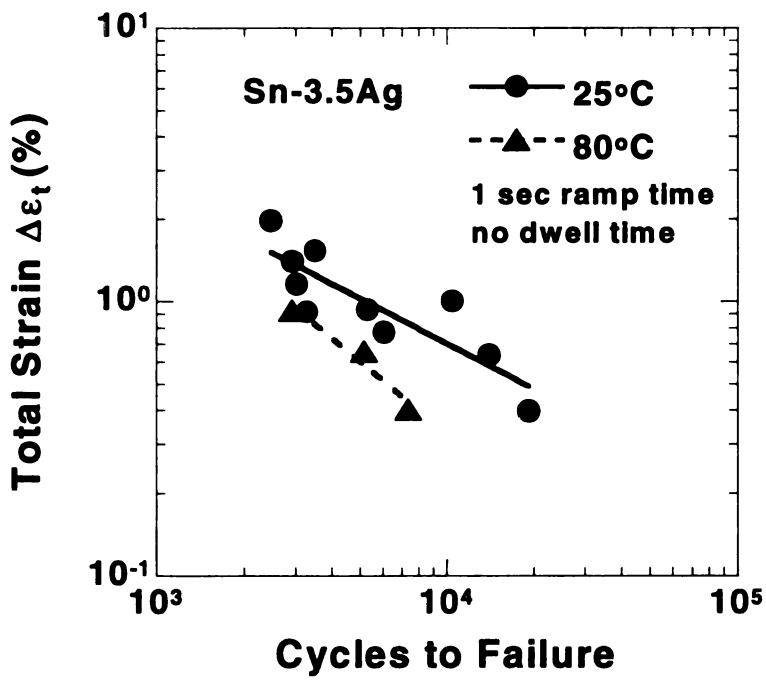

Figure 2.27 Effect of temperature on fatigue lives of Sn-3.5Ag solder during tests with 1 sec ramp time and no dwell time [78].

in tests without dwell time (i.e. decrease in cycling frequency and reduction of strain-rate) led to a reduction in the umber of cycles to failure. The fatigue lives of the Sn-3.5Ag solder were more sensitive to the ramp time variable than Sn-37Pb solder. The effect of temperature was to reduce the number of cycles to failure with increasing temperature as shown in Figure 2.27. There appeared to be a greater reduction at lower total strain ranges.

2.4.3.2 Thermomechanical Fatigue

As with studies for Sn-Pb solders, the fatigue studies on the Sn-3.5Ag solder concentrated on the assessment of the fatigue lifetime or resistance using Coffin-Manson type relationships in the analyses. These approaches were criticized by Winterbottom [2] in his work where the deformation process in the actual solder joint was studied using a thermal cycling profile similar to that in real service condition and simulated using a nonlinear finite element analysis. A number of geometric and microstructural features in the actual solder joint complicate the deformation process. He has also pointed out that the number of cycles to failure can be influenced by the frequency of temperature cycling, temperature extremes, ramp times, dwell times, and the magnitude of the strain ranges. It has become apparent that such a simple model as Coffin-Manson relation is an over-simplification in assessment of fatigue life of the actual solder joints and a more accurate model is needed for more accurate life predictions.

Several important results were obtained from the analysis of Winterbottom's simulation study on deformation process, which were verified in experimental results. The first feature was that the distribution of the accumulated strain in the solder joint was

inhomogeneous and highly localized depending on the joint geometry. This does not support the uniform strain assumption throughout the simplified solder joints or bulk solders employed in application of the Coffin-Manson type relation. The localized strain accumulation at certain locations suggested that the crack initiation and propagation processes would be more appropriate for predicting fatigue lifetime than an approach assuming uniform strain based on global displacements. Secondly, the deformation produced during the heating and cooling regimes of the thermal cycling was not reversible but produced continually changing distortion and strain distributions. As a result, the joint shape and the stress distribution changed irreversibly as well. This behavior implied that isothermal fatigue testing couldn't reveal exactly the failure mechanism, i.e. the cracking process, induced by thermal cycling. The nucleation and propagation of fatigue cracks were observed to further alter the distribution of strain and stress. Thirdly, the comparison of accumulated strain induced by time-independent plastic deformation and time-dependent creep deformation provided insight into the cracking process for fatigue failure. The crack trajectory in the solder joint was found to pass through the regions having greatly accumulated plastic strain and very little creep strain. With inputs from the study on deformation process, a failure criterion was taken as follows. Once a critical strain density is reached at a location in the solder joint, a crack is nucleated and extended. The solder joint will fail when the cracked area reduces the joint strength below that required to support the imposed load.

In the earlier study using actual solder joints by Harada *et al.* [51], controlled-collapsed chip joints (flip chip) of Sn-3.5Ag solder between two ceramic chips, whose solderable area was plated with Ni/Au, were used. The solder joints were thermally

cycled between –50°C and +150°C in a thermal shock mode with 30 min dwell at each temperature in air, i.e. a cycle/hour. Figure 2.28 schematically illustrates the geometry of the solder joint and cracking in the solder joint. Fine fatigue striations with intervals of 0.04 ~ 0.2 μm were observed on the fracture surface. These striations were considered as the crack length created during each thermal fatigue cycle, so the intervals of striations were used to estimate fatigue crack growth rate. As the crack propagated during thermal cycling, the striation interval increased. Thus, the crack growth rate increased with increasing number of cycles, contrary to the results in the study using single shear lap solder joints by Guo *et al.* [76] and Solomon [75]. This was attributed to reduced the effective joint area that increased the stress during thermal cycling. It indicates that the load did not decrease during thermal cycling, resulting in the increasing stress because of the reducing joint area. This is contrary to load drop behavior observed in strain-controlled isothermal mechanical fatigue that estimated a constant shear stress ($\Delta\tau$) acting on the solder joints throughout a fatigue test. The striation intervals in the fracture surface of Sn-3.5Ag solder joint were generally about a half of those of Sn-37Pb solder, indicating the Sn-3.5Ag solder to have about twice fatigue life of Sn-37Pb solder for the same joint geometry.

Frear [48] used the double lap shear Sn-3.5Ag solder joint in his TMF tests where the cyclic strain and temperature were imposed simultaneously. The temperature range was –55°C to +125°C and a total of 10% shear strain was imposed at a deformation rate of 2.9×10^{-4}/sec. The Sn-3.5Ag solder joint had a slightly longer fatigue lifetime than the Sn-40Pb solder joint tested under the same condition. The Sn-3.5Ag solder joints failed by intergranular cracking at Sn-Sn grain boundaries.

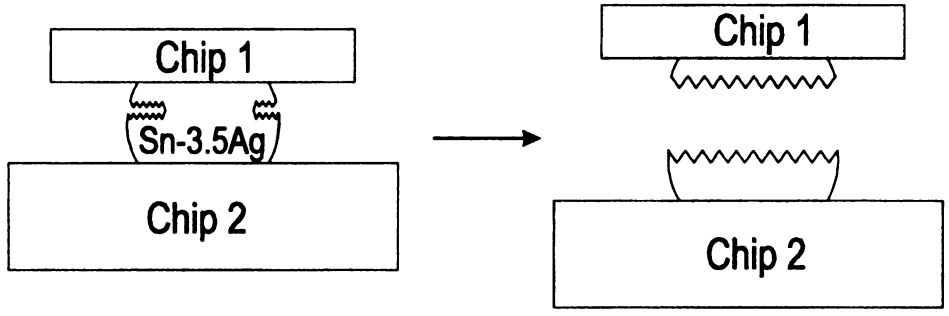

Figure 2.28 Schematic illustration of geometry of and cracking in the controlled-collapsed chip (flip chip) Sn-3.5Ag solder joint [51].

Shangguan [79-80] tested Sn-3.5Ag solder joints made by soldering surface mount leadless ceramic chip resistors to Cu pad on printed wiring board substrates. The solder joints were cycled in air under thermal shock mode between –40°C to +125°C with 18 minutes dwell time at each temperature extreme up to 1500 cycles. Figure 2.29 illustrates the geometry of the solder joint and the crack propagation through the solder joint. The cracks initiated at a location in the end of the component termination between 250 and 500 cycles. The cracks then propagated through the stand-off region towards the end fillet region. Once the cracks reached the end of the component, they propagated either upward along the component termination or along an approximately 45° direction in the end fillet. The length of crack which propagated during every 250 cycles was measured and the average crack growth rate was calculated by dividing the crack length increment by the number of cycles (250 cycles). Figure 2.30a and b show the crack length as a function of number of cycles and average crack growth rate, respectively. The crack initiation took place between 250 and 500 cycles. Initial crack growth rate was rapid and then became slow once the crack reached the end of the component. The crack growth rate significantly decreased in the end fillet region to 0.18 μm/cycle between 1250 and 2500 cycles. It is thought to be due to the large volume of solder in end fillet region compared to that in the stand-off region.

In the case of solder joints with leadless surface mount component, the crack initiation and growth greatly depended on the geometry of the solder joint and volume of the solder. The crack initiation did not appear to be the major portion of fatigue life. The slow crack propagation rate in the end fillet region of the solder joints significantly extended the total life of the solder joint. Since the crack initiated in the end of the

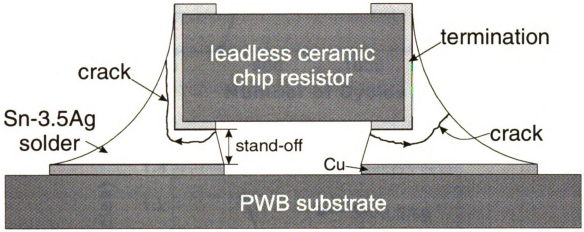

Figure 2.29 Geometry of the surface mount leadless Sn-3.5Ag solder joint and the crack propagation through the solder joint [79].

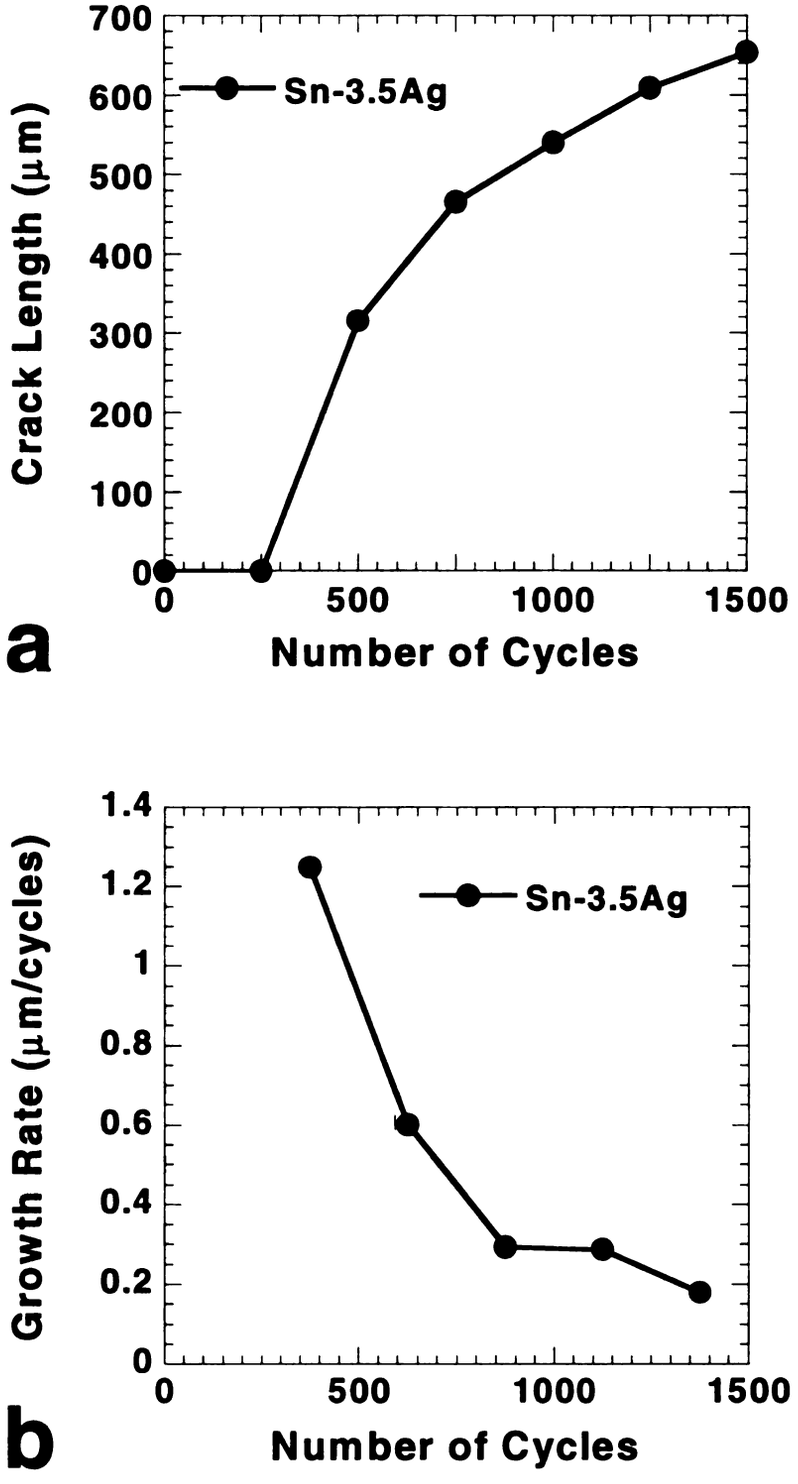

Figure 2.30 (a) Crack length as a function of number of cycles, and (b) crack growth rate in surface mount leadless Sn-3.5Ag solder joint [79].

component termination and rapidly propagated through thin stand-off region, it is critical to increase the stand-off height to delay crack initiation and growth. The cracking and fracture process of the solder joint in this study were identical to the criterion determined in the work of Winterbottom [2].

Fatigue properties of solder joints have been analyzed using measured fatigue data from bulk solder and simplified joint specimen. The fatigue deformation of those specimens was characterized using a Coffin-Manson type relationship. However, it is difficult to directly apply the fatigue data obtained from bulk solder and simplified specimen to actual modules. This is mainly due to several other factors such as geometry, complicate stress-strain state, microstructure, etc. Furthermore, there is no microstructural characterization of fatigue deformation and damage. Fatigue properties of solder joints should be examined incorporating distinct parameters related to each specific type of solder joint to estimate the fatigue resistance or lifetime of solder joints. The fatigue resistance of solder joints can be improved by optimizing geometry of solder joints. Eventually, the performance of solder joints during thermomechanical fatigue can be maximized by microstructural control of solder joints toward deferring fatigue damage. Thus, as with studies of Sn-Pb solder joints, detailed microstructural study on fatigue deformation and damage is required to better understand the fatigue properties of Sn-Ag solder joints.

2.5 INTERFACIAL INTERMETALLIC COMPOUND (IMC) LAYERS

The Sn-based solders form the interfacial intermetallic compound (IMC) layers at the solder/substrate interface during soldering due to the reaction of Sn and the substrate elements. The IMC layers grow by means of solid state diffusion and continued reaction of Sn and substrate elements during service. In the case of the Cu substrates extensively used in electronic applications, two IMC layers of Cu_6Sn_5 and Cu_3Sn are formed at the solder/substrate interface [81-85]. Only the Cu_6Sn_5 layer was found to form during soldering and Cu_3Sn layer is usually found only after aging at elevated temperatures [81-86].

The physical properties of intermetallic compounds contrast significantly with those of solder or the substrate materials. Intermetallic compounds are less ductile, and less thermally and electrically conductive. Table 2.4 provides physical properties of Cu-Sn intermetallic compounds along with those of Cu and Sn for comparison [87-88]. The intermetallic compounds used to generate this data were produced by rapid solidification by supersonic, inert gas, metal atomization, and resulted in fine-grained single phase. The hardness is greater for the intermetallic compounds, indicating their greater brittleness. With these higher values of hardness for the intermetallics, no plastic deformation would be expected under normal levels of stress acting on the solder joints. The elastic modulus is likewise greater for the intermetallics, and intermetallics usually have a low ductility. However, the coefficients of thermal expansion for the intermetallics are similar to that of Cu and Sn. Thus, it appears that the intermetallics would expand and contract much like their associated substrate material. Thermal and electrical conductivities are generally lower for the intermetallics, but they are considered

Table 2.4 Room temperature physical properties of intermetallics [87-88].

Properties	Cu_6Sn_5	Cu_3Sn	Cu	Sn
Vickers Hardness (kg/mm^2)	378 ± 55	343 ± 47	30	100
Toughness ($MPa \cdot m^{-1/2}$)	1.4 ± 0.3	1.7 ± 0.3		
Youngs Modulus (GPa)	85.56 ± 1/65	108.3 ± 4.4	117	41
Shear Modulus (GPa)	50.21	42.41		
Thermal Expansion ($x\ 10^{-6}/°C$)	**16.3 ± 0.03**	**19.0 ± 0.3**	**17.1**	**23**
Thermal Diffusivity (cm^2/sec)	0.145 ± 0.015	0.24 ± 0.024		
Heat Capacity (J/gm/deg)	0.286 ± 0.012	0.326 ± 0.012	0.385	0.227
Resistivity (μohm-cm)	17.5 ± 0.1	8.93 ± 0.02	1.7	11.5
Density (gm/cc)	8.28 ± 0.02	8.9 ± 0.02	8.9	7.3
Thermal Conductivity (watt/cm-deg)	0.341 ± 0.051	0.704 ± 0.098	3.98	0.67

as minimal problems for a thin intermetallic layer.

While the formation of the IMC layers ensures the firm bonding of a solder joint, the resulting thickness of the IMC layer is of significant concern to the reliability of the solder joint. Two major concerns related to the IMC layer are the solderability loss and the degradation of mechanical properties [81-85]. The solder pads of printed wiring board and component termination are usually pre-coated with pure Sn or Sn-Pb solder as a solderable metallization to improve their solderability during manufacturing. The coating process also creates IMC layers, which in turn grow during storage. Consumption of the solderable metallization due to the growth of the IMC layers in the solid state during storage can strongly affect subsequent solderability. The degradation of the mechanical properties is due to the embrittlement of the joint with excessive growth of the IMC layers during service.

Frear *et al.* [48, 82] reported that the fracture toughness of the Sn-3.5Ag solder joint was drastically decreased below a half of that of as-solidified one when the IMC thickness increased up to 25 μm. They also found that the fracture of the Sn-3.5Ag solder joint was dependent on the IMC thickness. In the as-solidified condition with about 1.24 μm Cu_6Sn_5 IMC layer, the failure occurred via interfacial separation at the solder/IMC interface, while the fracture propagated through the 4.5μm Cu_3Sn layer after aging 10 days at 205°C. After 205°C for 25 days, the fracture occurred through a 37.8μm Cu_6Sn_5 layer.

Yang *et al.* [15] showed the effects of IMC layer thickness on the mechanical properties using the Sn-3.5Ag solder joints produced by two different reflow times of 20 and 1000 minutes during soldering. The solder joint reflowed for the longer time

exhibited no ductility in tensile test and significantly reduced strain at failure during creep compared to that reflowed for short time. The solder joints with long reflow time showed brittle fracture through IMC layer, while the solder joints reflowed for a short time failed in the bulk solder.

The growth kinetics of the IMC layers in liquid and solid state was examined in many studies. The growth of two IMC layers, Cu_6Sn_5 and Cu_3Sn, in solid state occurs in planar manner by the diffusion of Sn and Cu in opposite direction. As in Sn-Pb solder [89-90], the solid state growth of IMC layers in the Sn-3.5Ag solder joint exhibited a diffusion-controlled growth characterized by the model,

$$x = x_o + \sqrt{Dt},$$

where x_o is the initial thickness, x is the IMC layer thickness at time t, and D is IMC layer growth rate constant [81, 82, 91]. However, Frear *et al.* [82] observed that the IMC layers grew following $t^{0.35}$ dependence instead of $t^{1/2}$ during aging at 205°C, suggesting a different mechanism controlling IMC layer growth at high temperature.

For liquid state growth of IMC layers during soldering, Blair *et al.* [84] observed the dependence of $t^{1/2}$ of IMC layer growth at temperature ranges of 228 ~ 326°C and for reflow times from 10 to 120 sec. However, London *et al.* [83] observed the $t^{1/3}$ dependence of IMC layer growth during soldering in the study using 240 ~ 360°C temperature ranges and reflow time up to 216 hours. Choi *et al.* [86] observed that only Cu_6Sn_5 layer was formed for reflow time less than 120 sec, while two layers of Cu_6Sn_5 and Cu_3Sn were formed when the reflow time was more than 120 sec. The difference in

results between Blair *et al.* and London *et al.* appears to be due to the formation of Cu_3Sn layer when longer reflow time was used, affecting the grow rate of the total IMC layer.

2.6 EFFECTS OF REINFORCEMENTS

Several types of reinforcements have been used in attempts to improve mechanical properties of the solder materials. The types of the reinforcement studied include carbon fiber, metallic elements such as Cu, Ni, Au, Ag, Fe, In, and Sb, and intermetallic compound particles such as Ni_3Sn_4, Cu_6Sn_5, and Cu_3Sn. The intermetallic particles were incorporated directly in the solder materials or by *in-situ* method [25, 26, 92-94]. While the effects of reinforcements on the Sn-Pb solder were extensively studied [89-90, 93-106], the studies using Pb-free solder are only a few. In the case of Sn-3.5Ag solder, only some metallic elements and intermetallic particles by *in-situ* method were attempted [5, 21, 25-26, 48, 92, 107-109]. For Pb-free solders, the reinforcements were incorporated not only to improve mechanical properties but also to match the melting temperature of the eutectic Sn-Pb solder.

For the eutectic Sn-3.5Ag solder, the metallic elements were incorporated to reduce the 221°C melting temperature because it is too high to apply directly to manufacturing processes. Miller *et al.* [107] found a ternary eutectic Sn-4.7Ag-1.7Cu which melts at 216.8°C. Further alloying with Sb resulted in a newly invented solder alloy, CASTIN, Sn-2Ag-0.8Cu-0.6Sb, with melting range of 210 ~ 217°C [108]. Frear [48] extensively studied the ternary Sn-4.7Ag-1.7Cu for creep, solid state IMC layer growth, TMF deformation under the same condition as those used for Sn-3.5Ag solder. The microstructure of the ternary Sn-4.7Ag-1.7Cu was similar to the eutectic Sn-Ag solder

except having additional Cu_6Sn_5 intermetallic particles. The ternary Sn-4.7Ag-1.7Cu alloy exhibited very similar deformation behavior to the Sn-3.5Ag solder, with the stress exponent of 6 in creep, decreasing fracture toughness with increasing IMC layer, and similar number of cycles to failure during TMF. The small addition of Cu did not have any substantial effects on mechanical properties of the Sn-3.5Ag solder.

McCormack *et al.* [21] examined two ternary alloys, Sn-3.5Ag-5In and Sn-3.5Ag-5 Bi, produced by incorporating In or Bi into Sn-3.5Ag solder. They obtained a reduced melting temperature of 213°C and 212°C for the In and Bi additions, respectively. Both types of additions strengthened the alloys at small strain ranges, but they severely degraded the maximum strain limit that the alloy can withstand, showing a brittle fracture. This was attributed to the segregation of In and Bi in Sn phase. They also examined the ternary alloys Sn-3.5Ag-1Zn with a reduced melting temperature of 217°C [5]. This alloy showed increased 0.2% offset yield stress, ultimate tensile strength, and comparable elongation to the Sn-3.5Ag solder. It also exhibited significant creep resistance with creep strain more than an order of magnitude smaller than Sn-3.5Ag solder. The improvements of mechanical properties were interpreted in terms of microstructural refinement. The added Zn suppressed the soft primary Sn phase and refined Ag_3Sn particles resulting in very fine and uniform two phase microstructure. Zn was found exclusively within the Ag_3Sn phase. It appears that Zn affected the microstructure of primary Sn phase by refining Ag_3Sn particles which may provide nucleation sites of Sn phase.

Kariya *et al.* [109] investigated the effects of Cu and Bi on Sn-3.5Ag solder with up to 1% Cu and 5% Bi addition during TMF using actual solder joint with Quad Flat Pack

(QFP) leads. They found that the increased addition of Bi drastically degraded the thermal fatigue resistance of Sn-3.5Ag solder. They attributed the degraded performance to the formation of Bi precipitates in Sn phase when more than the solubility limit of 2 mass% Bi in Sn was exceeded. The Cu addition did not change significantly the thermal fatigue property of the Sn-3.5Ag solder.

The effects of reinforcements have been investigated on physical properties (e.g. melting temperature), mechanical properties (e.g. creep, fatigue, and tensile), and microstructure. However, there are very few studies about effects of reinforcements on interfacial intermetallic layer growth. Furthermore, these studies were performed with Sn-Pb solders and time scales ranging to a few hundred hours. It is necessary to examine the effect of reinforcements on interfacial intermetallic layer growths during long-term ranging to several thousand hours.

CHAPTER 3

THERMOMECHANICAL FATIGUE BEHAVIOR OF Sn-Ag SOLDER JOINTS

ABSTRACT

Microstructural studies of thermomechanically fatigued actual electronic components consisting of metallized alumina substrate and tinned copper lead, soldered with Sn-Ag or 95.5Ag/4Ag/0.5Cu solder were carried out with an optical microscope and environmental scanning electron microscope (ESEM). Damage characterization was made on samples that underwent 250 and 1000 thermal shock cycles between –40°C and +125°C, with a 20 minute hold time at each extreme. Surface roughening and grain boundary cracking were evident even in samples thermally cycled for 250 times. The cracks were found to originate on the free surface of the solder joint. With increased thermal cycles these cracks grew by grain boundary decohesion. The crack that will affect the integrity of the solder joint was found to originate from the free surface of the solder very near the alumina substrate and progress towards and continue along the solder region adjacent to the Ag_3Sn intermetallic layer formed with the metallized alumina substrate. Re-examination of these thermally fatigued samples that were stored at room temperature after ten months revealed the effects of significant residual stress due to such thermal cycles. Such observations include enhanced surface relief effects delineating the grain boundaries and crack growth in regions inside the joint.

3.1 INTRODUCTION

The need for improving the structural performance of solder is increasing rapidly since solder joints that connect surface mounted electronic components are structural as well as electrical connections. The lack of detailed characterization of the realistic solder joint microstructure, and its evolution in service, especially in lead-free solders, represents a major hurdle to overcome before a solder microstructure that provides optimal service performance can be engineered and introduced into manufacturing settings. A highly recommended suitable alternative for Pb-bearing solders used in electronic applications, especially for higher temperature service conditions, is eutectic Sn-Ag solder. Such a solder under service environments like in automotive under-the-hood, aerospace, and military application will experience severe thermal excursions that will result in significant thermal stresses due to the thermal expansion mismatch between soldered components and the substrate. Although there have been studies [75,80,110-112,79,109] dealing with thermomechanical fatigue behavior of Sn-Ag solders, a microstructural evaluation to develop a basic understanding of the processes involved is far from complete.

Typically, manufactured solder joints have non-equilibrium casting microstructures with considerable porosity. As the Pb-Sn solder joint undergoes long term thermomechanical deformation, the microstructure coarsens heterogeneously and develops well defined phase boundaries, especially in highly stressed areas near the interface, and the coarsened regions are more susceptible to fatigue crack initiation [113,114,73]. In addition, a continuous, hard intermetallic layer forms at the solder/substrate interface. This layer and the constraints imposed by the substrate affect

the stress state and the deformation behavior in the solder joint [115,65]. When hold times between temperature changes are imposed, the number of thermal cycles to failure is substantially reduced [116-118]. There has been significant activity to model the complex stress histories that occur in solder joints in order to predict the failure processes. These analyses usually use mechanics based approaches for modeling the complex creep-fatigue conditions imposed by thermal cycling [110,119-124]. To develop suitable material models for reliability predictions, it is necessary to characterize the processes associated with microstructural evolution, particularly generation of microstructures that lead to plastic instability that stimulates the failure process to explore ways to prevent or retard damaging microstructural changes such as coarsening.

It is important to note that thermomechanical fatigue in Sn-Pb solders have been extensively investigated during the last decade. However, such a knowledge base cannot be directly applied to Sn-Ag solders because the phase fractions and solubility behavior of the two phases are distinctly different. Pb has high solubility for Sn but not vice versa, and the Pb rich phase is ductile, has a volume fraction near 30% in Pb-Sn solder ; in contrast to Ag_3Sn, which is hard and comprises only about 4% of the volume in Sn-Ag solder. The main aim of the proposed study is to investigate the thermomechanical fatigue damage in an actual electronic component assembly consisting of tinned copper lead soldered to metallized alumina substrate with Sn-Ag solders with or without Cu.

3.2 EXPERIMENTAL DETAILS

Several, as-made or thermally cycled electronic modules, containing chip components soldered to a rigid alumina substrate circuit board were examined during the

course of this investigation. Two types of solders, 96.5Sn/3.5Ag (eutectic Sn-Ag) and 95.5Sn/4Ag/0.5Cu, were used to connect the lead of chip component to the alumina substrate metallized with 99%Ag/1%Pt. The lead of the chip component was made of Cu and was plated with Ni/Sn or Sn-Pb.

Solder paste was screened to the solder pad on the metallized alumina substrate to a thickness of 150 ~ 200 μm. The circuit boards were then reflowed with a maximum temperature of 235 ~ 240°C for less than 20 sec in a nitrogen environment. Figure 3.1 shows a schematic drawing of the solder joint connecting the lead of the chip component to the substrate. The solder joints were subjected to thermal shock by cycling between –40°C and +125°C for 250 or 1000 cycles with a 20 minutes hold time at extreme temperatures. The two temperature extremes were chosen to represent the harsh conditions in the automotive under-the-hood environment [80, 2].

The initial examination of the surface appearance of the as-made and thermally cycled solder joints was carried out using optical microscopy and environmental scanning electronic microscopy (ESEM). Thereafter, the solder joints were mounted in epoxy resin, cross-sectioned using a diamond saw, and wet polished to 0.05mm finish using a SiO_2 colloidal suspension. Polished sections of the solder joints were examined with ESEM and energy dispersive spectroscopy (EDS). ESEM facilitated direct examination of the solder joint assemblies without additional preparation such as gold or carbon conductive coating that will be required for analysis in conventional scanning electronic microscopy [111, 125]. These solder joints were also reexamined using ESEM without any further treatments after about 10 months.

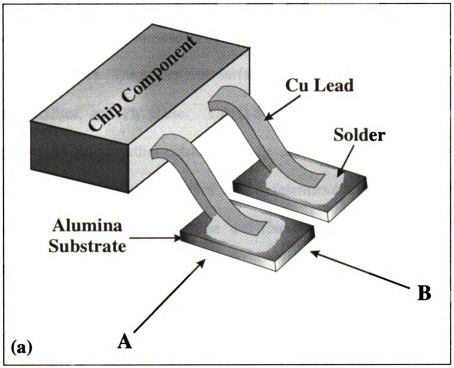

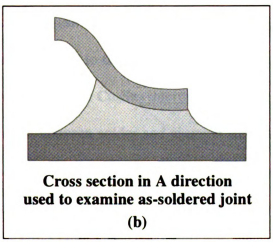

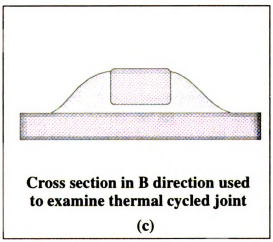

Figure 3.1 A schematic drawing of solder joint used in this study. The cross section in A and B direction is used to examine as-soldered and thermally cycled joints, respectively.

3.3 RESULTS

Surface Appearance and Microstructure of the As-Soldered Joint

Optical and ESEM micrographs of the surfaces of the as-soldered 95.5Sn/4Ag/0.5Cu solder joints are given in Figure 3.2. There was no observable damage on these surfaces. The solder joint surface consisted of almost pure β-Sn, Ag_3Sn, Cu_6Sn_5 intermetallics, and Pb phase. The β-Sn phase exhibited an elliptical-shape morphology. Ag_3Sn intermetallics existed in needle and disk shapes, and were embedded within the β-Sn phase. Hexagonal shaped Cu_6Sn_5 intermetallics were also prevalent on the surface of the solder joint. Pb phase was found mostly between β-Sn grains at various regions of the solder joint.

The microstructures of a cross-section (indicated in Figure 3.1b) of as-soldered 95.5Sn/4Ag/0.5Cu solder joint are given in Figure 3.3. The solder comprised of pure β-Sn phase matrix with eutectic Sn-Ag phase that is a mixture of β-Sn and small needle shaped Ag_3Sn intermetallics. Pb phase (bright areas) was also identified and its existence was attributed to the Sn/Pb solder tinning used for the lead of the chip component. Few irregular shaped Cu_6Sn_5 intermetallics were also observed. Ag_3Sn intermetallic layer was formed between solder and alumina substrate as a result of reaction between Sn from the solder and Ag from the 99Ag/1Pt metallization as shown in Figure 3.3(b). This Ag also reacted with Sn resulting in the formation of large rod shaped Ag_3Sn intermetallics, which could have broken away from the Ag_3Sn layer and entered into the bulk solder region during reflow.

The microstructure of the regions between solder and Cu component lead is provided in Figure 3.3(c). Sn-Pb layer tinning on the surface of the Cu component lead

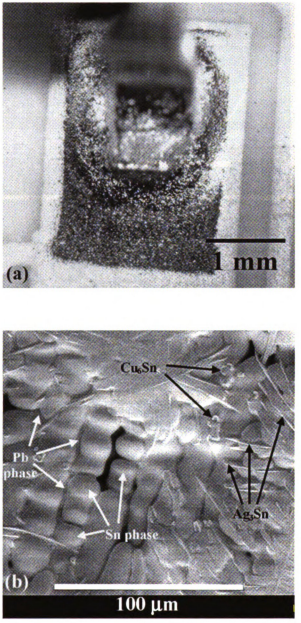

Figure 3.2 (a)Optical and (b)ESEM micrographs of surface appearance of as-soldered 95.5Sn/4Ag/0.5Cu solder joint.

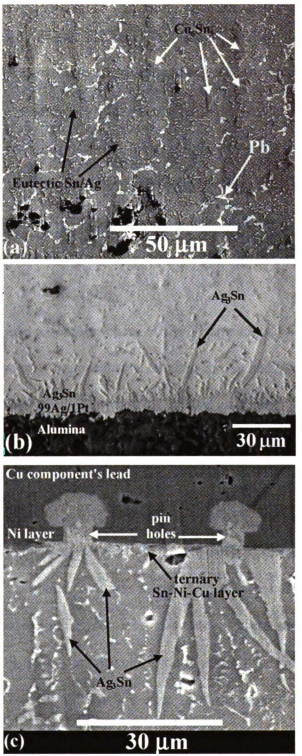

Figure 3.3 ESEM and optical micrographs showing microstructures of a cross-section of as-soldered 95.5Sn/4Ag/0.5Cu solder joint in the direction shown in Figure 3.1b. (a) is the bulk solder region, (b) is the region near Ag_3Sn intermetallic layer, (c) is the region near Ni coating layer on Cu lead.

dissolved in molten solder during reflow resulting in the formation of Pb phase in bulk solder region as shown in Figure 3.3(a). The Ni layer plating on a Cu component lead exhibited discontinuity due to several pin-hole defects. Molten solder penetrated through the pin-hole defect and reacted with the Cu lead resulting in the formation of Cu_3Sn and Cu_6Sn_5 intermetallics inside the hole. Similar damage in the Ni plated leadless chip resistor has been identified in a previous study [111]. Since the Ni protective layer was breached, ternary intermetallic layer consisting of Sn, Ni, and Cu replaced Sn or Sn-Pb layer tinning adjacent to the Ni layer.

Surface Appearance and Microstructure of the Thermally Cycled Joints

Surface appearances of representative eutectic Sn-Ag and 95.5Sn/4Ag/0.5Cu solder joints after 250 and 1000 thermal cycles are shown in Figure 3.4. Thermally cycled solder joints exhibited significant surface cracking that was circumferential to the component lead, irrespective of which of the two solders was used to make the joint. After 250 thermal cycles, the 95.5Sn/4Ag/0.5Cu solder joint showed more surface cracking than the eutectic Sn-Ag solder joint. After 1000 cycles, the surface appearance of the 95.5Sn/4Ag/0.5Cu solder joint was slightly more grainy and rougher compared to the eutectic Sn-Ag solder joint. However, the crack density on the joint surface was apparently the same for both types of solder joints after 1000 cycles. The extent of the opening of the cracks on the joint surface after 1000 thermal cycles was more than that after 250 thermal cycles.

Closer examinations of the representative cracks on the surface of the solder joint shown in Figure 3.4 are presented in Figure 3.5. Figure 3.5(a) shows that the cracking

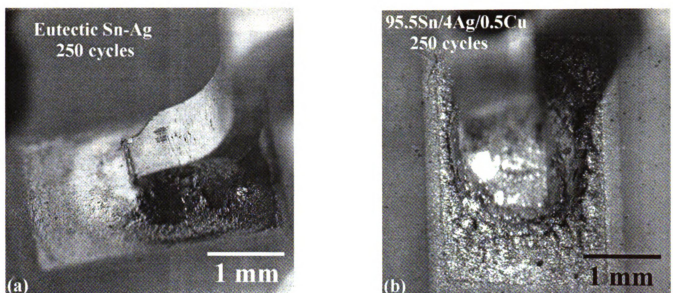

Figure 3.4 (a) & (b) Optical micrographs of surface appearances of representative eutectic Sn-Ag (a) and 95.5Sn/4Ag/0.5Cu (b) solder joint after 250 thermal cycles.

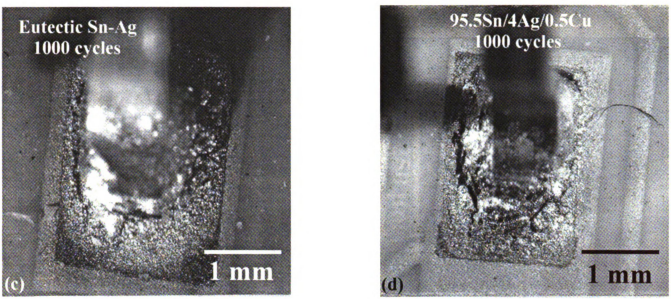

Figure 3.4 (c) & (d) Optical micrographs of surface appearances of representative eutectic Sn-Ag (c) and 95.5Sn/4Ag/0.5Cu (d) solder joint after 1000 thermal cycles.

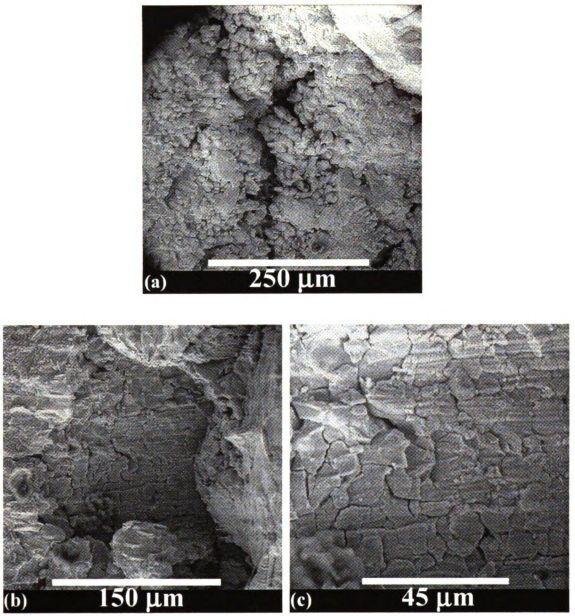

Figure 3.5 ESEM micrographs of circumferential crack on the surface of solder joint. (a) Eutectic Sn-Ag solder joint after 1000 thermal cycles, (b) and (c) 95.5Sn/4Ag/0.5Cu solder joint after 1000 thermal cycles.

occurred between β-Sn grains during thermal cycling. The cracking between β-Sn grains indicates that the microcracks developed between elliptical Sn grains evolved as a macrocrack that is circumferential to the component lead. Figures 3.5(b) and 3.5(c) also show that the cracking along the grain boundaries between β-Sn grains at the bottom surface of the open crack. The bottom surfaces of the open crack revealed striations that were parallel to the direction of the crack opening and closing during thermal cycling as shown in Figures 3.5(b) and 3.5(c). These striations were also found to be perpendicular to the circumferential direction of cracking around the component lead. The schematic drawing given in Figure 3.6 illustrates the direction of striations with respect to the circumferential cracks. These striations were found at the bottom surface at every location of the circumferential crack around the component lead as illustrated in Figure 3.6. These striations are attributed to rubbing of the harder Ag_3Sn particles present at the grain boundaries on the grain surface during opening and closing of the crack.

The microstructures of eutectic Sn-Ag and 95.5Sn/4Ag/0.5Cu solder joint after 250 and 1000 thermal cycles, provided in Figure 3.7, illustrate the coarsening of the Ag_3Sn intermetallics. Small needle shaped Ag_3Sn intermetallics present in as-joined condition (shown in Figure 3.3(a)) have coarsened into more rounded particles and are found to be more uniformly distributed. The details of the microstructural coarsening have been discussed in other previous studies [25,26,92]. The coarsening behavior of the constituent phases was prominent with increased number of thermal cycling. Ag_3Sn layer that formed between the solder and 99Ag/1Pt during reflow also exhibited significant growth during thermal cycling, depending upon the number of cycles as shown in Figure 3.8.

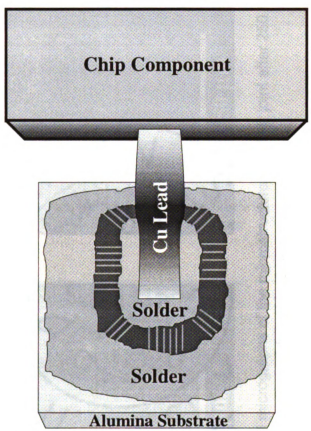

Figure 3.6 A schematic drawing showing the circumferential crack on the free surface of the solder joint and striations on the bottom surface in the open crack.

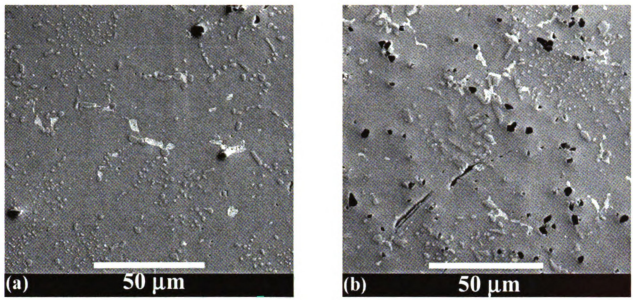

Figure 3.7 (a) & (b) ESEM micrographs of the microstructure of solder joint after 250 thermal cycles. (a) and (b) are eutectic Sn-Ag and 95.5Sn/4Ag/0.5Cu, respectively.

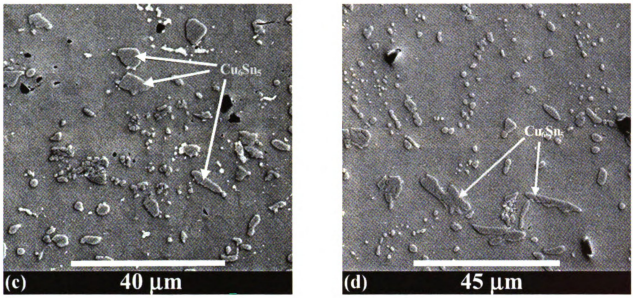

Figure 3.7 (c) & (d) ESEM micrographs of the microstructure of solder joint after 1000 thermal cycles. (c) and (d) are eutectic Sn-Ag and 95.5Sn/4Ag/0.5Cu, respectively.

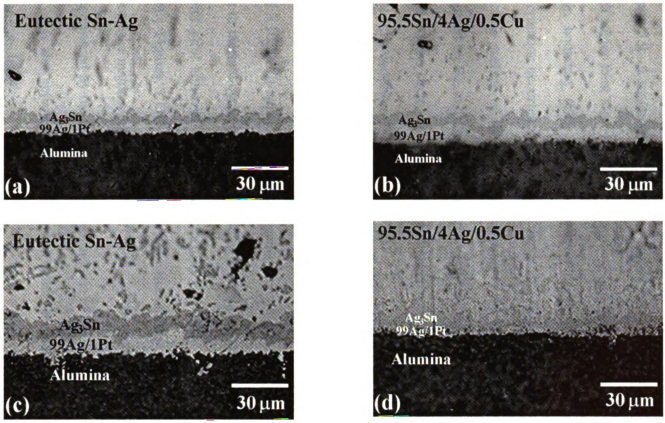

Figure 3.8 ESEM micrographs of Ag_3Sn intermetallic layer
between solder and 99Ag/1Pt metallization on alumina substrate.
(a) and (b) are eutectic Sn-Ag and 95.5Sn/4Ag/0.5Cu after 250 thermal cycles, respectively.
(c) and (d) are eutectic Sn-Ag and 95.5Sn/4Ag/0.5Cu after 1000 thermal cycles, respectively.

Studies on the Cross Section of the Solder Joint That Underwent Thermal Cycling

Microstructure observed in the cross-section (indicated in Figure 3.1(c)) of the eutectic Sn-Ag and 95.5Sn/4Ag/0.5Cu solder joint after 1000 thermal cycles are given in Figure 3.9. A major crack, which can lead to failure of the solder joint, was observed in each solder joint after 1000 thermal cycles. An important microstructural illustration of grain boundary (GB) sliding indicated that during the thermal cycling significant deformation occurred only in few locations. Such features were observed in regions near the free surface of the solder joint (denoted by A), regions around the major crack (denoted by B), and regions around the corner of the Cu lead (denoted by C). However, there was no such a microstructural indication associated with deformation in the solder joints that underwent 250 thermal cycles

The regions near the free surface of the solder joint (denoted by A in Figure 3.9) that exhibited deformed β-Sn grains due to thermal cycling are shown in Figures 3.10(a) and 3.10(b). It appeared that β-Sn grains present in this region experienced GB sliding due to thermal cycling. Such GB sliding was not observed in the interior regions of the solder joint although it was pronounced in regions near the free surface of the solder joint. Figures 3.11(a) and 3.11(b) reveal that similar GB sliding occurred in regions around the major crack (denoted by B in Figure 3.9). This indicates that GB sliding was accompanied by the formation and propagation of the crack along grain boundaries of β-Sn. It is also apparent that the crack propagated through regions in the bulk solder near the Ag_3Sn layer.

Cracks observed in thin regions between the Cu lead and Ag_3Sn intermetallic layer on the metallized substrate of the 95.5Sn/4Ag/0.5Cu solder joint are illustrated with

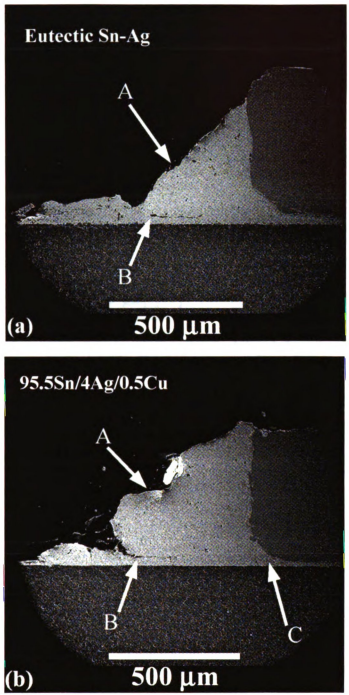

Figure 3.9 ESEM micrographs of cross-section of solder joint after 1000 thermal cycles. (a) is the eutectic Sn-Ag solder joint and (b) is the 95.5Sn/4Ag/0.5Cu solder joint.

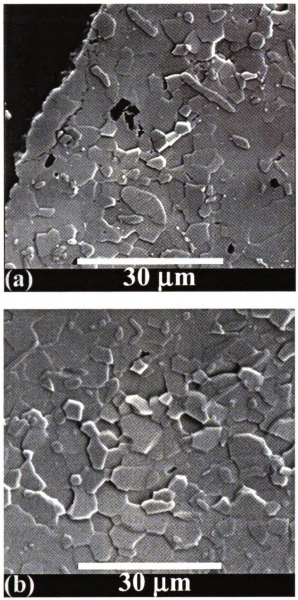

Figure 3.10 ESEM micrographs of a region near free surface of the solder joint after 100 thermal cycles.
(a) is the eutectic Sn-Ag solder joint and
(b) is the 95.5Sn/4Ag/0.5Cu solder joint.

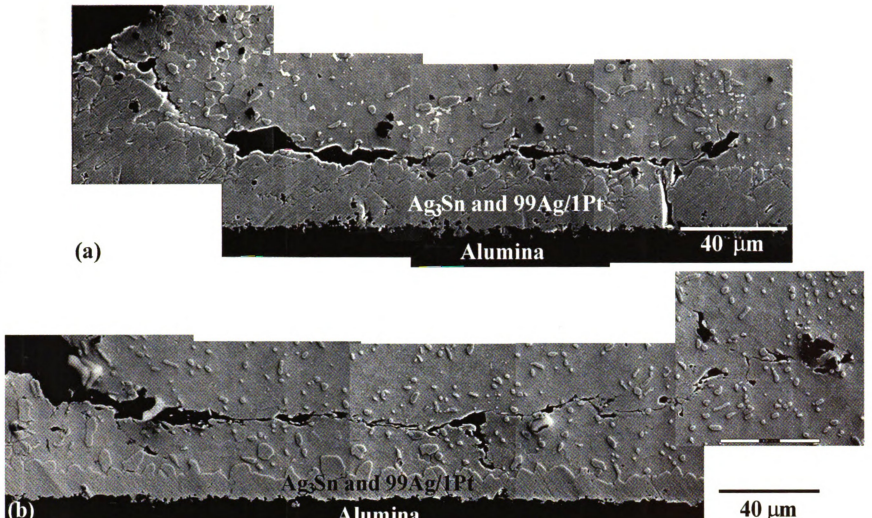

Figure 3.11 ESEM micrographs showing the crack within bulk region of the solder joint after 1000 thermal cycles. (a) is the eutectic Sn-Ag solder joint and (b) is the 95.5Sn/4Ag/0.5Cu solder joint.

micrographs given in Figure 3.12. The cracks propagated along the boundaries between the Ag_3Sn layer and bulk solder. In the region around the corner of Cu lead (marked by C in Figure 3.9(b)), the GB sliding, which was identified in regions near the free surface and around the major crack, was also prevalent. The eutectic Sn-Ag solder joint, however, did not reveal any feature of deformation such as GB sliding and crack in the same region (around the corner of the Cu lead).

Re-Examination of the Cross Section of the Solder Joint

The re-examination of the cross-section with ESEM of the solder joints shown in Figure 3.9 were performed without any additional treatments after 10 months since the first examination was carried out. Figure 3.13 compares the microstructures seen in the first and the second examination of the interior region away from the free surface, and the region near Ag_3Sn intermetallic layer, in the cross-section of the eutectic Sn-Ag solder joint. The microstructural characteristics of GB sliding were observed in both regions during the second examination where no microstructural evidence of GB sliding was found in the first examination. It is obvious that the cross-section of the solder joint underwent further GB sliding during storage in regions where no microstructural characteristics could be observed in the first examination. The regions beneath the Cu lead in the eutectic Sn-Ag solder joint that did not exhibit cracking during the first examination; however, the same region exhibited cracking during the second examination as shown in Figure 3.14. The crack propagation was along the grain boundaries of β-Sn in the region around the corner of the Cu lead where the GB sliding was prominent. The crack path changed to the interface between Ag_3Sn intermetallic layer and the solder in

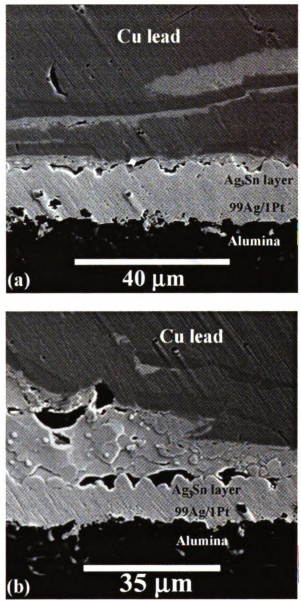

Figure 3.12 ESEM micrographs of (a) crack in the thin region between Cu lead and 99Ag/1Pt metallized alumina substrate and (b) microstructure in the region around the corner of Cu lead.

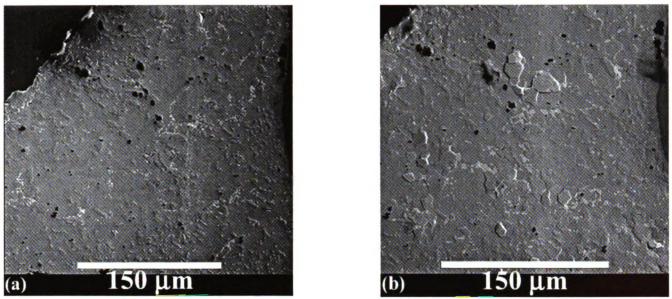

Figure 3.13 (a) & (b) ESEM micrographs of microstructures of two same regions of the eutectic Sn-Ag solder joint in first and second examination. (a) and (b) represent the interior region away from the free surface in first and second examination, respectively.

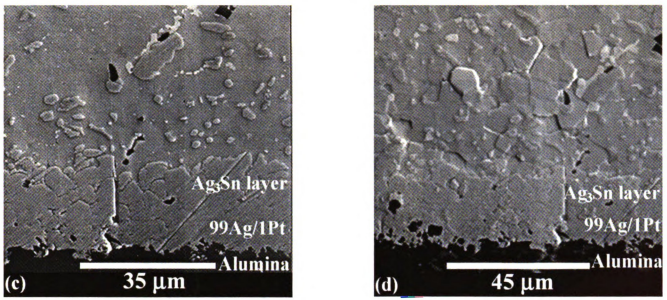

Figure 3.13 (c) & (d) ESEM micrographs of microstructures of two same regions of the eutectic Sn-Ag solder joint in first and second examination. (c) and (d) represent the region near Ag_3Sn intermetallic layer, respectively.

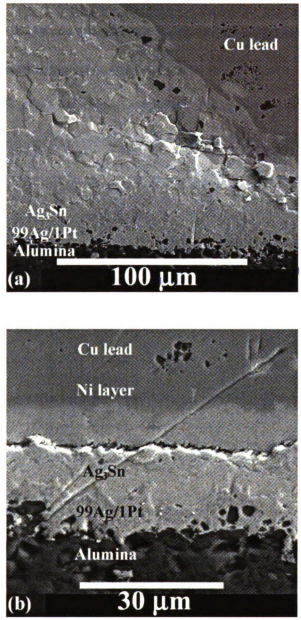

Figure 3.14 ESEM micrographs of microstructures of regions beneath Cu lead of the eutectic Sn-Ag solder joint. (a) is the region around the corner of the Cu lead and (b) is the region beneath Cu lead.

the regions beneath the Cu lead. In this region only small amount of solder is present compared to that around the corner of Cu lead. Unfortunately, microstructural features in the 95.5Sn/4Ag/0.5Cu solder joint could not be observed in the second examination due to severe contamination of the specimens during storage.

As-soldered joints also exhibited the microstructural characteristics of GB sliding in regions near Ag_3Sn intermetallic layer as Figure 3.15 reveals. However, the extent of GB sliding in the as-soldered joints during storage appeared to be much less compared to the solder joints subjected to 1000 thermal cycles.

3.4 DISCUSSION

The present microstructural study dealt with deformation and fracture aspects in two Sn-Ag based solders during thermomechanical cycling of an actual electronic component. This section addresses the implications of the findings and possible reasons for the same.

Effects of Pb Contamination

There have been concerns about the effects of tinning of Cu leads with Pb containing solders [17,126,127]. Pb entering the Sn-Ag solder results in affecting its higher temperature capabilities, due to the formation of low melting ternary eutectic phase of 178°C [128]. During the course of this study we did observe the presence of Pb containing phases within the solder, distributed throughout the joint. However, if such phases were to affect the thermomechanical fatigue behavior of the solders studied, the region where the detrimental crack could form and grow should be along the regions

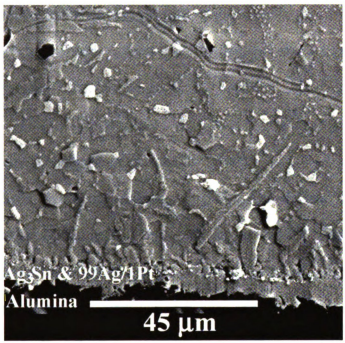

Figure 3.15 ESEM micrograph of a region near Ag_3Sn intermetallic in as-soldered 95Sn/4Ag/0.5Cu solder joint in the second examination.

where the Pb contamination should be a maximum. Contrary to this expectation the detrimental crack formed near the ceramic substrate where the effects due to mismatch in CTE will be a maximum. However it should be emphasized that the highest temperature experienced by the solder joints in this study was only 125°C, reasonably below the melting temperatures of low melting Pb-containing phases (178°C) that will be present in the contaminated solder. If higher temperatures are involved in the thermal cycling, so as to evaluate the higher temperature capabilities of the solders studied, problems due to Pb contamination may arise.

Effects of Breached Ni Coating on Cu Lead

There have been significant concerns regarding the defects in the Ni coating, especially the electroless coating, on the copper substrate [129-131]. Similar defects were found in Ni coating on leadless chip resistor [111]. Defects such as pinholes present in such a layer can facilitate the diffusion of copper and tin, and promote formation of intermetallics that can affect the integrity of the joint. During the course of this study formation of such intermetallics, especially mushroom-type growth within the Ni coating and the Cu lead, have been observed. If these were potential sources for thermomechanical fatigue failures, the detrimental crack that affects the integrity of the joint should be in the region near the copper lead. However, this was not the case for the temperature range and holding times used during thermal cycling in this study. Obviously the CTE mismatch seems to be more of a contributing factor for the failure in the component studied, rather than breached Ni coating. However, a breached Ni coating

on the substrate may significantly affect the thermomechanical fatigue behavior of the solder joint.

Effects of Small Amount of Copper Addition to Sn-Ag Solder

During the course of this study no significant differences in thermomechanical fatigue behavior due to the small addition Cu to Sn-Ag solder could be detected. Such an observation tends to indicate that the breached Ni-coating on the copper lead, or other means of impregnating the solder with small amounts of Cu will overshadow the effects of small additions of Cu to Sn-Ag solder. However, it should be noted that the small decrease in ternary eutectic temperature to 216.8°C [107] due to the addition of Cu to the Sn-Ag solder still results in a melting temperature well above the highest temperature used for thermal cycling of this study.

Thermomechanical Fatigue Crack Nucleation

In all the samples observed it was apparent that the thermomechanical crack nucleation always started on the free surface. There have been studies indicating that stress imposed decreases and strain imposed increases during thermomechanical fatigue [75,123] Some other studies indicate that stress-strain hysteresis loop during thermal cycling stabilizes after a few cycles [110]. In stress relaxation studies on single shear lap specimens made with the eutectic Sn-Ag solder joints having similar joint thickness, the stress relaxation after about an hour at room temperature was about 50% and that at 150°C was about 60%, for comparable imposed strains [132]. All these observations are

based on specific joint geometry and joint thickness. Such observations elucidate the role of constraints on stress relaxation.

Unlike in controlled studies that use single shear-lap specimens or joint specimens with controlled geometry, the free surface area of the solder joint to the interface area between solder and substrate/component is much higher in the solder joints studied. As a consequence, the strain accumulated due to thermomechanical fatigue could dissipate from regions of high strain concentration to the free surface. This is more probable based on hot-deformation condition that exists in solders due to the high homologous temperatures experienced by the solders. Such strain dissipation at the free surface could create surface undulations that provide potential sites for crack opening. This dissipation of strain/stress appears to be accommodated by grain boundary sliding. Although such crack nucleation could occur any where on the free surface of the solder, presence of the copper lead, with its own CTE, seems to favor the circumferential surface cracking observed during the course of this study. However, these circumferential cracks did not prove to be detrimental due to the soft interior of the bulk solder joint that was able to accommodate the strain gradients by plastic deformation, and deter the crack propagation.

The location of the detrimental crack tends to indicate that the region that experiences the maximum effects of CTE mismatch is the potential location for it. Although studies based on Pb-Sn solders indicate that localized phase coarsening in such a region contribute to the thermomechanical fatigue failure [113,114,73], no significant coarsening of grains in such regions was observed in Sn-Ag solders used in this study. However, such an observation does not preclude the possibility of dynamic

recovery/recrystallization in such a region. Such microstructural rearrangement will also facilitate stress relaxation. The important finding is that there is no grain coarsening/growth in these regions. Grain sizes in these regions are about the same as that in the as-made joint.

Thermomechanical Fatigue Growth of the Catastrophic Crack

The catastrophic crack that contributes to the thermomechanical fatigue failure was found to nucleate on the free surface near the interface between solder and intermetallic layer on the metallized ceramic substrate. This crack propagated by grain boundary decohesion/sliding within the solder in a region adjacent to this interface. This crack did not reach the solder/intermetallic interface within the bulk of the solder joint. If and when the intermetallic region grew due to aging, this crack tended to reach this interface. Such a feature can be realized in the very thin region underneath the copper lead where the amount of leftover solder was very little. This observation tends to indicate that grain boundary sliding within the solder to be dominant mechanism of thermomechanical fatigue failure in the Sn-Ag solder used in the electronic component studied.

Residual Stresses due to Thermomechanical Fatigue

Another important finding of this study is the existence of significant amount of residual stress due to thermomechanical fatigue. Such an effect became obvious by the enhanced relief effects revealing grain structures noted in specimens re-examined after about ten months following the initial examination, with no additional specimen preparation. The residual stresses that exist in thermomechanically fatigued samples are

much higher than those present in as-joined samples, as evidenced by the much enhanced surface relief in the former compared to a bare minimal one in the latter.

3.5 SUMMARY

Following summarizes the findings based on studies with actual electronic components containing metallized ceramic substrate and tinned copper leads soldered with Sn-Ag or 95.5Sn/4Ag/0.5Cu solder:

1. Thermomechanical fatigue damage in Sn-Ag and 95.5Sn/4Ag/0.5Cu solder joints occurs by processes that are different from those observed in Pb-Sn solders. There appears to be no grain coarsening in Sn-Ag solders as a consequence of thermal cycling.
2. Cracks formed due to thermal cycling in Sn-Ag and 95.5Sn/4Ag/0.5Cu solder joints initiate on the free surface of the solder joint and progress towards the interior regions of the joint.
3. Crack growth due to thermomechanical fatigue is along the grain boundaries of β-Sn phase. Opening and closing of these cracks during each thermal cycle results in striations on the grain boundary surfaces that intersect the opening crack. These striations can be due to the rubbing of Ag_3Sn particles present at the grain boundaries onto the grain boundary surfaces.
4. The crack that will contribute to the ultimate thermomechanical fatigue failure of the joint occurs very near the ceramic substrate, initiating at the free surface of the solder joint and progressing inwards and continuing along the solder region near the interface with Ag_3Sn intermetallic layer formed with metallized ceramic substrate.

5. Significant amount of residual stresses resulting from thermomechanical fatigue can cause further damage to solder joints during storage at room temperature.

6. Presence of small amounts of copper does not significantly affect the thermomechanical fatigue behavior of the Sn-Ag solder joints.

7. Presence of Pb phase in the solder, arising from tinning of Cu lead, also does not appear to affect the thermomechanical fatigue behavior of the Sn-Ag solder joints as long as the maximum temperature experienced is below 150°C.

CHAPTER 4

CHARACTERIZATION OF THE GROWTH OF INTERMETALLIC INTERFACIAL LAYERS OF Sn-Ag AND Sn-Pb EUTECTIC SOLDERS AND THEIR COMPOSITE SOLDERS ON Cu SUBSTRATE DURING ISOTHERMAL LONG-TERM AGING

ABSTRACT

Single shear lap joints were made with four different solders, Sn-Pb and Sn-Ag eutectic solders, and their composites containing about 20 vol% *in-situ* Cu_6Sn_5 intermetallic phases about 3-8 micrometers in diameter. Two sets of experiments were performed : In the first set, all of the above four solder joints were aged at 150°C for periods ranging to 5000 hours and the intermetallic growth was monitored periodically. In the second set, each of the above four solder joints was aged at five different temperatures for 4000 hours. The interfacial layers between solders and the Cu substrate were examined using optical and scanning electron microscopy. The growth kinetics of intermetallic interfacial layers formed between solder and Cu substrate was characterized. The effect of *in-situ* Cu_6Sn_5 intermetallic phases on the growth rate is discussed. The growth rate of the intermetallic layers in the eutectic Sn-Pb composite was slower for the first 150 hours as compared to the eutectic Sn-Pb non-composite. The growth rate of the intermetallic layers was similar for both the eutectic Sn-Ag and eutectic Sn-Ag composite throughout the aging duration. The activation energies for Cu_6Sn_5 layer growth for the eutectic Sn-Pb and Sn-Ag solder joints are evaluated to be 111 kJ/mol and 116 kJ/mol, respectively. The eutectic Sn-Pb and Sn-Ag composite solder joints exhibit higher activation energies of 161 kJ/mol and 203 kJ/mol.

4.1 INTRODUCTION

Eutectic Sn-Pb solder has been widely used in electronic industry as an interconnect material between electronic components and printed circuit boards. Recently, the environmental and mechanical concerns have warranted the electronic industry to develop alternatives to Pb-free solders [26]. Eutectic Sn-Ag solder is being considered as a possible Pb-free solder substitute for several reasons. The eutectic Sn-Ag solder is non-toxic, has a higher melting temperature of 221°C, is suitable for higher temperature applications, and offers better mechanical properties [2,5]. Its wetting characteristics are comparable to that of eutectic Sn-Pb solder [4].

The Sn-Pb and Sn-Ag solders bond strongly with Cu substrate by forming intermetallic layers between the solder and Cu substrate. Two intermetallic layers, namely, Cu_6Sn_5 (η-phase) and Cu_3Sn (ε-phase), are produced at the interface between the solder and Cu substrate. However, these layers tend to grow with time by solid state diffusion even at ambient temperatures. These intermetallic layers may adversely affect the reliability and solderability of solder joints due to excessive growth during storage and service. They can be sources of mechanical weakness in solder joints due to the brittle nature of the intermetallics or can cause delamination at the interface [133,82].

Because of the importance of the intermetallic layer to bonding, and its influence on the mechanical properties of solder joints, many studies have been carried out on the crystal structures [134] on the growth kinetics [135-137,90,16,91], and on their effects on mechanical properties [83,138-140] While over the last few years the kinetics and microstructural data published [82,137,90,16,91] on the intermetallic layers in the Pb-free

solder and composite solder joints have been considerable, a basic understanding is far from complete.

This study investigates microstructural evolution and growth kinetics of the Cu_6Sn_5 and Cu_3Sn intermetallic layers in the eutectic Sn-Pb and Sn-Ag solder, and their corresponding composite solder joints during long-term solid state aging. The growth kinetics of intermetallic interfacial layers formed between solders and Cu substrate was measured as a function of time and temperature, and activation energies for the intermetallic layer growth were calculated using a diffusion-controlled growth model.

4.2 EXPERIMENTAL PROCEDURES

Single shear lap solder joints were fabricated by soldering two dog-bone shaped Cu strips together using the solder preforms of four different solders, eutectic Sn-Pb and eutectic Sn-Ag solders, and their corresponding composite solders with 20 vol% Cu_6Sn_5 reinforcements. Eutectic Sn-Pb and Sn-Ag solders were provided in the form of cast ingots by Alpha Metals. Composite solders were prepared by introducing about 20 vol% Cu_6Sn_5 intermetallic particles into the eutectic Sn-Pb and Sn-Ag solders by *in-situ* methods. These solders were rolled to produce sheets about 100 μm thick, and cut into the preform foils of about 1.0 mm^2 size.

Copper substrates were machined from 0.5 mm-thick Cu sheet using electrodischarge machining (EDM) to produce specimens 11.5 mm long with a gage width of 1 mm. The Cu substrates were painted at the end of the gage section of the substrate with a solder mask and baked for about 1 hour at 150°C to confine the molten solder within a 1 mm^2 area during joining operation. The Cu substrates were precleaned

with a 50% aqueous HNO_3 solution and rinsed in methyl alcohol just prior to soldering to remove the thin tarnish layers.

Figure 4.1 schematically illustrates fabrication of solder joints along with dimensions of Cu substrate. Solder joints were fabricated in an aluminum fixture designed to hold the assemblies of solder joints in proper alignment during soldering operation. Liquid acid flux (α200-L) was applied to the area to be soldered in each Cu substrates prior to sandwiching the solder preforms between them. They were placed on an aluminum fixture. The temperatures of solder joints during joining operation were monitored by a thermocouple attached to the aluminum fixture. Since aluminum has very high thermal conductivity, it was assumed that the temperature of the aluminum fixture was nearly the same as that of the solder joints. The aluminum fixture with an assembly of 10 solder joints was placed on a preheated hot plate maintained at about 500°C, and allowed to reach about 230°C for eutectic Sn-Pb and its composite solder joints, and 270°C for eutectic Sn-Ag and its composite solder joints. When the solder joints reached the temperature allowed, the aluminum fixture was moved to a cooling surface. Figure 4.2 illustrates geometry and dimensions of fabricated single shear lap solder joints. The solder joints possess about $1mm^2$ joining area and about 100 μm thickness. During soldering, the intermetallic particulate reinforcements in composite solders remained in a solid state during reflow because of their higher melting temperature, while the solder matrices in them were reflowed and solidified during soldering process.

Excess solder present on both sides of the joints were ground off, and one of its sides was polished using 400 and 2000 grit sand papers followed by a finish using 0.05 μm SiO_2 colloidal suspension. The solder joints were etched with a solution of 40%

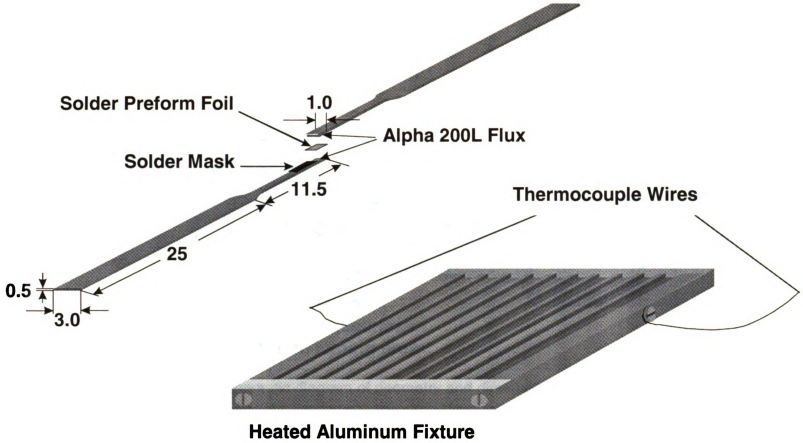

Figure 4.1 Schematic diagram of the assembly of solder joints and aluminum fixture to hold solder joints (scales in mm).

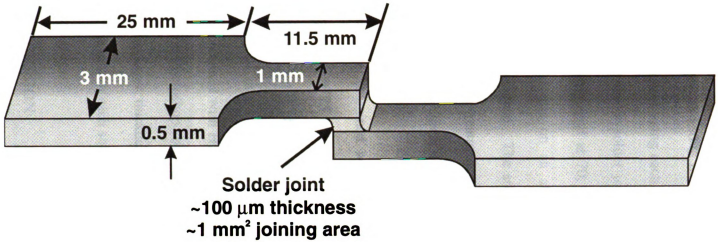

Figure 4.2 Schematic diagram of geometry and dimensions of solder joints.

H_2O/40% NH_4OH/20%H_2O_2 for about 10 seconds to reveal microstructural features.

Two sets of aging treatments were performed. In the first set, the joints made with all of the four solders were aged at 150°C for various periods of time ranging to 5000 hours. The second set consisted of aging each of the four solder joints at five different temperatures for 4000 hours. Sn-Pb solder joints were aged at 50, 70, 100, 120 and 150°C, Sn-Ag solder joints were aged at 70, 100, 120, 150 and 180°C. Aging was conducted by placing solder joints on an aluminum plate maintained at a steady temperature by means of a hot plate. The solder joints were slightly repolished and etched periodically after each aging treatment to reveal the resultant microstructure. This procedure helped to monitor the progress of the aging process on the same specimen at various stages.

The solder joints were examined with an optical microscope and a scanning electron microscope operated at 25 kV. Energy dispersive X-ray spectra (EDS) were used to identify elements present in phases and intermetallic layers. Optical micrographs of solder/substrate interfacial intermetallic layers were used to measure its thickness. These micrographs were scanned with HG Scanet 3C scanner and scanned images were then analyzed using Adobe Photoshop software to measure the thickness of intermetallic layers. The intermetallic layer thicknesses reported here are averages of about 10 measurements per micrograph for each solder joint.

4.3 RESULTS AND DISCUSSION

As-joined microstructures of the eutectic Sn-Pb and Sn-Ag solder, and their composite solder joints are presented in Figure 4.3. The Sn-Pb solder joint consisted of

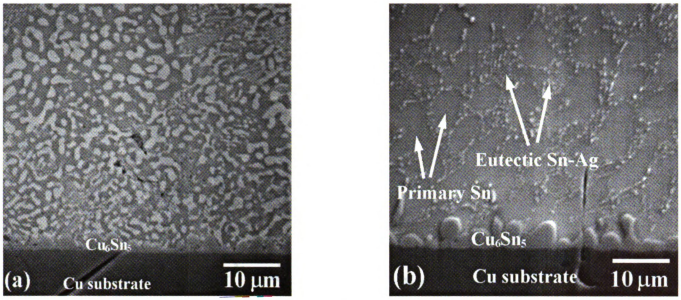

Figure 4.3 (a) & (b) SEM micrographs showing the microstructure of as-fabricated solder joints (a) eutectic Sn-Pb solder joint and (b) eutectic Sn-Ag solder joint.

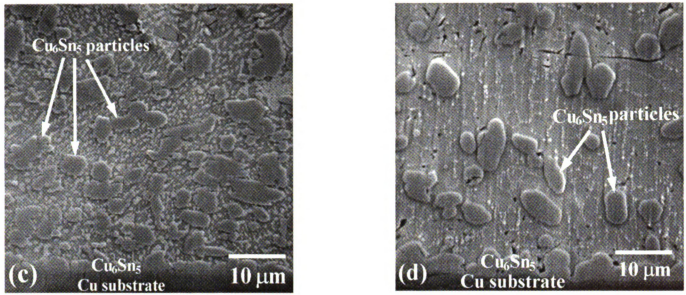

Figure 4.3 (c) & (d) SEM micrographs showing the microstructure of as-fabricated solder joints. (c) eutectic Sn-Pb composite solder joint and (d) eutectic Sn-Ag composite solder joint.

three regions namely, the Cu substrate, the Cu_6Sn_5 intermetallic layer, and the eutectic Sn-Pb phase. Sn-Ag solder joint revealed four distinct regions, the Cu substrate, the Cu_6Sn_5 intermetallic layer, primary Sn-rich phase and the eutectic Sn-Ag phase. The composite solder joints possessed microstructures similar to their corresponding non-composites except for the uniformly distributed 3 ~ 8 μm size intentionally incorporated Cu_6Sn_5 intermetallic particles. Prior to aging only the Cu_6Sn_5 intermetallic layer at the solder/substrate interface was observed for all four solder joints.

Figure 4.4 reveals the microstructures of all the four solder joints after aging for 5000 hours at 150°C. The aged eutectic Sn-Pb solder joint consists of the Cu substrate, the Cu_3Sn intermetallic layer, the Cu_6Sn_5 intermetallic layer, the Pb-rich (white) phase, and the Sn rich (dark) phase. The Pb-rich and Sn-rich phases exhibit extensive coarsening due to aging. The growth of the intermetallic layers depleted the Sn-rich phases adjacent to the Cu_6Sn_5 intermetallic layer and led to the formation of a layer of Pb-rich phase across the entire intermetallic layer/solder interface. Such a feature has been observed in other studies [133,82,90].

The aged eutectic Sn-Ag solder joint comprises the Cu substrate, the Cu_3Sn intermetallic layer, the Cu_6Sn_5 intermetallic layer, the Ag_3Sn particles embedded within the Cu_6Sn_5 intermetallic layer, the Ag_3Sn particles in the solder, and the Sn-rich phase. The Ag_3Sn particles present in the solder and the Cu_6Sn_5 intermetallic layer exhibited a significant amount of coarsening due to aging. With increased aging, the Ag_3Sn particles became more prevalent in the Cu_6Sn_5 intermetallic layer. This observation is consistent with a previous study [91] on the intermetallic growth in a eutectic Sn-Ag/Cu diffusion couple. The existence of Ag_3Sn particles within the Cu_6Sn_5 intermetallic layer is related

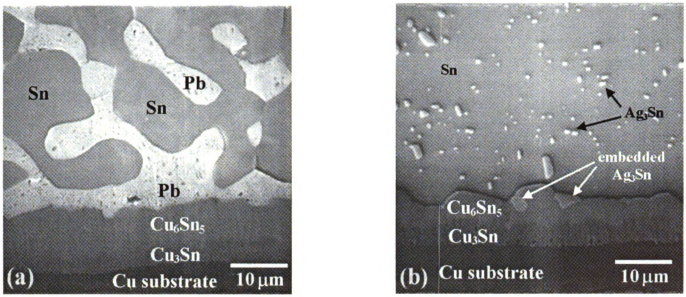

Figure 4.4 (a) & (b) SEM micrographs showing the microstructure of the solder joints after aging at 150°C for 5000 hours. (a) eutectic Sn-Pb solder joint and (b) eutectic Sn-Ag solder joint.

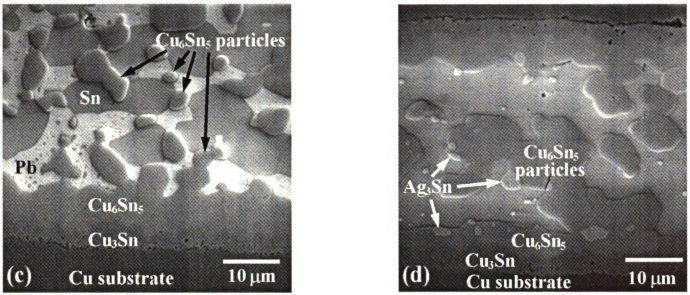

Figure 4.4 (c) & (d) SEM micrographs showing the microstructure of the solder joints after aging at 150°C for 5000 hours. (c) eutectic Sn-Pb composite solder joint, (d) eutectic Sn-Ag composite solder joint.

to the depletion of Sn close to intermetallic layer.

Composite solder joints retained characteristics similar to corresponding non-composite solder joints with the presence of the Cu_3Sn intermetallic layer, the Cu_6Sn_5 intermetallic layer, coarsened Pb-rich and Sn-rich solder phases, and Ag_3Sn particles. The Cu_6Sn_5 particles present in the composite solder joints also showed coarsening after long-term aging of 5000 hours. In addition, the Cu_6Sn_5 particles present in the region near the intermetallic layer tended to attach with the Cu_6Sn_5 intermetallic layer as shown in Figure 4.4 (c) and (d), resulting in "abnormal" growth of such layers. This undesirable feature is less pronounced in the Sn-Pb composite solder joint than in the Sn-Ag composite solder joint because of the Pb phase present in the Sn-Pb solder. Since this phenomenon is not the direct cause for the intermetallic layer growth, it was not included in the quantitative analysis of the layer growth measurement. It has been observed in a 35 μm thick Sn-Ag composite solder joint that the joining of the Cu_6Sn_5 particles with the Cu_6Sn_5 intermetallic layer led an excessive intermetallic layer growth and finally caused two Cu_6Sn_5 intermetallic layers at opposing sides to bridge together.

Table 4.1 lists the thicknesses of the Cu_6Sn_5 and Cu_3Sn, intermetallic layers for all four solder joints for the aging times up to 5000 hours at 150°C. Presence of these two intermetallic layers was common to all of four solder joints aged in a solid state. The thicknesses of both intermetallic layers increased with time for all four solder joints, and in general the thickness of the Cu_6Sn_5 intermetallic layer was always larger than that of Cu_3Sn layer.

The Cu_3Sn intermetallic layer was not observed for short aging times for all of four solder joints and only Cu_6Sn_5 intermetallic layer was observed. A Transmission Electron

Table 4.1 Intermetallic thicknesses (μm) during aging at 150°C.

Solder Joint/Time (hours)		0	10	50	150	350	700	1200	2200	5000
Eutectic Sn-Pb Solder Joint	Cu_6Sn_5	1.85	2.3	2.8	3.8	4.67	5.15	6.5	7.0	7.8
	Cu_3Sn			2.4	2.6	3.0	3.5	3.9	3.5	4.8
Eutectic Sn-Pb Composite Solder Joint	Cu_6Sn_5	1.9	1.35	1.6	2.9	3.9	5.7	6.9	6.8	8.0
	Cu_3Sn		0.99	1.0	2.35	2.7	2.6	3.3	3.6	4.9
Eutectic Sn-Ag Solder Joint	Cu_6Sn_5	3.5	3.8	4.3	3.8	4.2	4.8	6.4	7.3	6.5
	Cu_3Sn				1.3	2.1	2.5	3.1	4.0	5.6
Eutectic Sn-Ag Composite Solder Joint	Cu_6Sn_5	2.3	2.33	2.62	2.5	2.75	3.0	3.7	5.5	5.5
	Cu_3Sn				1.2	1.9	2.1	2.6	4.0	4.6

Microscopic study by Y. Wu *et al.* [90] reported the presence of about 0.2 ~ 0.3 μm thickness Cu_3Sn layer in an as-fabricated eutectic Sn-Pb solder/Cu joint. Since the solder joints in the current study were investigated by the optical and SEM microscopy, it should be noted that formation of such a thin Cu_3Sn layer during soldering could not be observed.

Sn-Ag and its composite solders formed thicker Cu_6Sn_5 intermetallic layer than the Sn-Pb and its composite solder as a result of the joining operation. Presence of higher amount of Sn present in eutectic Sn-Ag solder (96.5Sn wt%) composition appears to promote a thicker Cu_6Sn_5 intermetallic layer as compared to the eutectic Sn-Pb solder (63Sn wt%). The eutectic Sn-Pb composite solder produced a Cu_6Sn_5 intermetallic layer of comparable thickness to that of the eutectic Sn-Pb non-composite. On the other hand, the eutectic Sn-Ag composite solder formed a less thick Cu_6Sn_5 intermetallic layer than the eutectic Sn-Ag solder due to joining operation. It is not clear how the presence of the Cu_6Sn_5 particles in the solder affects the intermetallic layer formation during with Sn-Ag solder.

Figure 4.5 shows plots of the total intermetallic layer (Cu_6Sn_5 + Cu_3Sn) thickness versus aging times up to 5000 hours using the data in Table 4.1. For clarity, the same plot is shown in three different aging time scales, namely two expanded short time scales and an overall time scale incorporating all aging times investigated.

During the initial stages of aging up to 50 hours, the eutectic Sn-Pb solder joint showed faster growth of the intermetallic layers than did its composite solder joint, and the growth of the intermetallic layers slowed after 50 hours. As shown in Table 4.1, the eutectic Sn-Pb solder joint exhibited no visible Cu_3Sn intermetallic layer growth up to 10

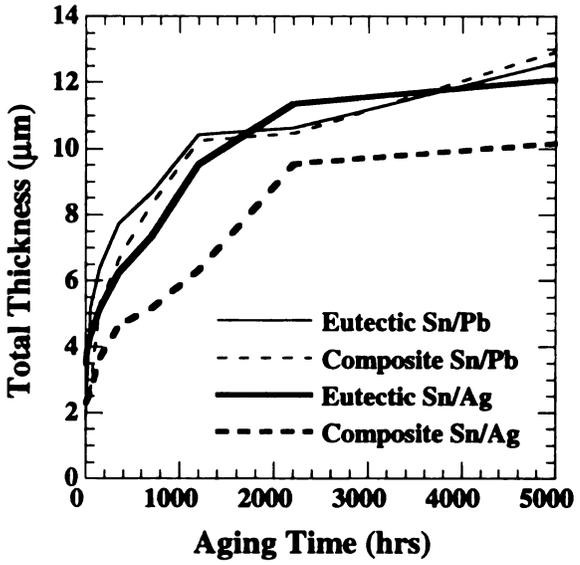

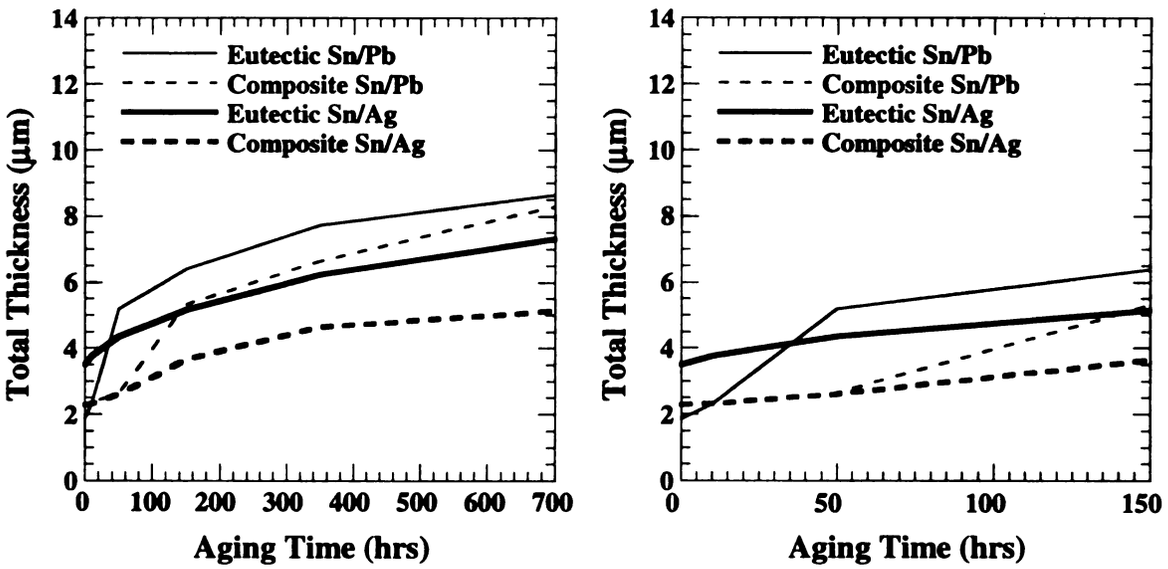

Figure 4.5 Total intermetallic layer (Cu_6Sn_5 + Cu_3Sn) versus aging time for the eutectic Sn-Pb and Sn-Ag solder joints, and their corresponding composite solder joints after aging at 150°C for 5000 hours.

hours. The Cu_3Sn intermetallic layer was observed after 50 hours of aging. After the formation of Cu_3Sn layer, both Cu_6Sn_5 and Cu_3Sn intermetallic layers grew in a progressive manner. These observations for the intermetallic layers in the eutectic Sn-Pb solder joint imply that the Pb-rich phases began to accumulate between solder/Cu_6Sn_5 intermetallic layer interface due to the depletion of Sn-rich phases. They consequently affected the growth of the intermetallic layers by reducing the Sn concentration at the Cu_6Sn_5 intermetallic layer/Cu interface, resulting in the formation of the Cu-rich Cu_3Sn intermetallic layer. The enriched Pb-rich phases adjacent to the Cu_6Sn_5 intermetallic layer, once formed, appears to significantly affect the growth of the intermetallic layers throughout the rest of the aging process.

Sn-Pb composite solder joint exhibited no significant growth of the intermetallic layers initially and after 50 hours, the intermetallic layer growth in this solder showed faster growth than corresponding non-composite solder that finally decelerates after 150 hours as shown in Figure 4.5. After 700 hours, the eutectic Sn-Pb composite solder joint showed growth of the intermetallic layers similar to its non-composite counterpart. The Cu_3Sn intermetallic layer in the eutectic Sn-Pb composite solder joint was noticed even after 10 hours aging, a time period shorter than in its non-composite counterpart, and occupied a considerable portion of the total intermetallic layer.

Since the accumulation of the Pb-rich phases in the eutectic Sn-Pb composite solder joint was not significant prior to an aging period of 50 hours, it appears that the Cu_6Sn_5 particles affected the intermetallic layer growth by delaying Sn diffusion toward the Cu_6Sn_5 intermetallic layer, resulting in the earlier formation of the Cu_3Sn intermetallic layer of similar total thickness up to 50 hours. The Sn depletion at Cu_6Sn_5 intermetallic

layer/solder interface occurred after 50 hours causing the accumulation of the Pb-rich phases. The intermetallic layer growth appears to be affected by the accumulated Pb-rich phase throughout the rest of the aging process beyond 150 hours.

Accumulation of the Pb-rich phases adjacent to the Cu_6Sn_5 intermetallic layer in the eutectic Sn-Pb and its composite solder joints after 350 hour aging at 150°C can be observed in Figure 4.6. It is evident that the Cu_6Sn_5 intermetallic layer in the eutectic Sn-Pb solder joint was completely covered with Pb-rich phase. However, in Sn-Pb composite solder joint only about 87 % of the interface layer was covered with the Pb-rich phase. The comparable enrichment of the Pb-rich phases after aging for 350 hours and the similar growth rate of the intermetallic layers after 700 hours in the eutectic Sn-Pb and its composite solder joints suggest that the growth of the intermetallic layers in the eutectic Sn-Pb composite solder joint was moderated by the enhanced concentrations of Pb-rich phases rather than the Cu_6Sn_5 particles for most of the later stage of aging. The Cu_6Sn_5 particles were effective in retarding the intermetallic layer growth during the initial stages of aging in this solder.

It was considered as a possible mechanism in a previous study [137] that the Cu_6Sn_5 particles can act as Sn sinks so that they reduce the amount of Sn available for the reaction at the substrate/solder interface. However, since the Cu_6Sn_5 particles do not react with the solder and can be considered as an inert phase with respect to the solder, it is unlikely that the Cu_6Sn_5 particles can be sinks for Sn. One possible mechanism is that the Cu_6Sn_5 particles act as partial obstacles to Sn diffusion toward the substrate/solder interface resulting in an increase of its total diffusion distance and delay the Sn supply required for the intermetallic growth. A similar suggestion on the role of the Cu_6Sn_5

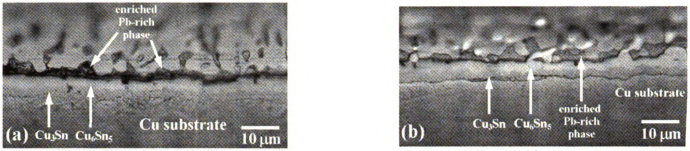

Figure 4.6 Optical micrographs showing the accumulation of the Pb-rich phases adjacent to the Cu_6Sn_5 intermetallic layer in (a) the eutectic Sn-Pb solder joint and (b) the eutectic Sn-Pb composite solder joint aged at 150°C for 350 hours.

particles has been made in a previous study [90].

The eutectic Sn-Ag and its composite solder joints revealed similar growth rates throughout aging. The difference of the intermetallic layer thickness produced during soldering between the eutectic Sn-Ag solder joint and its composite solder joint was maintained for the entire duration of this aging study as shown in Figure 4.5. It can be seen from Table 4.1 that the Cu_3Sn layer in the eutectic Sn-Ag and its composite solder joints exhibited similar thickness values and only the Cu_6Sn_5 layer retained the initial difference of the intermetallic layer thickness portion in the total thickness of the intermetallic layer during aging, resulting in a similar growth rate. This maintenance of the difference in the initial thickness of the intermetallic layers by the Cu_6Sn_5 intermetallic layer indicates that there is no substantial effect of the Cu_6Sn_5 particles on the intermetallic layer growth, although it affects the formation of this layer during joining.

An interesting feature about Cu_3Sn intermetallic layer formation in Sn-Ag solder joint occurs far later than in Sn-Pb solder joint as shown in Table 4.1. This suggests that lack of diffusion of tin from the solder is a dominant factor in determining the rate of growth of the Cu_3Sn layer. Since Sn-Ag solder can provide more tin than Sn-Pb solder matrix, tin deficiency that will occur at Cu_6Sn_5 intermetallic layer/Cu interface with Sn-Pb solder results in early formation of Cu_3Sn layer (in the time range of 0-50 hours as compared to 50-150 hours).

The four solder joints investigated in this study exhibited a saturation in the layer growth after they reached a certain thickness of the intermetallic layers at different aging times. The slow saturated layer growth suggests a possible change in growth rate

controlling factor during aging. A possible explanation may rest with that a certain intermetallic layer thickness may cause this stabilization. If the intermetallic layer is thick enough to cause diffusion of Cu and Sn through it to become much slower, the solder joint may exhibit the saturation in the layer growth. Thus, the thickness of intermetallic layers themselves can be a controlling factor for the layer growth during long-term aging in this solder.

The growth of the intermetallic layers is influenced by factors such as (a) the Pb-rich phase accumulation at the intermetallic layer/solder interface, (b) the intermetallic layer thickness, (c) the Cu_6Sn_5 particles, and (d) the number of interface boundaries encountered by the diffusing species. The influence of each factor on the growth of the intermetallic layers is complicated.

A simple layer growth model was used to determine the layer-growth coefficients K for Cu_6Sn_5 and Cu_3Sn intermetallic layers, which is expressed as follows.

$$d = d_o + \sqrt{Kt}$$

where K is strongly related to the diffusion coefficient of atomic elements of the intermetallic layer. d is the intermetallic thickness (μm) at time t, d_o is the initial thickness (μm) of the intermetallic layer, K is the layer-growth coefficient (cm^2/sec), and t is the aging time (sec). The layer-growth coefficients were determined from a linear regression analysis of $(d\text{-}d_o)$ versus $t^{1/2}$, where the slope is $K^{1/2}$.

Figure 4.7 shows values of the layer-growth coefficients for Cu_6Sn_5 and Cu_3Sn layer growth obtained from plotting intermetallic layer thickness versus square root of time at 150°C. The linear correlation coefficients were generally greater than 0.9 for the

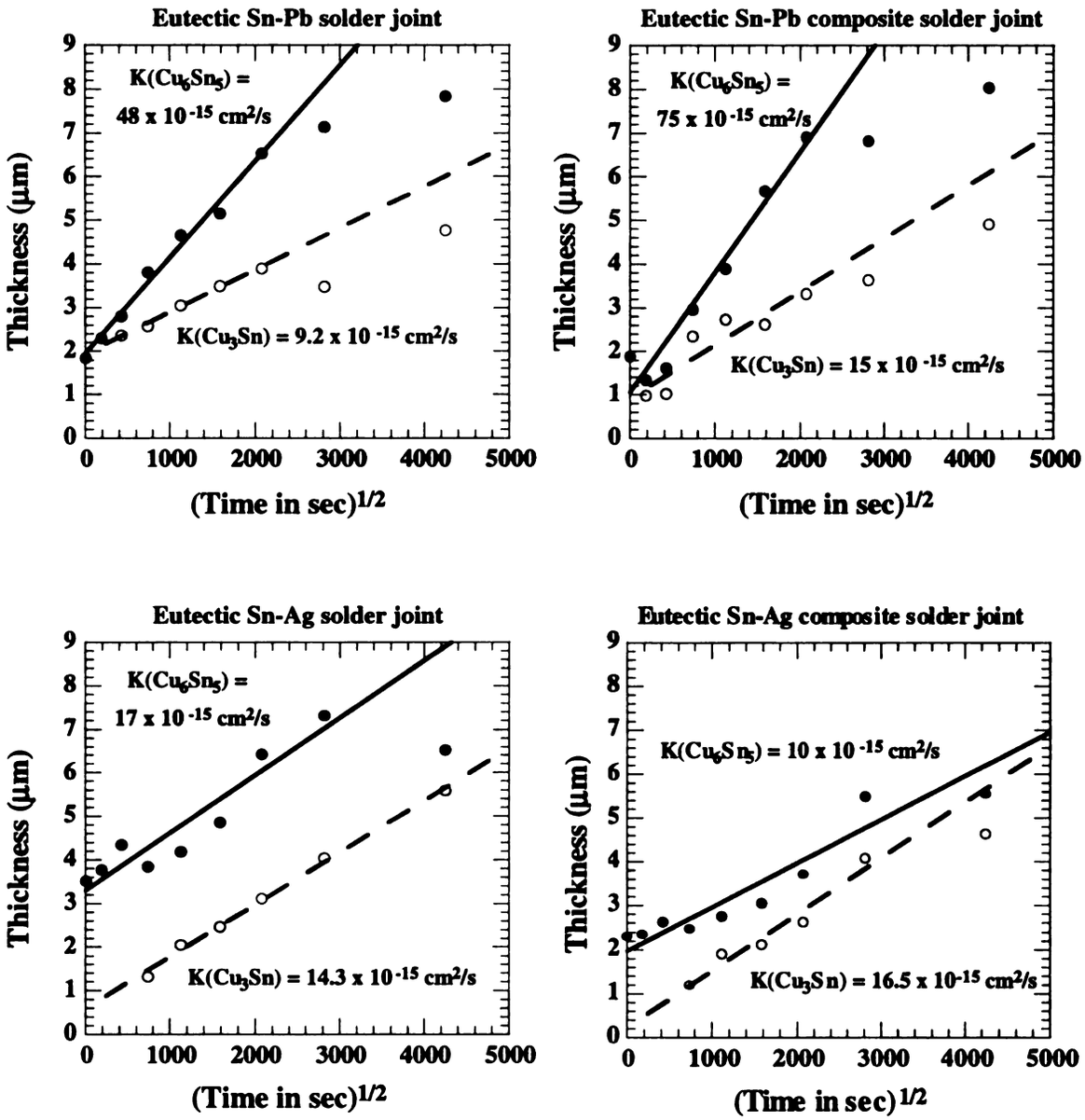

Figure 4.7 Thickness of the Cu_6Sn_5 and Cu_3Sn intermetallic layers versus square root of aging time at 150°C for the eutectic Sn-Pb and Sn-Ag solder joints, and their corresponding composite solder joints.

four types of solder joints used except the K value of 0.83 for the Cu_3Sn layer in the Sn-Pb composite and 0.84 for the Cu_6Sn_5 layer in the Sn-Ag composite. This good linear correlation suggests that a thermally activated diffusion process is valid approach for assessing the intermetallic layer growth.

Eutectic Sn-Pb composite solder joint showed higher layer-growth coefficients for the growth of Cu_6Sn_5 and Cu_3Sn layers than the corresponding non-composite solder joint. The high layer-growth coefficient values observed for Sn-Pb composite tend to suggest that the Cu_6Sn_5 particles, added *in-situ*, did not promote layer growth retardation, particularly in the later stage of aging. In contrast, both eutectic Sn-Ag solder joint and its composite counterpart exhibited comparable layer-growth coefficients for the Cu_6Sn_5 and Cu_3Sn intermetallic layers.

The eutectic Sn-Ag and its composite solder joints exhibited lower layer-growth coefficients for the Cu_6Sn_5 layer, and higher layer-growth coefficients for the Cu_3Sn layer than the eutectic Sn-Pb and its composite solder joints. The data in the Figure 4.7 resulted from the aging at the same temperature of 150°C. The same aging temperature of 150°C represents 0.85 for the eutectic Sn-Ag solder and 0.9 for the eutectic Sn-Pb solder in terms of their melting temperatures. Sn diffusion toward the intermetallic layers in the eutectic Sn-Ag and its composite solder joints was slower than in the eutectic Sn-Pb and its composite solder joints due to the aging at lower homologous temperature. The slower Sn diffusion resulted in lower layer-growth coefficients for the Sn-rich Cu_6Sn_5 intermetallic layer, and higher layer-growth coefficients for Cu-rich Cu_3Sn intermetallic layer.

The activation energies for the intermetallic layer growth was calculated using the Arrhenius relationship for the diffusion dominant process,

$$K = A\exp(-E^* / RT)$$

where K is the layer-growth coefficient (cm^2/sec), A is the layer-growth constant (cm^2/sec), E^* is the activation energy (J/mol) for layer growth, R is the ideal gas constant (8.314 J/mol K), and T is the absolute temperature (^oK). The activation energy is obtained from the slope of the ln K versus $1/T$ plot. Figure 4.8 is the Arrhenius plots from which the activation energies for the growth of the Cu_6Sn_5 intermetallic layer in the four solder joints can be obtained. The data reported here are in good agreement with the results from the previous studies [82,137,90,16,91]. Unfortunately, the analysis for the Cu_3Sn layer is not shown in this study because of lack of relevant data.

The two composite solder joints exhibited higher activation energies than their corresponding non-composite solder joints. Higher activation energies in the two composite solder joints appear to indicate that the Cu_6Sn_5 particles in the composite solders were effective in retarding the intermetallic layer growth. The higher activation energies, however, resulted from higher layer-growth coefficients at high aging temperature and lower layer-growth coefficients at low aging temperature. Therefore, it is evident that the Cu_6Sn_5 particles were not efficient diffusion barriers at high temperature, while they were effective barriers at low temperatures.

The activation energy values for the Cu_6Sn_5 intermetallic layer in this study are slightly higher than those reported from the previous studies, which are 77 kJ/mol for eutectic Sn-Pb solder [90], 118 kJ/mol for the eutectic Sn-Pb composite solder containing

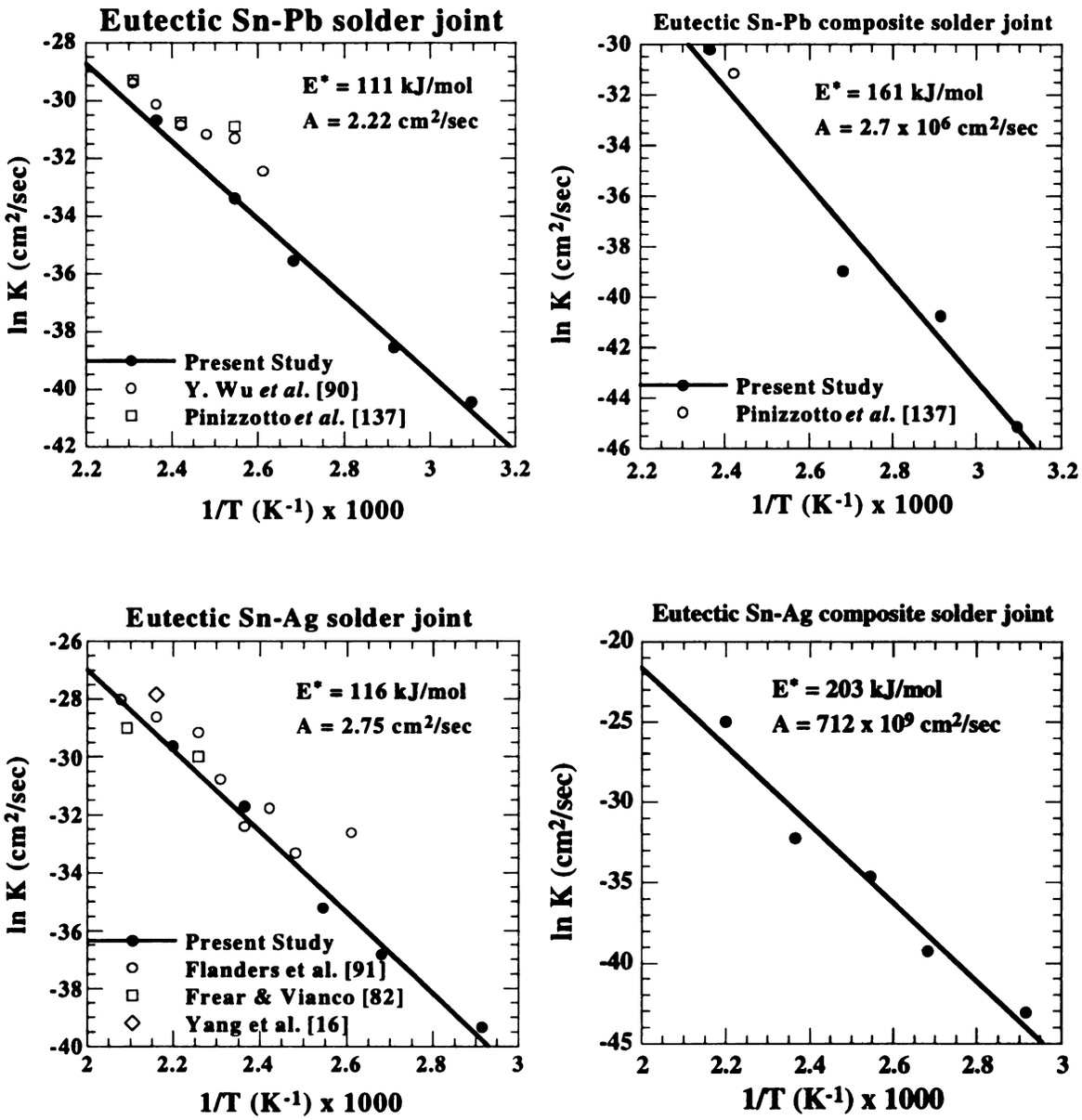

Figure 4.8 Arrhenius plots for the growth of Cu_6Sn_5 intermetallic layer in the eutectic Sn-Pb and Sn-Ag solder joints, and their corresponding composite solder joints based on the interfacial intermetallic layer thickness at 4000 hours of aging at different temperatures.

20 wt% Cu_6Sn_5 particles [90], and 107 kJ/mol for the eutectic Sn-Ag solder [91]. The previous studies [133,91] reported that the aging at low temperatures less than 110°C up to about 2184 hours did not cause significant growth of the intermetallic layers. However, the four solder joints studied here revealed slight increases of the Cu_6Sn_5 intermetallic layer at low temperature of 70 and 50°C during the long-term aging up to 5000 hours. The slightly higher activation energy values for the intermetallic layer growth in this study appear to result from the low layer-growth coefficients produced at low aging temperature during long-term aging up to 5000 hours.

4.4 CONCLUSION

This study detailed the microstructural evolution and growth kinetics of the Cu_6Sn_5 and Cu_3Sn intermetallic layers in the eutectic Sn-Pb and Sn-Ag solders, and their corresponding composites during aging at temperatures ranging 50°C to 180°C up to 5000 hours. During aging, the eutectic Sn-Pb and Sn-Ag solder phases revealed extensive coarsening and the intermetallic layers also grew significantly. The intermetallic layers in the composite solder joints exhibited undesirable features, specifically, (a) coarsening of the Cu_6Sn_5 particles, (b) the 'abnormal' growth of the intermetallic layer.

Factors such as Pb-rich phase accumulation, the layer thickness itself, the aging temperature, and Cu_6Sn_5 particles play significant roles in the growth of the intermetallic layer. The Cu_6Sn_5 particles affected the growth of the intermetallic layers at the initial stage of aging for the eutectic Sn-Pb composite solder joint. However, there was no effect of the Cu_6Sn_5 particles for the intermetallic layer growth in the Sn-Ag composite

solder joint aged at 150°C for long periods of time, even though there was an apparent effect on the intermetallic layer formation during soldering. The Cu_6Sn_5 particles were effective in reducing the layer growth in Sn-Pb and Sn-Ag composite solder joints for low temperature aging, but at high temperatures above 150°C significant coarsening of the Cu_6Sn_5 particles was observed and caused the enhanced intermetallic layer growth.

A possible mechanism which can explain the effect of the Cu_6Sn_5 particles on the kinetics of intermetallic growth is based on assuming that the particles act as barriers to the Sn-diffusion toward intermetallic layer and reduce the amount of Sn available at the interface for reaction.

CHAPTER 5

FORMATION AND GROWTH OF INTERFACIAL INTERMETALLIC LAYERS IN EUTECTIC Sn-Ag SOLDER AND ITS COMPOSITE SOLDER JOINTS

ABSTRACT

Single shear lap joints were made by soldering two Cu substrates with eutectic Sn-Ag solder, and its composite solders containing $FeSn/FeSn_2$ or Ni_3Sn_4 intermetallic particles introduced by *in-situ* method. Aging of solder joints was performed at 70, 100, 120, 150, 180°C for 1400 hours. The growth of the interfacial intermetallic compound (IMC) layers was characterized assuming diffusion-controlled growth kinetics. Effects of such $FeSn/FeSn_2$ and Ni_3Sn_4 particulates on the IMC layer growth rate were extensively characterized. Composite solder joints in the fabricated condition formed thinner IMC layers compared to the corresponding non-composite solder joints. The Cu_6Sn_5 IMC layer grew faster at temperatures above 120°C(T/T_m = 0.8), while growing slower at temperatures below 120°C in composite solder joints. *In-situ* introduced $FeSn/FeSn_2$ and Ni_3Sn_4 particle reinforcements in composite solder joints proved effective in reducing the overall growth of the interfacial Cu_6Sn_5 IMC layer only at lower temperatures. Composite solder joints exhibited slower growth of the Cu_3Sn layer during aging at all temperatures used in this study. Two different regions having different activation energies depending on the temperature were identified for the growth of Cu_6Sn_5 and Cu_3Sn IMC layers.

5.1 INTRODUCTION

Solders will bond with a Cu substrate through the formation of a dual Cu-Sn intermetallic compound (IMC) layer consisting of Cu_6Sn_5 and Cu_3Sn that exist between the solder and Cu substrate. The Cu_6Sn_5 layer forms adjacent to the solder side and the Cu_3Sn layer next to the Cu substrate. Over time in service, these layers grow in the solid state and occupy a significant portion of the solder joint. Because IMC layers are more brittle than the solder matrix, they can be a site of mechanical weakness causing failure of the joint with the fracture in the IMC layer itself or along the interface between solder and IMC layer [133,82].

Several studies have been carried out on the growth kinetics of IMC layers [135,136,89,90,16,91] and their subsequent effects on the mechanical properties of solder joints [138,83,139,140]. Most of these studies deal with IMC layer in Pb-Sn solder joints, and complementary Pb-Sn composite solder joints [133,135,89,90,138-140]. In contrast, fewer studies exist on the formation and growth of IMC layers in eutectic Sn-Ag solder and eutectic Sn-Ag based composite solder joints [82,16,91].

This study investigates formation and growth of IMC layers in eutectic Sn-Ag solder and its composite solder joints during long-term isothermal aging up to 1400 hours. Our previous study [141] investigated the effects of *in-situ* introduced Cu_6Sn_5 particles on the growth of IMC layers in both Sn-Ag and Pb-Sn solder joints. In this study, the effects of *in-situ* introduced Fe-Sn and Ni_3Sn_4 particle reinforcements on the growth of IMC layers in eutectic Sn-Ag solder were characterized. A comparison was made between composite solders reinforced with Fe-Sn, Ni_3Sn_4, and Cu_6Sn_5 particles.

The growth kinetics of IMC layers was determined as a function of time and temperature assuming a diffusion-controlled growth model.

5.2 EXPERIMENTAL DETAILS

Three types of solders were used in this study, eutectic Sn-Ag and its composite solders containing FeSn/$FeSn_2$ or Ni_3Sn_4 intermetallic reinforcement particles. Eutectic Sn-Ag solder was provided in the form of ingots cast by Alpha Metals. Composite solders were prepared by incorporating additional Ni and Sn or Fe and Sn to introduce about 20 vol.% $FeSn_2$ or Ni_3Sn_4 intermetallic particulate reinforcements into the eutectic Sn-Ag solder using *in-situ* method. However, the composite solder reinforced with Fe and Sn produced two different compositions of particles, FeSn and $FeSn_2$, as illustrated in Figure 5.1. The ratio of FeSn and $FeSn_2$ in particulate reinforcements is not clear at present. The compositions of composite solders are listed in Table 5.1.

Single shear lap joints were made using solder preform foils with two dog-bone shaped Cu strips together. Fabrication and preparation methods of solder joint specimens are described in detail in Chapter 4. Excess solder present on both sides of the joints were ground off, and one of its sides was polished using 400 and 2000 grit sand papers followed by a finish using 0.05 μm SiO_2 colloidal suspension. The solder joints were etched with a solution of 40% H_2O/40% NH_4OH/20%H_2O_2 for about 10 seconds to reveal microstructural features.

Solder joints were then isothermally aged at five temperatures of 70, 100, 120, 150, 180°C for long time periods up to 1400 hours by placing them at different locations on an aluminum plate heated by a hot plate at the end so that is maintained at these steady

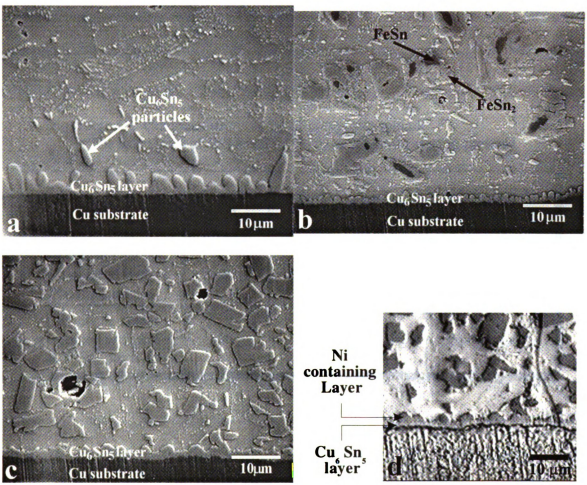

Figure 5.1 SEM micrographs showing the microstructures of as-made solder joints, (a) eutectic Sn-Ag solder joint, (b) composite solder joint containing FeSn/$FeSn_2$ particles, (c) composite solder joint containing Ni_3Sn_4 particles, (d) optical micrograph showing the layer containing Ni element in composite solder joint containing Ni_3Sn_4 particles.

Table 5.1 Compositions (vol %) of composite solders
(*The exact ratio of FeSn and $FeSn_2$ particles is not clear at present).

	Eutectic Sn-Ag	Ni	Fe	Sn	Introduced intermetallics
Composite solder reinforced with Ni_3Sn_4 particles	80	5.1		16.84	20 vol% Ni_3Sn_4
Composite solder reinforced with FeSn & $FeSn_2$ particles	80		4.12	18.98	FeSn & $FeSn_2$

temperatures. The solder joints were removed from the set-up periodically, and were slightly repolished to reveal the resultant microstructure using an optical microscope. In order to measure the IMC layer thickness, optical micrographs of IMC layers between solder and Cu substrate were scanned with HG Scanet 3C scanner and then analyzed using Adobe Photoshop software. The average value of 10 measurements per micrograph was used to analyze the growth kinetics of IMC layers.

5.3 RESULTS AND DISCUSSION

Figure 5.1 shows the as-joined microstructures of solder joints prior to aging. Typically, eutectic Sn-Ag joints consisted of Sn dendrites and eutectic Sn-Ag phases having Sn phase peppered with fine Ag_3Sn particles as shown in Figure 5.1a. The microstructures of composite solder joints containing $FeSn/FeSn_2$ or Ni_3Sn_4 intermetallic particles in a eutectic Sn-Ag solder matrix are shown in Figure 5.1b and 5.1c, respectively. *In-situ* introduced Fe-Sn particles were found to be of two types, FeSn and $FeSn_2$, as evidenced by the different contrast shown in Figure 5.1b. According to Fe-Sn phase diagram [142], these two intermetallic compositions are possible in this system. The Fe-rich FeSn is shown by the dark contrast in the inside region of Fe-Sn particles, and Sn-rich $FeSn_2$ is exhibited by the light contrast in the outside region of Fe-Sn particle.

The solder joints have been found to form two IMC layers between solder and Cu substrate, Sn-rich Cu_6Sn_5 layer adjacent to the solder and Cu-rich Cu_3Sn layer adjacent to the Cu substrate, as identified in phase diagram of Cu-Sn binary system [16,82,83,89-91,133,135,136,138-141]. The non-composite and composite solder joints in as-

fabricated condition contained a continuous Cu_6Sn_5 IMC layer between solder and Cu substrate formed by the reaction of Sn and Cu during reflow. The Cu_3Sn IMC layer which has been identified to form during reflow [90] was not clearly visible in the as-joined solder joints of this study. Few Cu_6Sn_5 particles were found in the solder matrix of as-fabricated joint as shown in Figure 5.1a. Cu_6Sn_5 particles appear to exist in solder matrix by breaking of Cu_6Sn_5 scallop from the Cu_6Sn_5 IMC layer and entering the solder matrix during reflow. Composite solder joint having Ni_3Sn_4 particles exhibited an additional component to the Cu_6Sn_5 layer which contained Ni as shown in Figure 5.1d. This observation suggests that Ni_3Sn_4 particles in composite solder participated in the formation of IMC layer during reflow, resulting in Ni containing layer adjacent to Cu_6Sn_5 IMC layer. The exact composition of the Ni containing layer is not clear at present. The Ni containing layer was not included in the quantitative analysis of Cu_6Sn_5 and Cu_3Sn IMC layer growth, but was considered in computing the total thickness of IMC layers.

Figure 5.2 shows the microstructures of solder joints after aging at 180°C for 1400 hours. The Ag_3Sn particles present in the solder exhibited a significant amount of coarsening as has been observed in previous studies [16,25]. Few Cu_6Sn_5 particles that were present in as-joined non-composite eutectic Sn-Ag solder joint also showed considerable coarsening during aging [16]. The $FeSn/FeSn_2$ and Ni_3Sn_4 particles in composite solder joints were stable during aging in this study, as compared to Cu_6Sn_5 reinforcing particles that exhibited significant coarsening during aging for 5000 hours at this temperature [141]. Ag_3Sn particles were also found to be embedded within the Cu_6Sn_5 layer and in Cu_6Sn_5 particles of the solder matrix. Such an embedding of Ag_3Sn particles is attributed to the depletion of Sn close to the Cu_6Sn_5 layer and Cu_6Sn_5 particles

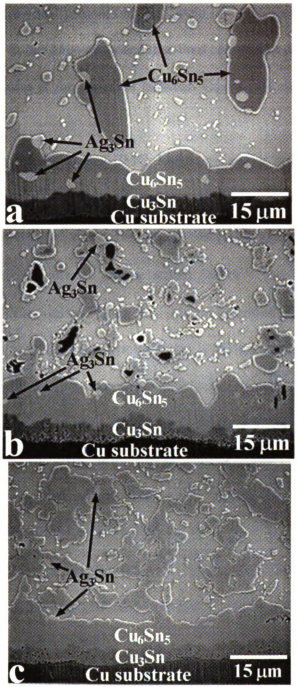

Figure 5.2 SEM micrographs showing the microstructures of solder joints after aging at 180°C for 1400 hours, (a) eutectic Sn-Ag solder joint, (b) composite solder joint containing FeSn/$FeSn_2$ particles, (c) composite solder joint containing Ni_3Sn_4 particles.

within solder matrix [141,91]. The Cu_6Sn_5 and Cu_3Sn layers exhibited significant growth during aging. There were voids present only in Cu_3Sn layer apparently due to Kirkendall effect in diffusion [15]. It has been proposed that void coarsening during aging can cause the failure of a solder joint at the interface between Cu_3Sn IMC layer and Cu substrate [16].

Initial thicknesses of interfacial IMC layers of solder joints in the as-joined condition are provided in Figure 5.3. Composite solder joints exhibited thinner IMC layer, with average thickness of about 2.0 μm, as compared to an average thickness of about 3.8 μm observed in eutectic Sn-Ag solder joints. The IMC layer thickness differences are readily observed in Figure 5.1. In our previous study [141], composite solder joints reinforced with Cu_6Sn_5 particles in the as-joined condition also produced a thinner IMC layer than did the non-composite eutectic Sn-Ag solder joint in the as-joined condition. These observations indicate that reinforcing particles affect the formation and its initial thickness of the IMC layer during the joining operation.

Plots illustrating the growth of total IMC layers (including both Cu_6Sn_5 and Cu_3Sn) at five temperatures up to 1400 hours are presented in Figure 5.4. Both non-composite and composite Sn-Ag solder joints exhibited a similar behavior. The growth of total IMC layer was considerably faster at higher temperatures of 180 and 150°C, as compared to that at lower temperatures below 120°C.

The IMC layers, Cu_6Sn_5 and Cu_3Sn layers, present in solder joints are formed by the reaction of Sn in solder matrix and Cu from Cu substrate during reflow and grow upon aging. The growth of IMC layers occurs through diffusion of Cu and Sn in opposite directions. In this study, due to the complexity of two diffusing atomic species in

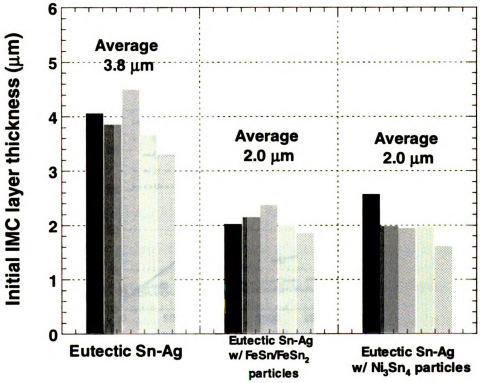

Figure 5.3 Initial thicknesses of IMC layers in eutectic Sn-Ag and composite solder joints.

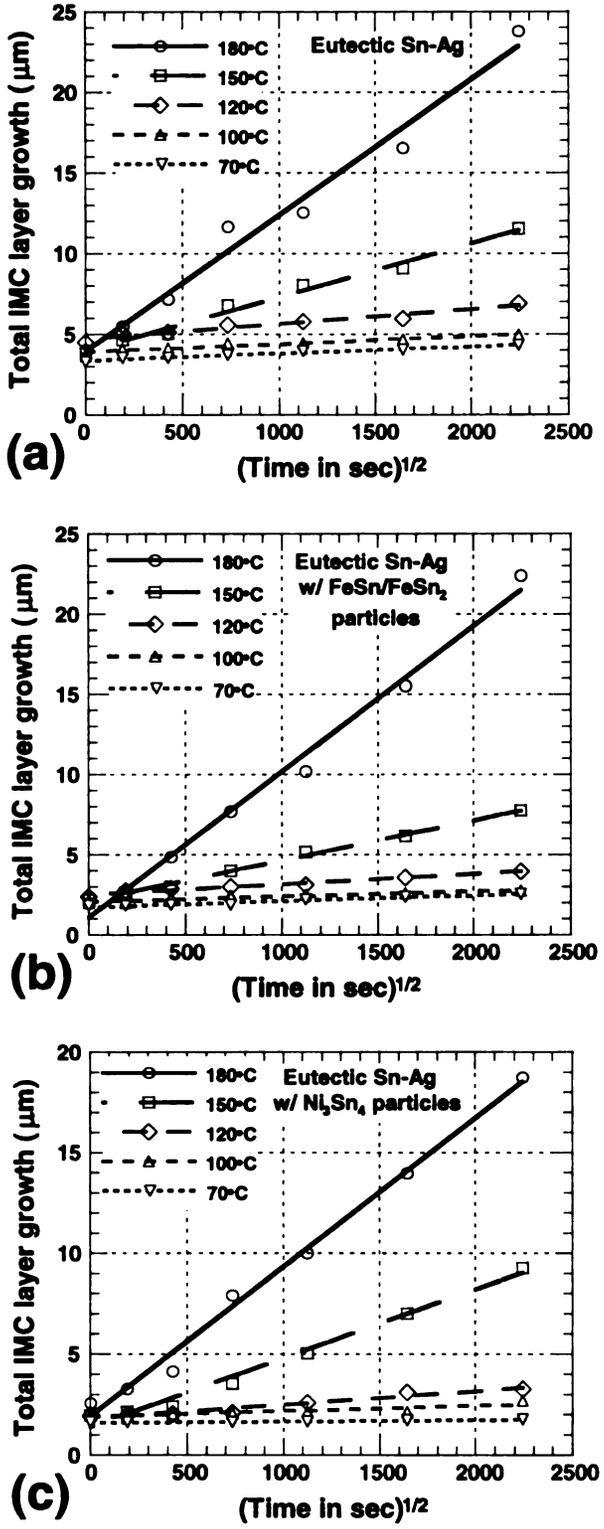

Figure 5.4 The growth of total IMC layer (both Cu_6Sn_5 and Cu_3Sn) during aging up to 1400 hours, (a) eutectic Sn-Ag solder joints, (b) composite solder joint with $FeSn/FeSn_2$ particles, (c) composite solder joints with Ni_3Sn_4 particles.

opposite directions, the thickness measurements of IMC layers were used to address the growth kinetics of the IM layers during aging, assuming diffusion-controlled growth of IMC layers by Sn and Cu in opposite directions. As a result, layer growth coefficient is used for analysis in solder studies, rather than traditional diffusion coefficient based equations [141].

The growth kinetics of the Cu_6Sn_5 and Cu_3Sn IMC layers was determined using a simple growth model,

$$d = d_o + \sqrt{Kt}.$$

The layer-growth coefficient, K, is strongly related to the diffusion coefficient of diffusing atomic species determining the growth of the IMC layers. d is the IMC layer thickness at aging time t, and d_o is the initial thickness of the IMC layers. The layer-growth coefficient, K, was determined from a linear regression analysis of d versuss $t^{1/2}$, where the slope is $K^{1/2}$. K is then related to activation energy for the growth of IMC layers by Arrhenius relationship describing the temperature dependence of K as follows :

$$K = A\exp\left(-E^*/RT\right)$$

where A is the temperature-independent pre-exponential factor, E^* is the activation energy for the IMC layer growth, R is the ideal gas constant, and T is the absolute temperature. The activation energy was calculated from the slope of $ln\ K$ vs $1/T$ plot.

The layer-growth coefficients, K, for the growth of Cu_6Sn_5 and Cu_3Sn IMC layers

Table 5.2 Calculated layer-growth coefficients for the growth of IMC layers.

	Temperature (°C)	Eutectic Sn-Ag		Eutectic Sn-Ag with $FeSn/FeSn_2$ particles		Eutectic Sn-Ag with Ni_3Sn_4 particles	
		K ($10^{-15}cm^2/sec$)	R^2	K ($10^{-15}cm^2/sec$)	R^2	K ($10^{-15}cm^2/sec$)	R^2
Cu_6Sn_5 IMC layer	180	214	0.931	337	0.974	235	0.983
	150	19.8	0.929	23.8	0.983	71.7	0.987
	120	1.33	0.919	1.72	0.917	1.22	0.941
	100	0.85	0.973	0.14	0.97	0.11	0.963
	70	0.76	0.935	0.11	0.948	0.043	0.981
Cu_3Sn IMC layer	180	144	0.998	107	0.956	64.4	0.939
	150	37.7	0.99	9.41	0.986		
	120	3.15	0.904	0.56	0.674		
	100	0.41	0.688				
	70	0.21	0.659				

in non-composite and composite solder joints at 180, 150, 120, 100, and 70°C are provided in Table 5.2. Most of the linear correlation factor, R^2, were greater than 0.9. This study and other previous studies [89,16,91] confirm that the growth of IMC layers is diffusion-controlled in both non-composite and composite solder joints over the temperature range studied.

At higher aging temperatures of 180 and 150°C, composite solder joints had higher layer-growth coefficients for the Cu_6Sn_5 IMC layer growth than non-composite solder joints. At an intermediate aging temperature of 120°C, both non-composite and composite solder joints exhibited similar layer-growth coefficients. These observations suggest that $FeSn/FeSn_2$ and Ni_3Sn_4 particles have no substantial effects on reducing the growth of Cu_6Sn_5 layer during aging at temperatures above 120°C. Therefore, $FeSn/FeSn_2$ and Ni_3Sn_4 particles are not expected to reduce the layer growth in conditions encountered in automotive under-the-hood environment, where the temperature can reach as high as 150°C [2].

On the contrary, composite solder joints exhibited lower layer-growth coefficients for the growth of Cu_6Sn_5 layer than non-composite solder joints at lower aging temperatures of 100 and 70°C. This indicates that the reinforcement particles in composite solder are effective in reducing the growth of Cu_6Sn_5 layer at temperatures below 120°C. Thus, composite solders containing $FeSn/FeSn_2$ or Ni_3Sn_4 particles would be beneficial in stabilizing the Cu_6Sn_5 layer in relatively low-temperature applications such as in microelectronic components in typical office/home environment.

The growth of Cu_3Sn layer was slower in composite solder joints than in the non-composite Sn-Ag solder joint at all aging temperatures used in this study as shown in

Table 5.2. This observation is consistent with that in a previous study [90] in which Ni retarded the growth of Cu_3Sn layer while increasing the growth of Cu_6Sn_5 layer. Moreover, the Cu_3Sn IMC layer became visible only at a far later aging time in composite solder joints aged at lower temperatures than in the non-composite solder joints. The composite solder joints thus were efficient in reducing the growth of Cu_3Sn layer at temperatures used in this study than the non-composite Sn-Ag solder.

Figures 5.5 and 5.6 are the Arrhenius plots from which activation energies for the growth of Cu_6Sn_5 and Cu_3Sn layers were obtained. The best fit to the K vs T data shows that the activation energies for Cu_6Sn_5 and Cu_3Sn layer were temperature dependent. Such results suggest that the controlling mechanisms for Cu_6Sn_5 and Cu_3Sn layer growth are different at high and low temperatures. The activation energies for the growth of Cu_6Sn_5 layer in the non-composite and composite solder joints with $FeSn/FeSn_2$ or Ni_3Sn_4 particles at higher temperature region ($T/T_m \sim 0.8 - 0.92$) were 1.3, 1.38, and 1.46 in eV/atom, respectively. Higher activation energies in composite solder joints were due to the higher layer-growth coefficients at higher aging temperatures of 180 and 150°C. The activation energy of 0.12 eV/atom in the non-composite solder joint in low temperature region was quite lower than that at higher temperatures. The activation energy in composite solder joints at lower temperatures was not determined because of insufficient data. The activation energy for Cu_3Sn IMC layer growth in the composite solder joint with $FeSn/FeSn_2$ particles was higher than that in non-composite solder joint. The activation energy for Cu_3Sn IMC layer growth in composite solder joints could not be determined due to the inability to visually resolve the Cu_3Sn layer.

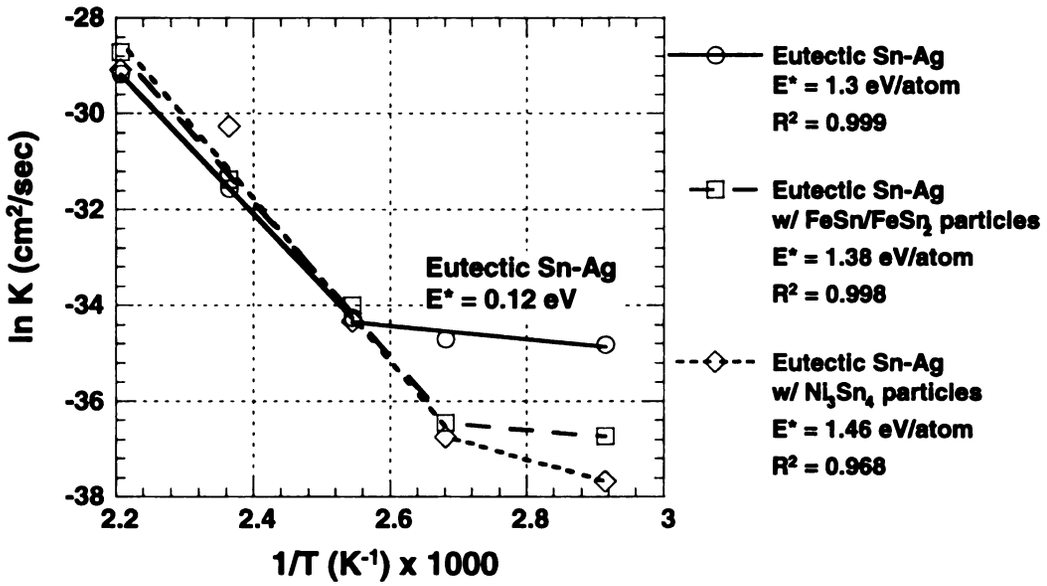

Figure 5.5 Arrhenius plot for the growth of Cu_6Sn_5 IMC layer in eutectic Sn-Ag and composite solder joints.

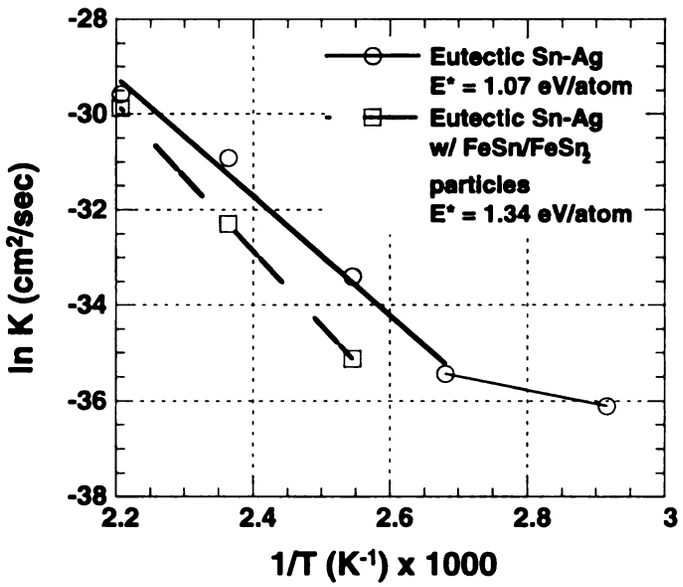

Figure 5.6 Arrhenius plot for the growth of Cu_3Sn IMC layer in eutectic Sn-Ag and composite solder joints.

5.4 SUMMARY

The formation and growth kinetics of Cu_6Sn_5 and Cu_3Sn layers during isothermal aging up to 1400 hours were investigated in non-composite and composite Sn-Ag solder joints. The Ag_3Sn particles showed significant coarsening while $FeSn/FeSn_2$ and Ni_3Sn_4 particles remained stable during the aging in this study. Voids were present only within Cu_3Sn layer due to Kirkendall effect. The microstructures of composite solder joints revealed thinner initial IMC layers than non-composite solder joints, thus suggesting an influence of $FeSn/FeSn_2$ and Ni_3Sn_4 particles on the formation of IMC layers.

Both non-composite and composite Sn-Ag solder joints exhibited a similar behavior in the growth of IMC layers. For the Cu_6Sn_5 layer, the layer-growth coefficients at temperatures above 120°C were higher in composite solder joints, while composite solder joints exhibited lower layer-growth coefficients at temperatures below 120°C. $FeSn/FeSn_2$ and Ni_3Sn_4 particles were effective in reducing the growth of Cu_6Sn_5 layer at lower temperatures. In the present study, it was revealed that Cu_3Sn IMC layer grew slower in composite solder joints at all temperatures. The growth of Cu_6Sn_5 and Cu_3Sn IMC layers appeared to be controlled by two different temperature-dependent diffusion related mechanisms.

CHAPTER 6

CREEP PROPERTIES OF EUTECTIC Sn-Ag SOLDER JOINTS AND Sn-Ag COMPOSITE SOLDER JOINTS CONTAINING INTERMETALLIC PARTICLES INTRODUCED BY *IN-SITU* METHODS

ABSTRACT

Creep behavior of the eutectic Sn-Ag joints and Sn-Ag composite solder joints containing 20 Vol.% of Cu_6Sn_5, Ni_3Sn_4, and $FeSn_2$ intermetallic reinforcements introduced by *in-situ* methods was investigated. These creep tests were carried out using single shear lap solder joints at room temperature, 85, and 125°C. The creep resistance was similar in magnitude for all alloys, and with increasing temperature, the stress exponents decreased in a manner consistent with power-law breakdown behavior. The $FeSn_2$ intermetallic reinforced composite solder was found to be the most creep resistant alloy at room temperature. Creep failure was observed to occur within the solder matrix in all these solder joints. Although the smearing of the features present in the fracture surface made a detailed analysis of the processes involved difficult, there were indications of grain boundary separation, ductile fracture, and interfacial separation.

6.1 INTRODUCTION

Global economic and environmental pressures warrant that lead be removed from electronic solders [143]. Another concern in the electronics industry is that performance limitations of Sn-Pb solders are being exhausted due to requirements of surface mount technology. In many electronic systems, the majority of reliability losses were identified with mechanical failures of the solder joints rather than device malfunctions [3]. Several Pb-free solders have been considered as alternatives to Sn-Pb solders. Among potential Pb-free solders, eutectic Sn-Ag solder (Sn-3.5Ag in wt%) is amongst the leading Pb-free candidates [11,14,21,15]. Also for electronic systems used in harsh conditions such as automotive under-the-hood and aerospace applications, a composite solder approach has been proposed to improve the performance of solders [25,92,26].

In thermomechanical fatigue at high homologous temperatures, both thermal and athermal processes are operative [11]. At high frequencies or low temperatures, failure is dominated by athermal processes. However, at low strain-rates or high temperatures, creep deformation dominates. Creep has been identified as a major deformation mode of the solder joint. Grain boundary sliding, an important deformation mechanism in creep, was typically observed in thermomechanically fatigued solder joints [13].

Creep deformation of the Sn-3.5Ag solder has been investigated in many studies [92,45,12,46,30,53,48]. However, there is no clear agreement about the responsible creep mechanism. A brief summary on the creep property of the Sn-3.5Ag solder is given next to elucidate the current understanding.

Mathew *et al.* [45] reported that the Sn-3.5Ag bulk solder of 20μm grain size exhibited the stress exponent of 5 and 60.7 kJ/mol activation energy. They compared this

data with the creep data of pure Sn of 150μm grain size with a stress exponent of 7.6 and an activation energy of 60.3 kJ/mol and cited lattice diffusion-controlled dislocation climb as the controlling mechanism. Despite the difference in stress exponents, creep deformation of Sn-3.5Ag solder was therefore attributed to the same mechanism as that of pure Sn. Yang *et al.* [12] and Liang *et al.* [46] regarded Sn-3.5Ag solder as a particle-hardened alloy. Dislocation climb over the Ag_3Sn particles was considered as the rate-controlling mechanism.

Darveaux *et al.* [30] performed creep tests using actual ball grid arrays of Sn-3.5Ag solder joints. From the measured stress exponent of 5.5, they concluded that dislocation climb was the controlling mechanism. However, the observed activation energy of 38.5 kJ/mol was considerably lower than the expected value of lattice (106 kJ/mol) or dislocation pipe (63kJ/mol) diffusion in pure Sn. They surmised that the activation energy was stress dependent since the data was in the power law break down regime, producing a lower activation energy than usual.

Igoshev *et al.* [53] suggested other mechanisms such as grain boundary sliding and/or dislocation movement to account for observed stress exponents higher than 5. Other microstructural studies on crept specimens appear to support this suggestion [53,48] Frear [48] reported that the creep strain was accommodated through the Sn matrix of 1 μm grain size, at Sn-Sn grain boundaries. Igoshev *et al.* [53] observed that microcracks were accumulated at grain boundaries due to grain boundary sliding, leading to an intergranular fracture. The accumulation of grain boundary defects started at an earlier stage of creep and lasted for at least 70 ~ 80 % of the lifetime.

In our previous study [92], Sn-3.5Ag solder joints reinforced with Cu_6Sn_5 particles showed two or three order of magnitude higher creep resistance in as-fabricated condition, compared to the eutectic Sn-Ag solder joint. But with aging, the difference in creep resistance was less dramatic. In this study, the creep deformations of unaged Sn-3.5Ag solder and its *in-situ* composite solders reinforced with Cu_6Sn_5, Ni_3Sn_4, or $FeSn_2$ are characterized by constant-load creep testing of single shear lap solder joints. The effects of creep test methodology and reinforcement particles on measured creep properties are discussed. The significance of the particle type in creep resistance is examined. Fracture processes during the creep of the solder joints are also investigated.

6.2 EXPERIMENTAL PROCEDURES

Sn-3.5Ag solder stock was received in the form of cast ingots. Sn-Ag composite solders were prepared by incorporating 20 Vol.% Cu_6Sn_5, Ni_3Sn_4, or $FeSn_2$ intermetallic particles into the Sn-3.5Ag solder by *in-situ* methods. The composite solders were made by intrinsically producing the intermetallic reinforcements within the solder, rather than by mechanically adding intermetallic particles to the solder. The Sn-3.5Ag and composite solders were rolled to produce a sheet of about 100 μm thick and cut into preforms of about 1.0 mm^2 area. Single shear lap joints with an area of about 1 mm^2 were fabricated with preforms of the solders by soldering together two Cu substrates of semi-dogbone shape. Further experimental details about fabrication of the solder joint were described in Chapter 4 [141]. The solder joints were prepared for microstructural examination by standard metallographic techniques, finishing with 0.05 μm SiO_2 colloidal suspension.

Constant load creep tests were performed by hanging a dead-load on one side of the single shear lap solder joint mounted on an aluminum beam. Tests were conducted in air at room temperature, 85°C, and 125°C, with the applied stress varying from 3 to 25 MPa. Figure 6.1 shows how a test specimen was set up to do elevated temperature creep experiments. Such testing was carried out using a small heating pad affixed to the side of the Cu substrate, which was electrically connected to a variable transformer. The temperature was measured by a thermocouple soldered closely to the joined region of the Cu substrates.

Creep strain was measured using laser ablation patterns placed on the side of the solder joint by an excimer laser before creep testing [144]. Optical microscopic images of laser patterns were taken periodically. The creep strain was determined by calculating the changes in slope of the laser patterns, which distort from the original position with time. Details of creep data analysis using this method was described in our previous study [145].

The fracture surfaces of the solder joints were examined by scanning electron microscopy after the solder joints failed. The actual stress applied to the solder joint was determined by dividing the applied load by the actual joined area, obtained after subtracting the large void area in a solder joint cut by the fracture plane.

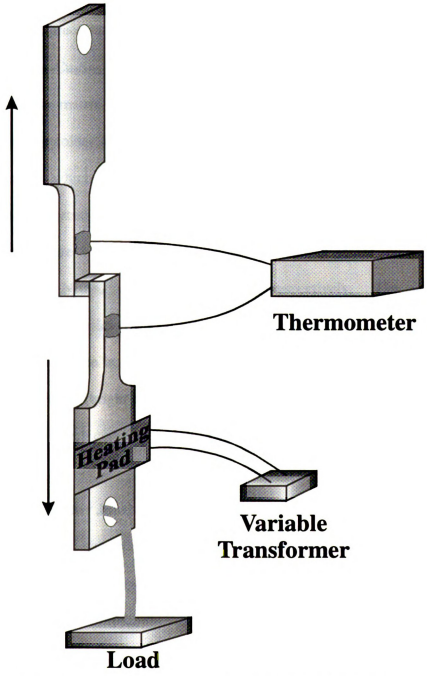

Figure 6.1 Schematic drawing of creep testing method.

6.3 RESULTS AND DISCUSSION

Initial Microstructure

The microstructure of a eutectic Sn-Ag solder joint in Figure 6.2(a) shows the Cu substrate, continuous Cu_6Sn_5 interfacial layer, and eutectic Sn-Ag solder matrix. The eutectic Sn-Ag solder matrix consisted of almost pure Sn grains peppered with Ag_3Sn particles. Within the solder matrix, a few Cu_6Sn_5 intermetallic particles were observed near the Cu substrate, which were formed during reflow of the solder joint [84].

Particulate reinforced Sn-3.5Ag composite solder joints, Figures 6.2 (b) ~ (d), showed a microstructure similar to that of the eutectic Sn-Ag solder joint along with incorporated Cu_6Sn_5, Ni_3Sn_4, and $FeSn_2$ particles, respectively. The solder joint reinforced with $FeSn_2$ particles revealed that some $FeSn_2$ possessed a dual composition manifested by the difference in contrast, indicating two different intermetallics of FeSn (dark contrast) and $FeSn_2$ (bright contrast). There were variations in the particle shape and size distribution in each composite solder joint.

Creep Properties of Solder Joints

Figures 6.3 (a) ~ (d) show the variation of secondary creep strain-rate with applied stress at various temperatures for eutectic Sn-Ag solder joints and its composite solder joints. A power law relationship of the form,

$$\dot{\gamma} = A\tau^n,$$

describes the data over the stress ranges and temperatures used in this study, with some scatter in the data. $\dot{\gamma}$ is the shear strain-rate, τ and n are the shear stress and stress

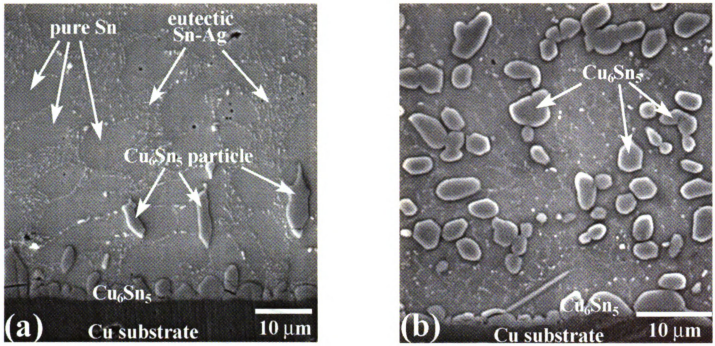

Figure 6.2 (a) & (b) SEM micrographs showing initial microstructure of the solder joint. (a) eutectic Sn-Ag solder, (b) Cu_6Sn_5 particle reinforced Sn-3.5Ag solder.

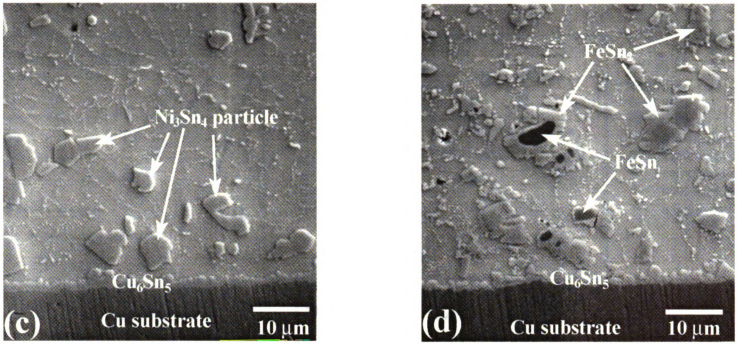

Figure 6.2 (c) & (d) SEM micrographs showing initial microstructure of the solder joint.
(c) Ni_3Sn_4 particle reinforced Sn-3.5Ag solder, (d) $FeSn_2$ particle reinforced Sn-3.5Ag solder.

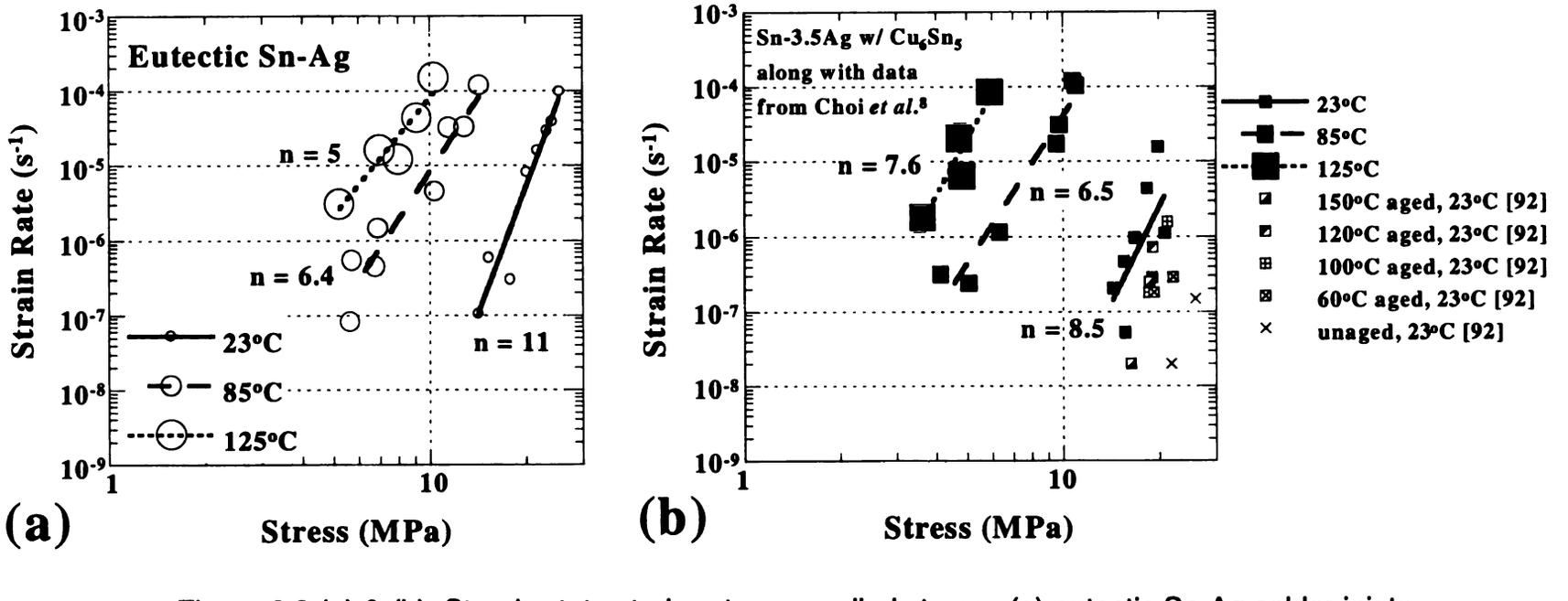

Figure 6.3 (a) & (b) Steady state strain-rate vs. applied stress. (a) eutectic Sn-Ag solder joints, (b) Cu_6Sn_5 composite solder joints along with data from Choi *et al.* [92].

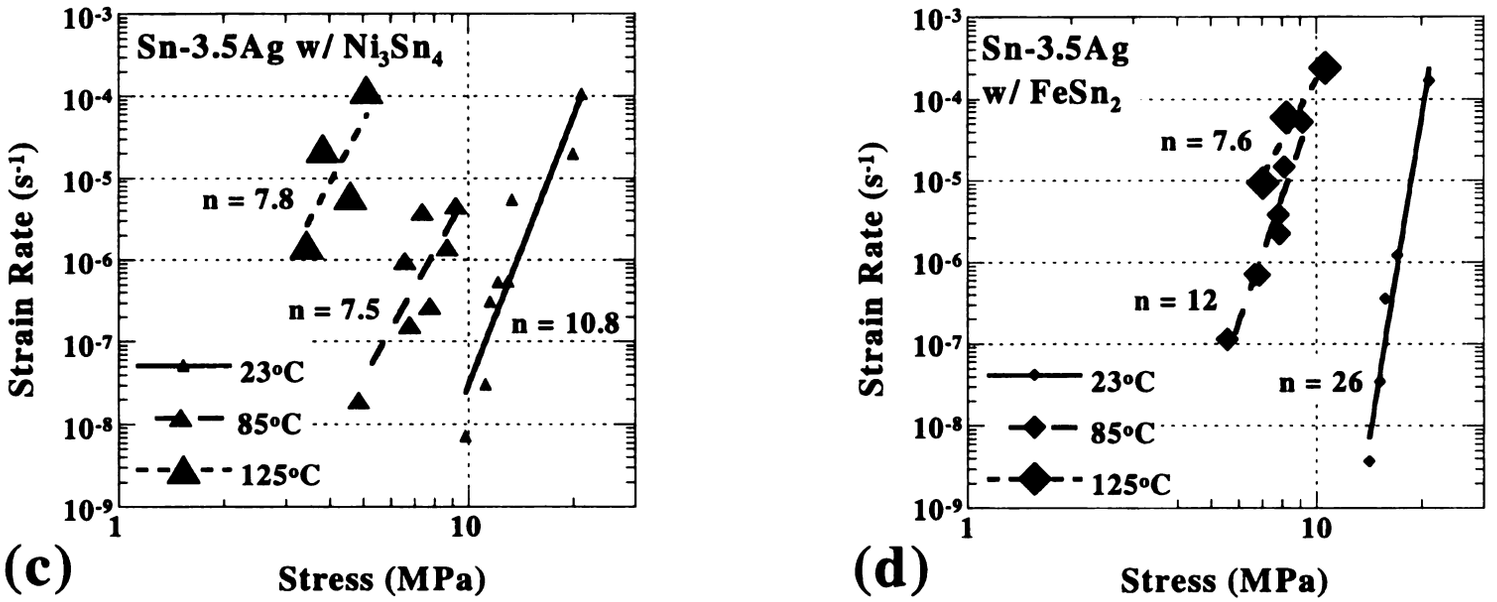

Figure 6.3 (c) & (d) Steady state strain-rate vs. applied stress.
(c) Ni_3Sn_4 composite solder joints, (d) $FeSn_2$ composite solder joints.

exponent, and A is a material-related constant. The stress exponents tended to decrease with increasing temperature with exception of the Cu_6Sn_5 particulate reinforced solder joint, which exhibited a stress exponent of 6.5 at 85°C. The stress exponents at a given temperature were found to be more or less similar, ranging from 5 to 12, which are similar to values given in other studies [12,46]. The solder joint reinforced with $FeSn_2$ particles showed the highest stress exponent values at room temperature.

Data from our prior work [92] on the same Cu_6Sn_5 composite solder joints shows substantially better creep resistance than the present study, as indicated in Figure 6.3(b). The datum points for the earlier study were obtained by unloading the specimen periodically to take micrographs of a particular scratch to quantify the shear displacement. This allowed recovery to occur that was not possible in the present study, where loading was uninterrupted. This implies that when the loading direction was reversed, recovery effects apparently reduced the mobile dislocation density that could be regenerated upon reloading, resulting in a reduction of strain over time by 2-3 orders of magnitude. When these joints were aged, the creep resistance was degraded due to the effects of coarsening the Ag_3Sn particles.

The scatter in data was related to differences in how damage accumulation developed during creep deformation. Figure 6.4 shows two representative creep curves of strain vs. time along with schematic diagrams of damage accumulation in the solder joint during creep deformation for the Ni_3Sn_4 particle reinforced solder joint crept at 85°C. The creep curve in Figure 6.4(a) shows an upward curvature for most of its lifetime, resulting in a lower creep strain before fracture, whereas the creep curve in Figure 6.4(c) exhibits the conventional downward curvature expected in the materials

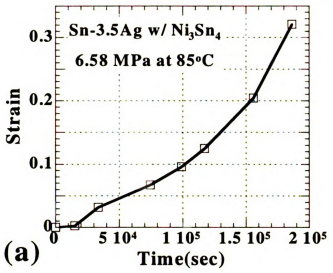

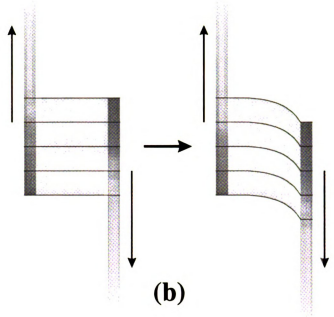

Figure 6.4 (a) & (b) Two representative creep curves and schematic diagrams illustrating different damage accumulation across the solder joint.
(a) and (b) represent inhomogeneous deformation.

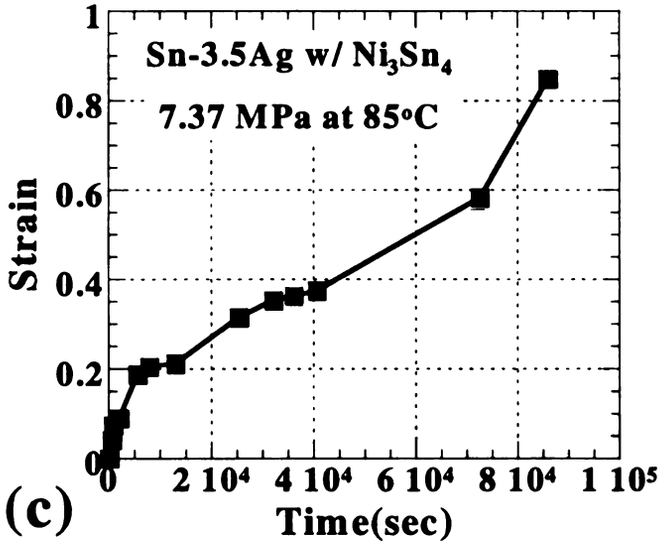

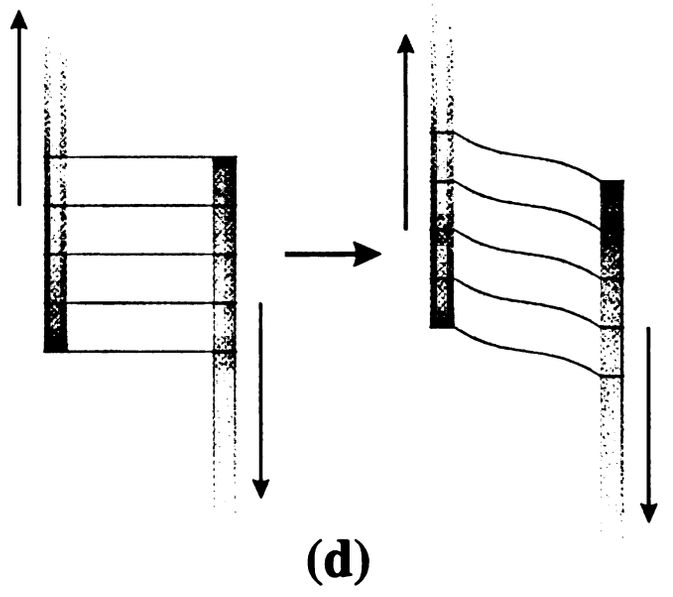

Figure 6.4 (c) & (d) Two representative creep curves and schematic diagrams illustrating different damage accumulation across the solder joint.
(c) and (d) represent homogeneous deformation.

where dislocation climb is the controlling mechanism. The difference between the two curves correlates with the different deformation history of the solder joint. The solder joint that exhibited an upward curvature in creep curve had inhomogeneous strain distribution across the joint thickness, resulting from preferential strain on one side of the solder joint as shown in Figure 6.4(b). On the other hand, the solder joint shown in Figure 6.4(d), exhibiting a downward curvature in creep curve, deformed nearly uniformly across the joint thickness. The inhomogeneous deformation in Figure 6.4(b) is thought to be influenced by undetected defects present initially in the solder joint such as porosity or a non-uniform particle distribution produced during specimen fabrication. In many cases, inhomogeneously deforming joints also showed higher minimum creep rates than specimens with more homogeneous deformation. This result points out that a better microstructural control is required to obtain consistent benefit from particle-reinforced composite solders.

Figures 6.5 (a)~(c) compare the behavior of each composite solder joint with the eutectic solder joint, and the data of Darveaux and Banerji [30] using a Dorn model for creep, which is most valid at lower normalized stresses below $\tau/G \sim 7\text{x}10^{-4}$, where power-law breakdown is not apparent.

$$\dot{\gamma} = A\frac{DGb}{kT}\left(\frac{\tau}{G}\right)^n\left(\frac{b}{d}\right)^p \quad or \quad \frac{\dot{\gamma}T}{A'G}\exp\left(\frac{+Q}{kT}\right) = \left(\frac{\tau}{G}\right)^n$$

where D is the operative diffusion process for creep with activation energy Q, G is the temperature dependent shear modulus, b is the Burgers vector, k is Boltzmann's constant, T is temperature in K, d is the grain size, n is the stress exponent, taken to be 5.5 (as used

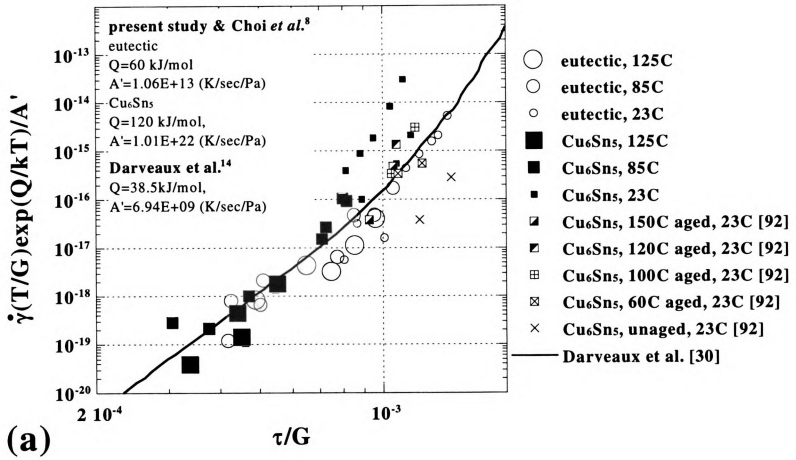

Figure 6.5(a) The normalized steady state behavior of eutectic Sn-Ag and Cu_6Sn_5 composite solder joints along with data of Choi *et al.* [92] and Darveaux & Banerji's [30].

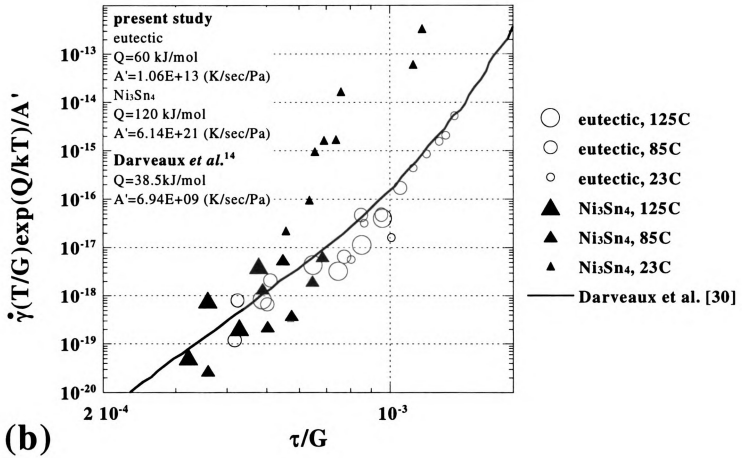

Figure 6.5(b) The normalized steady state behavior of eutectic Sn-Ag and Ni_3Sn_4 composite solder joints along with data of Darveaux & Banerji's [30].

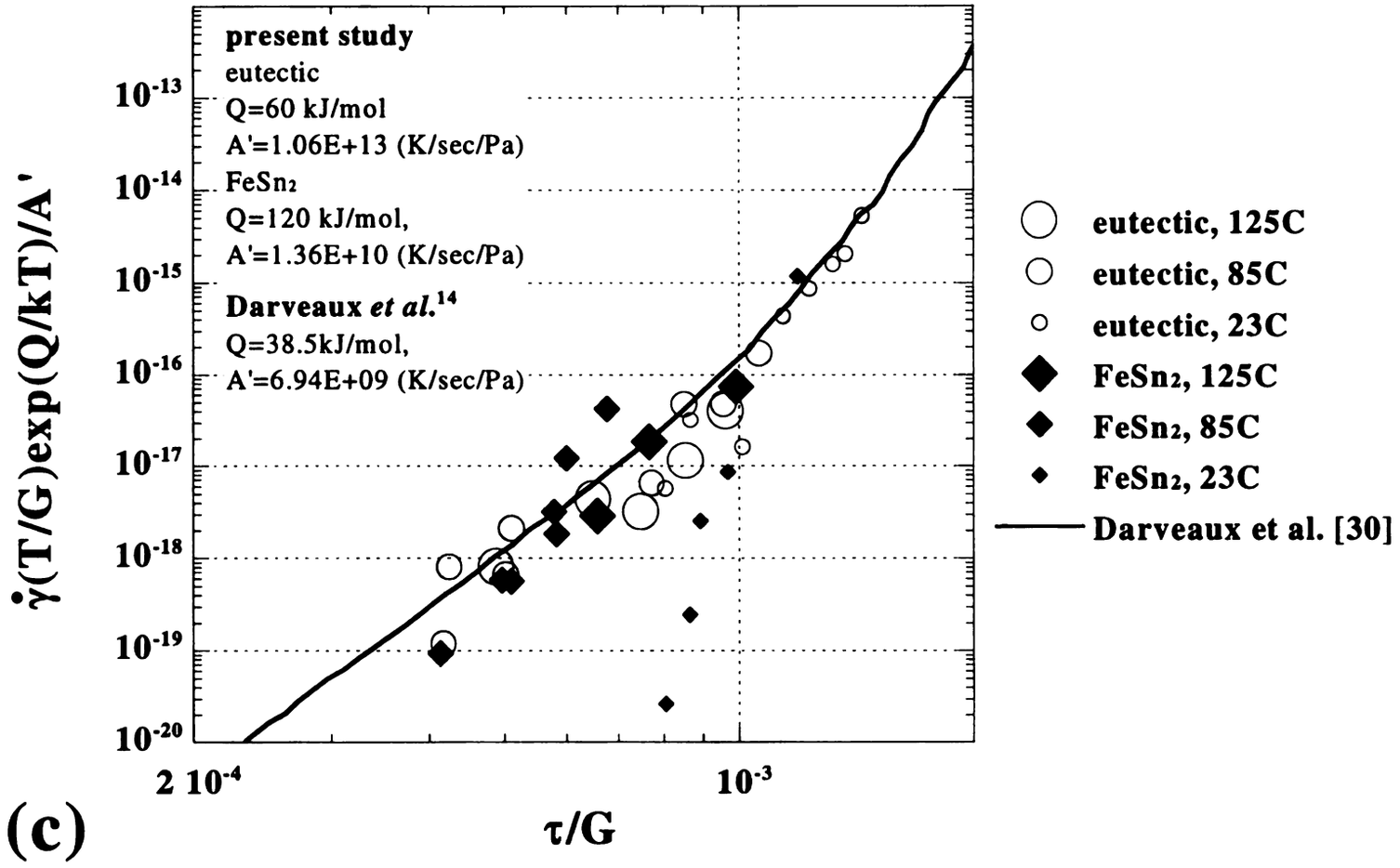

Figure 6.5(c) The normalized steady state behavior of eutectic Sn-Ag and $FeSn_2$ composite solder joints along with data of Darveaux & Banerji's [30].

by Darveaux and Banerji), p is the grain size exponent, and A is a geometrical parameter representing microstructural features. When terms that are assumed to be constant are combined into A', a set of data could be plotted using the second equation with various values of Q. The value of Q that causes the data at different temperatures to collapse onto a single line represents a good estimate of the controlling activation energy for creep. For the eutectic solder joints, a value of 60 kJ/mol caused a better fit of the data than the value of 38.5 kJ/mol used by Darveaux and Banerji. 60 kJ/mol is about half of the activation energy for tin self-diffusion [45,30], suggesting that grain boundary or pipe diffusion may control deformation of the eutectic solder joints. A value of Q=120 kJ/mol was most effective for the Cu_6Sn_5 and Ni_3Sn_4 composite solder joints, but for the $FeSn_2$ composite solder joints, Q=38.5 kJ/mol was more effective than 60 or 120 kJ/mol. Once the Q value was determined, the A' parameter could be found so that the solder joints could be compared on a uniform scale. These values are indicated in the plots in Figure 6.5 (a)~(c).

Figures 6.5 (a)~(c) show how the composite solder joints typically have the same properties as the eutectic solder joints at elevated temperatures, but not at lower temperatures. For the Cu_6Sn_5 and Ni_3Sn_4 composite solder joints, room temperature deformation appears weaker than the eutectic solder joints at equivalent normalized stresses, while the $FeSn_2$ composite solder joints are effectively stronger. This suggests that the Dorn model may be meaningful at high temperatures, but a different composite modeling strategy needs to be developed for composite solder joints at lower temperatures.

The morphology of the reinforcement particles differs among the three composite solders. Cu_6Sn_5 particles tend to be elliptical, Ni_3Sn_4 particles are angular, and $FeSn_2$ particles tend to be rounded although they exhibit irregular interface morphology. These variations imply that the mechanisms of dislocation climb over particles would be different for the three reinforcements due to different interface chemistry, geometry, and interfacial dislocation structure, and this may account for the difference in stress exponents. Since solder microstructure is very sensitive to the thermomechanical history, the variation in creep behavior may be attributed to the variation in microstructure.

Fracture of Solder Joints

A representative fracture surface of the crept solder joint is given in Figure 6.6(a), illustrating the presence of the porosities in the solder joint. The porosity within the solder joints ranged from 5 to 30 % of the total joint area. The large-scale porosity was subtracted in calculation of the actual stress applied on the solder joint since voids do not carry the load. Figure 6.6(b) shows the typical fracture surface of a solder joint crept to failure in shear. Most of the fracture surface exhibited failure by shear through the solder matrix. Thus, the fracture surface shown in Figure 6.6(b) illustrates the smeared Sn phase in the shearing direction.

In the minor areas of the fracture surface, fracture processes that included tensile as well as shear components of deformation were found. Eutectic Sn-Ag solder joints exhibited cracks along the grain boundaries of the Sn phase as shown in Figure 6.7(a), indicating that the creep strain was accommodated by intergranular separation. Spherical and elliptical dimples of Sn phase illustrated in Figure 6.7(b) were found in the fracture

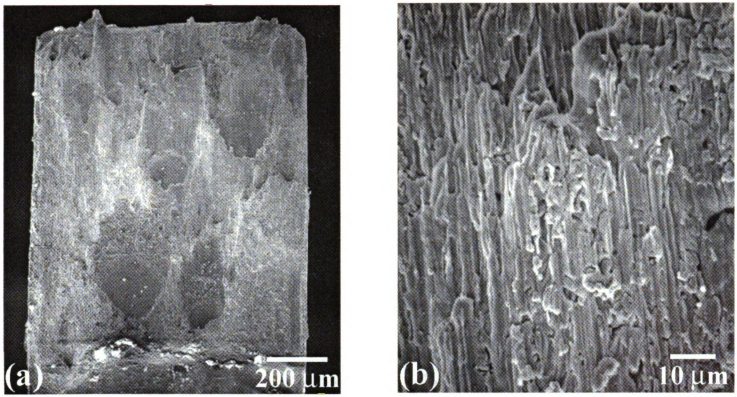

Figure 6.6 Representative fracture surface of the crept solder joint.
(a) Cu_6Sn_5 particle reinforced Sn-3.5Ag solder joint with 10.5% porosity,
(b) smeared surface due to fracture in pure shear.

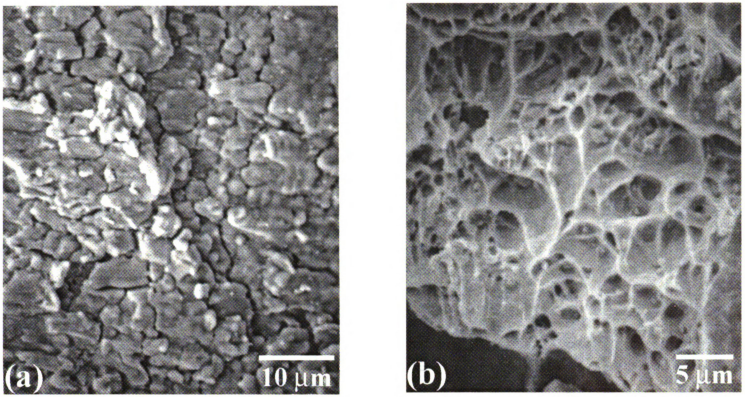

Figure 6.7 (a) & (b) SEM micrographs showing fracture processes.
(a) cracks developed along Sn-Sn grain boundaries and (b) dimples indicating ductile fracture.

surface of Ni_3Sn_4 particle reinforced solder joint crept at room temperature, indicating that this region failed in a highly ductile manner. A particle can be found at the bottom of some dimples, indicating cavity nucleation at the particle/matrix interface. Similar dimples were observed in the fracture surface of the Cu_6Sn_5 particle reinforced solder joints crept at room temperature.

Fracture by interfacial separation between Cu_6Sn_5 intermetallic interfacial layer and the solder matrix was found in very few regions. Figure 6.7(c) and (d) show the faceted surface of the Cu_6Sn_5 intermetallic layer in the fracture surface of the eutectic Sn-Ag solder joint crept at 85°C and 125°C. The exposure of the Cu_6Sn_5 intermetallic interfacial layer in the fracture surface indicates that the crack grew locally by debonding between the Cu_6Sn_5 intermetallic layer and solder matrix. The fracture surface region in Figure 6.7(c) shows complete debonding, but Figure 6.7(d) shows remaining solder ligaments indicating partial debonding. It is possible that if the solder joint fracture surface were not smeared by shear during fracture, the favored fracture processes could be observed. However, it is not easy to ascertain which is the preferred fracture process based on the complications indicated. If the overall failure process were a mixture of shear and tension, these failure modes would probably dominate the fracture surface more than the smearing shown in Figure 6.6(b). The initiation of a crack may develop by local tensile effects that are evident in Fig. 7.

6.4 SUMMARY

In this study, creep behavior of the eutectic Sn-Ag and three different types of composite solder joints were investigated. The stress exponents decreased with

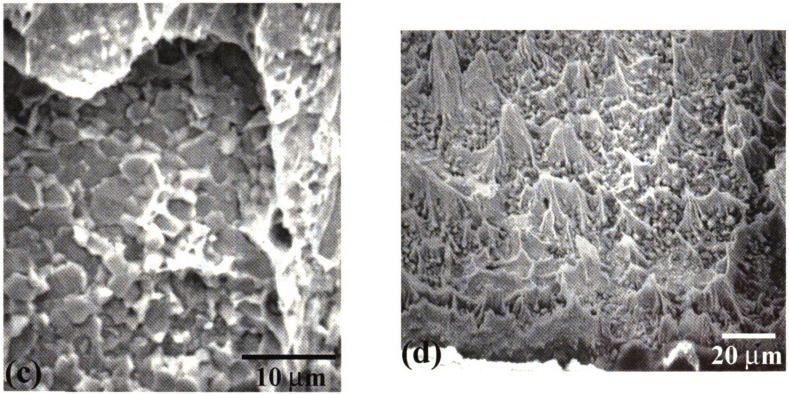

Figure 6.7 (c) & (d) SEM micrographs showing fracture processes.
(c) complete debonding of Cu_6Sn_5 interfacial layer and solder matrix, (d) partial debonding.

increasing temperature, ranging from 5 to 12. The $FeSn_2$ particle reinforced solder joint exhibited highest stress exponent values. Scatter in the data was correlated with differences in damage accumulation process during creep. The solder joints that deformed at an accelerating rate (rather than a nearly constant secondary rate) underwent inhomogeneous deformation due to a preferential strain on one side of the solder joint. This instability of the solder joint during creep in shear appeared to be due to undetected defects in the solder joint such as porosity or a non-uniform particle distribution. The solder joints reinforced with different particles exhibited different creep behavior depending upon the type of incorporated particle. Creep resistance is better if loading is cyclic rather than monotonic, so that recovery occurs during a stress reversal. All solders deformed similarly at elevated temperatures consistent with a Dorn creep model, but significant differences at room temperature indicate that appropriate composite modeling is needed at lower temperatures. Some solder joints contained regions exhibiting mixed tension and shear fracture processes such as ductile fracture identified with dimples, cracks along Sn-Sn grain boundaries, and debonding along interface between intermetallic layer and the solder matrix. However, a clear picture could not be obtained for most of the solder joint due to the rubbing of the fracture surfaces during the failure process.

CHAPTER 7

MECHANISTIC ISSUES ON CREEP STRENGTH OF SOLDER JOINTS

Creep properties of eutectic Sn-Ag and composite solder joints containing intermetallic particles have been investigated as detailed in Chapter 6. This study shows two distinct observations in creep strength of the solder joints. One is that when the solder joints experience cyclic creep deformation conducted by loading and unloading the specimen periodically, the solder joints exhibit substantially lower creep strain-rate. The other is that the composite solder joints exhibit weakening or strengthening compared to the non-composite eutectic Sn-Ag solder joints at room temperature, depending on the type of particulate reinforcement. The solder joints reinforced with either Cu_6Sn_5 or Ni_3Sn_4 particulates showed weakening, while ones reinforced with $FeSn_2$ particulates showed strengthening. In this Chapter, possible mechanistic issues that could account for the observed features in creep strength of the solder joints are discussed, to suggest future works to verify hypotheses regarding mechanistic issues that determine creep properties.

7.1 EFFECTS OF CYCLIC CREEP ON THE CREEP STRENGTH

The datum points of the Cu_6Sn_5 particle reinforced solder joints in the normalized plot, Figure 6.5(a), are reproduced in Figure 7.1 to clearly illustrate increased creep resistance in cyclic creep deformation at room temperature. It is apparent that the solder joints are more creep resistant by 2 to 3 orders of magnitude in cyclic creep conditions.

During unloading, the specimen is apparently subject to conditions similar to strain relaxation [146]. In the strain relaxation experiment, the specimen is prestrained at a

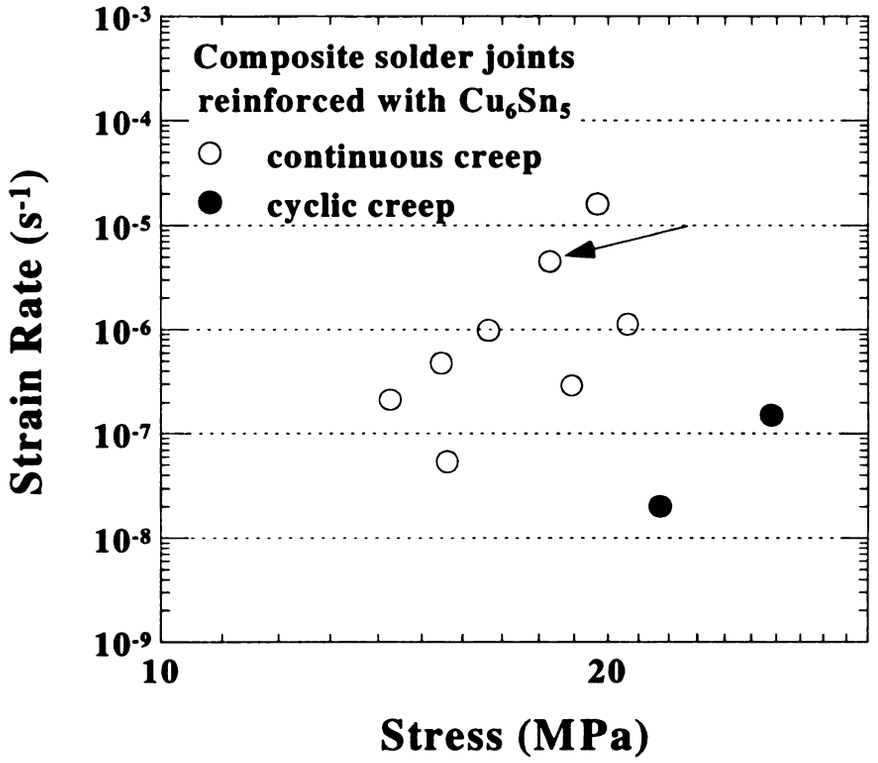

Figure 7.1 Comparison of steady state strain-rate of the Cu_6Sn_5 composite Sn-Ag solder joints for continuous and cyclic creep deformation.

fixed stress, and then rapidly unloaded. The length of the specimen is then measured with respect to time to record how the specimen shrinks. Deformation may be conveniently divided into elastic, anelastic, and plastic parts. Upon unloading, elastic strains are immediately recovered, whereas both anelastic and plastic deformation remain in materials. However, anelastic strains are recoverable with time, while plastic strains are permanent [147]. Thus, as result of unloading in the strain relaxation experiment, the elastic strain is fully relaxed, the plastic strains are static, and only the anelastic deformation causes continued strain reduction.

Eutectic Sn-37wt%Pb and Sn-2wt%Pb alloys exhibit pronounced anelastic behavior in strain relaxation experiment [148,149]. These alloys were prepared by rolling at room temperature and heat-treating to produce specimens of various grain sizes. The similar anelastic behavior in spite of large difference in composition indicates that Sn is primarily responsible for the anelasticity. In stress relaxation of the eutectic Sn-Ag and Cu_6Sn_5 reinforced composite solder joints, the % stress drop was similar in both solder joints. This indicates that Cu_6Sn_5 particles do not affect stress relaxation and only solder matrix is involved in stress relaxation behavior [150]. Since the stress relaxation is caused by deformation that reduces the internal stress within the material, strain reduction during strain relaxation may be due to similar mechanisms. The anelastic behavior of Sn is thus applicable to the eutectic Sn-Ag and composite Sn-Ag solder since the eutectic solder matrix has almost pure Sn phase containing less than 0.05% Ag. If anelastic deformation causes significant strain reduction during each unloading cyclic, this could account for the low creep strain-rate observed in cyclic creep deformation.

Another important consideration is the low melting temperature of solder materials. For solder materials, the room temperature is above half of melting temperature, indicating that the solder materials are under hot deformation condition even at ambient temperatures. It was noted that plastic strains are static in strain relaxation. However, solders may deform to behave plastically during strain relaxation due to effects of residual stress and recovery. This implies that unloading in cyclic creep allows recovery and reduces the mobile dislocation density, as the strain is reduced.

A simulation of cyclic creep using the data from continuous creep was attempted to examine the considered factors that cause strain reduction. The primary and secondary creep data for the datum point marked by an arrow in Figure 7.2 was utilized. The primary and secondary creep can be described phenomenologically by the following equation [151],

$$\varepsilon = \varepsilon_o\left(1-\exp(-\alpha t)\right)+t\dot{\varepsilon}_{ss},$$

where ε is the creep strain at time t, ε_o is the amount of primary creep strain, $\dot{\varepsilon}_{ss}$ is the secondary stage strain-rate, and α is the fitting parameter. The primary and secondary creep was best fitted with parameters of ε_o = 0.011, $\dot{\varepsilon}_{ss}$ = 4.45 x 10^{-6} /sec, and α = 0.008 /sec as shown in Figure 7.2. In the simulation of cyclic creep, an unloading event was introduced every 100 ksec and a constant 30% strain drop at each unloading were selected with the assumption that the same creep behavior as that in the continuous creep occurred with each reloading event due to application of the same stress. This choice of 30% is typical of stress relaxation in an hour [150]. Figure 7.3 shows the cyclic creep

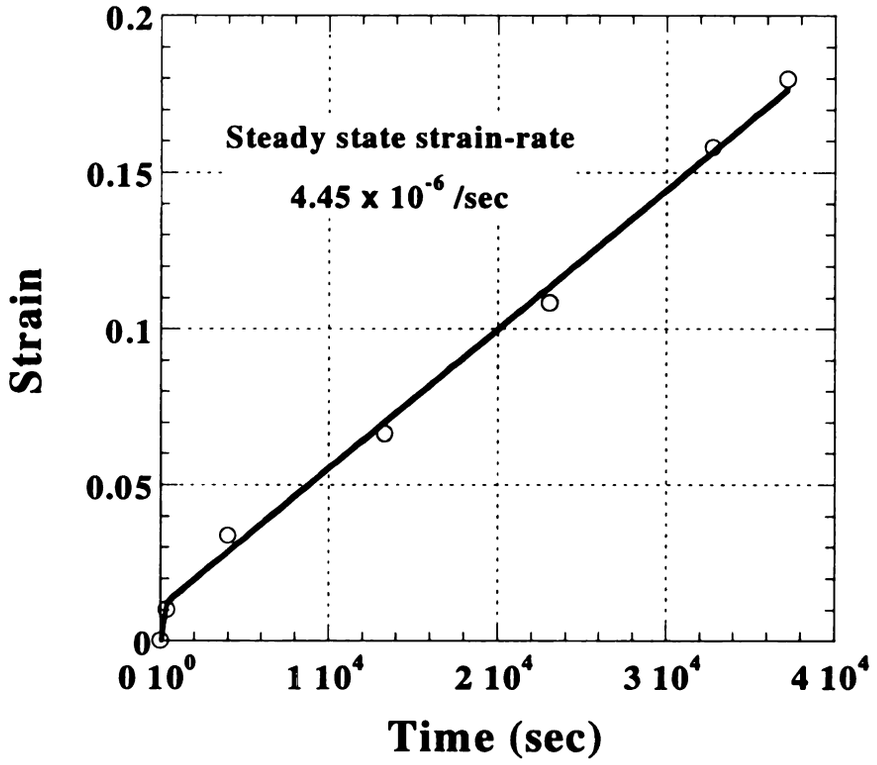

Figure 7.2 Strain vs. time curve showing primary and secondary stages of the datum point marked by an arrow in Figure 7.1.

curve obtained by connecting datum points of each strain value after the strain drop, compared with the curve for uninterrupted monotonic creep. The creep strain in cyclic creep is then expressed by this equation,

$$\varepsilon = \varepsilon_o(1-\exp(-\alpha t))+t\dot{\varepsilon}_{ss} - \varepsilon_{unloading} \ ,$$

where $\varepsilon_{unloading}$ is the 30% strain drop during unloading event.

The simulated cyclic creep curve (B in Figure 7.3) expects a lower minimum strain-rate by 2 orders of magnitude than that in monotonic creep. This indicates that the cyclic creep approach based on strain relaxation upon unloading could account for the low creep rate. However, the amount of creep strain over time is significantly larger than that observed in cyclic creep testing represented by the curve C in Figure 7.3. The strain values over time must be close to those observed in cyclic creep in order for the strain relaxation approach to be valid. This indicates that there are other operating processes that reduce the overall creep strain, since the monotonic strain-rate overpredicts the strain. Greater frequency of unloading events during cyclic creep would result in a lower cumulative creep strain. In contrast, the data in the composite solder specimen were obtained with larger time increments which would cause the model in Figure 7.3 to predict even larger cumulative strain. Furthermore, the magnitude of stress relaxation decreased with decreasing prestrain [150], and the creep strains were smaller than the prestrains used in stress relaxation. Reducing the amount of relaxation in each cycle would also move the model further from experiment.

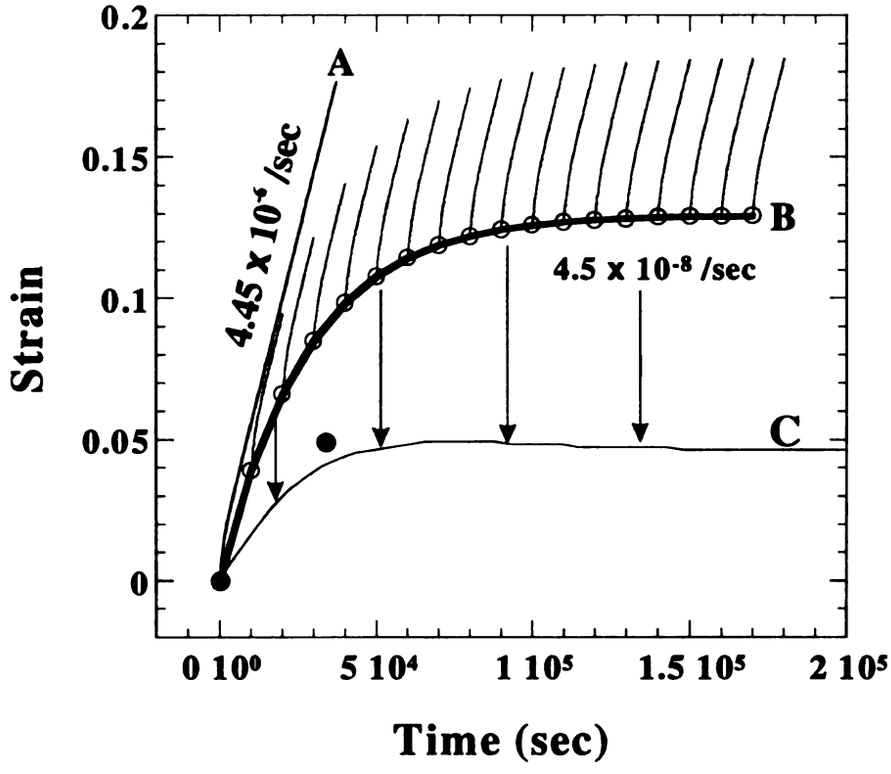

Figure 7.3 Simulated cyclic creep curve with unloading event every 10 ksec and 30% strain drop at each unloading. Curve A is one from continuous creep, curve B is the simulated cyclic creep, and curve C is the experimentally observed one.

In this simulation, it was assumed that the same creep behavior as that in monotonic creep will occur at each reloading, resulting in the same strain-rate. However, if the microstructure was not allowing the same dislocation substructure to develop, but instead changed toward increasing creep resistance due to the cyclic loading/unloading, the strain-rate during reloading would be reduced. If cyclic strain caused hardening, the strain-rate in the each subsequent reloading event would be decreased, leading to a lower strain over time than that expected with the assumption that a steady state substructure consistently developed.

The secondary stage during creep deformation proceeds by maintaining a certain balance between hardening and softening (recovery) at a given constant stress, leading to a constant strain-rate. If the recovery during unloading is small, the dislocations may accumulate with reloading, resulting in increasing dislocation density. A subgrain network consistent with climb controlled creep would form with the same stress applied, the subgrain size would be the same, but if dislocations accumulated in subgrain walls, then the misorientation would increase with each subsequent reloading. If this process leads to cumulatively larger misorientations, then grain boundary sliding could develop, resulting in large strain.

During unloading, if the subgrain network is maintained at some degree because of severely intertwined dislocations allowing small amount of recovery, it will result in smaller amount of primary strain at each subsequent reloading and secondary strain-rate stage will develop earlier. A smaller amount of primary strain at subsequent reloading was considered to be able to produce another hardening effect. However, it was found

that it did not produce any pronounced effect in the simulation of cyclic creep shown in Figure 7.3.

Tin (Sn) is known to have high elastic anisotropy. The high anisotropic property of Sn can also cause hardening effect. In a polycrystalline Sn alloy, when there are large misorientations between grains, the grain boundary must be readjusted to a new shape at reloading to accommodate strains along the grain boundary caused by the high anisotropy. The readjustment of grain boundaries can occur by generating more geometrically necessary dislocations at grain boundaries, also leading to an increase in dislocation density. Hardening can occur at room temperature since $T/T_m \cong 0.6$, and recrystallization or recovery processes may be slow, so dislocations can accumulate. This can also increase hardening at each reloading, causing smaller strain-rate at each subsequent reloading.

The processes discussed above can occur at the same time or only a single process may take place during the cyclic creep deformation. In order to verify the suggested processes, further systematic experimental study on cyclic creep should be conducted. In particular, measuring the strain reduction during unloading would provide important data on degree of anelasticity within the solder joint. Since the anelastic strains of Sn-Pb alloys measured are larger than can be predicted by existing models [149], much work on dislocation dynamics is needed before physically based models that describe Sn can be developed.

7.2 EFFECTS OF PARTICLES ON THE CREEP STRENGTH

The effects of particle reinforcement on the creep behavior were different among 3 composite solder joints, causing weakening or strengthening depending on the type of particle. Both weakening and strengthening behavior were observed in aluminum alloy depending on matrix microstructural stability and testing temperature [152]. It is not certain at present whether the particles incorporated in the eutectic Sn-Ag solder affect the microstructure of solder matrix.

The morphology of the reinforcement particle differs among the three composite solders. Cu_6Sn_5 and Ni_3Sn_4 particles tend to be smooth, whereas $FeSn_2$ particles exhibited considerable roughness. It is considered at present that the difference in interface morphology and chemistry among the particles may cause the difference in creep behavior. These variations imply that the dislocation interaction with particles would be different, and affect the motion of dislocation passing by the particles. The effect of shape could be investigated on solders reinforced by Ni-Sn intermetallic particles, as described by Fu Guo [153], that have different interface structure, but the same composition. Also important future work is to investigate the interaction between dislocation and particles with different interface property.

CHAPTER 8

SUMMARY

Deformation behavior and damage accumulation during thermomechanical fatigue were characterized using the actual eutectic Sn-Ag and Sn-4Ag-0.5Cu solder joints. The eutectic Sn-Ag and its *in-situ* composite solder joints were investigated on creep deformation and interfacial IMC layer growth. The important findings from those studies are summarized.

Microstructural studies of actual Sn-Ag or 95.5Ag/4Ag/0.5Cu solder joints that underwent 250 and 1000 thermal shock cycles between –40°C and +125°C, with a 20 minute hold time at each extreme were performed. Damages during thermomechanical fatigue initiated on the free surface and propagated through interior solder joints. The crack that would cause a catastrophic failure of solder joint occurred very near the ceramic substrate, initiating at the free surface of the solder joint and progressing inwards. Significant amount of residual stresses was observed after thermomechanical fatigue, which can cause further damage to solder joints during storage. Small amounts of copper did not have any pronounced effect on thermomechanical fatigue of Sn-Ag solder joints. Pb phase in the solder matrix also did not affect the thermomechanical fatigue behavior of the Sn-Ag solder joints.

Growth behavior of the Cu_6Sn_5 and Cu_3Sn interfacial IMC layers in the eutectic Sn-Pb and Sn-Ag, and their corresponding composite solder joints was characterized during aging at temperatures ranging 50°C to 180°C up to 5000 hours. The eutectic Sn-Pb and Sn-Ag solder matrices revealed extensive coarsening and the intermetallic layers also

grew significantly. Growth of the interfacial IMC intermetallic layers was affected several factors such as Pb-rich phase accumulation, the layer thickness itself, the aging temperature, and Cu_6Sn_5 particles. For the eutectic Sn-Pb composite solder joint, the Cu_6Sn_5 particles affected the growth of the intermetallic layers only at the initial stage of aging. However, the Cu_6Sn_5 particles did not affect the intermetallic layer growth in the Sn-Ag composite solder joint during aging at 150°C for long periods of time. The Cu_6Sn_5 particles were found to be effective in reducing the layer growth for low temperature aging, but at high temperatures above 150°C significant coarsening of the Cu_6Sn_5 particles was observed and caused the enhanced intermetallic layer growth.

The formation and growth kinetics of Cu_6Sn_5 and Cu_3Sn layers during isothermal aging up to 1400 hours were investigated in the eutectic Sn-Ag and *in-situ* composite Sn-Ag solder joints. During aging, $FeSn/FeSn_2$ and Ni_3Sn_4 particles remained stable, while Ag_3Sn particles showed significant coarsening. Voids were present only within Cu_3Sn layer due to Kirkendall effect. $FeSn/FeSn_2$ and Ni_3Sn_4 particles appeared to affect thickness of IMC layers during reflow, resulting in thinner initial interfacial IMC layer in composite solder joints. Both non-composite and composite Sn-Ag solder joints exhibited a similar behavior in the growth of IMC layers. $FeSn/FeSn_2$ and Ni_3Sn_4 particles were effective in reducing the growth of Cu_6Sn_5 layer at lower temperatures. Cu_3Sn IMC layer grew slower in composite solder joints at all temperatures.

Creep study of the eutectic Sn-Ag joints and Sn-Ag composite solder joints was carried out using single shear lap solder joints at room temperature, 85, and 125°C. Creep data of solder joints followed power law relationship over the stress ranges and temperatures employed. The stress exponents decreased with increasing temperature,

ranging from 5 to 12. Different creep behaviors were observed at room temperature depending upon the type of incorporated particle, while creep strength of the composite solder joints was similar to the eutectic Sn-Ag solder joints at high temperatures. This indicates that appropriate composite modeling is needed at lower temperatures. Creep resistance was found to be better when loading is cyclic rather than monotonic. Some solder joints exhibited mixed tension and shear fracture processes. The fracture processes were identified by dimples indicating ductile fracture, cracks along Sn-Sn grain boundaries, and debonding along interface between intermetallic layer and the solder matrix. However, the rubbing of the fracture surfaces during the failure process impeded a clear picture about fracture process of solder joints.

Mechanistic issues that may be responsible to observed cyclic creep behavior and different creep strength depending on type of reinforcement were discussed. These include anelastic strain and recovery during unloading, and change in microstructure upon reloading due to formation of subgrain network and high anisotropy of Sn. In order to verify the suggested hypotheses regarding mechanistic issues, further systematic experimental study on creep deformation of the Sn-Ag solder should be conducted.

LIST OF REFERENCES

REFERENCES

1. S. Jin, *JOM*, **45**(7), 3(1993).

2. W.L. Winterbottom, *JOM*, **45**(7), 20(1993).

3. P.T. Vianco and D.R. Frear, *JOM*, **45**(7), 14(1993).

4. C. Melton, *JOM*, **45**(7), 33(1993).

5. M. McCormack and S. Jin, *JOM*, **45**(7), 36(1993).

6. J.S. Hwang, *Modern Solder Technology for Competitive Electronic Manufacturing*, McGraw-Hill, New York, NY, 21(1996).

7. J.W. Morris, Jr., *Proceedings of the 2nd Pacific Rim International Conference on Advanced Materials and Processing*, eds. K.S. Shin *et al.*, The Korean Institute of Metals and Materials, Seoul, 715(1995).

8. W.J. Plumbridge, *J. Mater. Sci.*, Vol. 31, 2501(1996).

9. J.K. Tien, B.C. Hendrix, and A.I. Attarwala, *IEEE Transactions on Components, Hybrids, and Manufacturing Technology (CHMT)*, **12**(4), 502(1989).

10. F. Hua and J. Glazer, *Design & Reliability of Solders and Solder Interconnections*, Proceedings of a Symposium held during the TMS Annual Meeting at Orlando, FL, Feb. 10-13, 1997, The Minerals, Metals & Materials Society (TMS), Warrendale, PA, 65(1997).

11. H. Mavoori, J Chin, S. Vaynman, B. Moran, L. Keer, and M. Fine, *J. Electr. Mater.*, **26**(7), 783(1997).

12. H. Yang, P. Deane, P. Magill, and K.L. Murty, *1996 46th Electronic Components and Technology Conference (ECTC)*, IEEE, Piscataway NJ, 1136(1996).

13. S. Choi, K.N. Subramanian, J.P. Lucas, and T.R. Bieler, *J. Electr. Mater.*, **29**(10), 1249(2000).

14. S. Chada, A. Herrmann, W. Laub, R. Fournelle, D. Shangguan, and A. Achari, *Soldering & Surface Mount technology*, No. 26 July, 9(1997).

15. W. Yang, L.E. Felton, and R.W. Messler, Jr., *J. Electr. Mater.*, **24**(10), 1465(1995).

16. W. Yang, R.W. Messler, Jr., and L.E. Felton, *J. Electr. Mater.*, **23**(8), 765(1994).

17. W.B. Hampshire, *Soldering & Surface Mount Technology*, No. 14 June, 49(1993).

18. J. Glazer, *Int. Mater. Rev.*, **40**(2), 65(1995).

19. M. Abtew, G. Selvaduray, *Mater. Sci. & Eng.*, Vol. R27, 95(2000).

20. M. Ohring, *Reliability and Failure of Electronic Materials and Devices*, Academic Press, Chestnut Hill, MA, 439(1998).

21. M. McCormack and S. Jin, *1994 IEEE/CPMT 16th Int'l Electronics Manufacturing Technology Symposium, Vol. 1*, IEEE, Piscataway NJ, 7(1994).

22. W. Steurer, R. Ferro, and A. Saccone, *Physical Metallurgy 4th ed.*, Vol. 1, eds. R.W. Cahn and P. Haasen, Elsevier Science B.V., Amsterdam, The Netherlands, 25 & 284(1996).

23. C.W. Fairhurst and J.B. Cohen, *Acta Cryst.*, Vol. B28, 371(1972).

24. *Metals Handbook 9th ed.*, Vol. 9, ASM, Metals Park, OH, 455(1985).

25. A.W. Gibson, S.L. Choi, K.N. Subramanian, T.R. Bieler, *Design & Reliability of Solders and Solder Interconnections*, Proceedings of a Symposium held during the TMS Annual Meeting, The Minerals, Metals & Materials Society (TMS), Warrendale, PA, 97(1997).

26. A.W. Gibson, S. Choi, T.R. Bieler, and K.N. Subramanian, *IEEE Int'l Symposium on Electronics & the Environment*, IEEE, Piscataway, NJ, 246(1997).

27. W.D. Callister, Jr., *Materials Science and Engineering An Introductio*n 4th ed., John Wiley & Sons, Inc., New York, 220(1997).

28. R. Arrowood, A. Mukherjee, and W.B. Jones, *Solder Mechanics A State of the Art Assessment*, eds. D.R. Frear *et al.*, The Minerals, Metals & Materials Society (TMS), Warrendale, PA, 108(1991).

29. R.W. Evans and B. Wilshire, *Introduction to Creep*, The Institute of Materials, London, 20(1993).

30. R. Darveaux and K. Banerji, *1992 42nd Electronic Components and Technology Conference (ECTC)*, IEEE, Piscataway NJ, 538(1992).

31. G.E. Dieter, *Mechanical Metallurgy 3rd ed.*, McGraw-Hill Inc., 445(1986).

32. M.A. Meyers and K.K. Chawla, *Mechanical Metallurgy principles and applications*, Prentice-Hall Inc., Englewood Cliffs, NJ, 667(1984).

33. R. Arrowood, A. Mukherjee, and W.B. Jones, *Solder Mechanics A State of the Art Assessment*, eds. D.R. Frear *et al.*, The Minerals, Metals & Materials Society (TMS), Warrendale, PA, 111(1991).

34. R.W. Evans and B. Wilshire, *Introduction to Creep*, The Institute of Materials, London, 45(1993).

35. G.E. Dieter, *Mechanical Metallurgy 3rd ed.*, McGraw-Hill Inc., 446(1986).

36. R.W. Evans and B. Wilshire, *Introduction to Creep*, The Institute of Materials, London, 46(1993).

37. R.W. Evans and B. Wilshire, *Introduction to Creep*, The Institute of Materials, London, 47(1993).

38. F.A. Mohamed and T.G. Langdon, *Phil. Mag.*, Vol. 32, 697(1975).

39. P.L. Hacke, A.F. Sprecher, and H. Conrad, *Thermal Stress and Strain in Microelectronics Packaging*, eds. J.H. Lau, Van Nostrand Reinhold, New York, NY, 472(1993).

40. T.G. Langdon and F.A. Mohamed, *Scripta Metall.*, Vol. 11, 575(1977).

41. R. Arrowood, A. Mukherjee, and W.B. Jones, *Solder Mechanics A State of the Art Assessment*, eds. D.R. Frear *et al.*, The Minerals, Metals & Materials Society (TMS), Warrendale, PA, 119(1991).

42. R.W. Evans and B. Wilshire, *Introduction to Creep*, The Institute of Materials, London, 59(1993).

43. M.A. Meyers and K.K. Chawla, *Mechanical Metallurgy principles and applications*, Prentice-Hall Inc., Englewood Cliffs, NJ, 672(1984).

44. R.W. Evans and B. Wilshire, *Introduction to Creep*, The Institute of Materials, London, 61(1993).

45. M.D. Mathew, S. Movva, and K.L. Murty, *Key Engineering Materials*, Vol. 171-174, 655(2000).

46. J. Liang, P.S. Lee, N. Gollhardt, S. Schroeder, and W. Morris, *Mat. Res. Soc. Symp. Proc.*, Vol. 445, 307(1997).

47. C.H. Raeder, G.D. Schmeelk, D. Mitlin, T. Barbieri, and W. Yang, *1994 IEEE/CPMT Int'l Electronics Manufacturing Technology Symposium*, IEEE, Piscataway NJ, 1(1994).

48. D.R. Frear, *JOM*, **48**(5), 49(1996).

49. J.E. Breen and J. Weertman, *J. of Metals*, Vol. 7, 1230(1955).

50. F.A. Mohamed, K.L. Murty, J.W. Morris, Jr., *Metall. Trans.*, Vol. 4, 935(1973).

51. M. Harada and R. Satoh, *IEEE Transactions on Components, Hybrids, and Manufacturing Technology (CHMT)*, **13**(4), 736(1990).

52. V.I. Igoshev, J.I. Kleiman, *J. Electr. Mater.*, **29**(2), 244(2000).

53. V.I. Igoshev, J.I. Kleiman, D. Shangguan, C. Lock, S. Wong, and M. Wiseman, *J. Electr. Mater.*, **27**(12), 1367(1998).

54. W.D. Callister, Jr., *Materials Science and Engineering An Introductio*n 4th ed., John Wiley & Sons, Inc., New York, 203(1997).

55. G.E. Dieter, *Mechanical Metallurgy 3rd ed.*, McGraw-Hill Inc., 377(1986).

56. M.A. Meyers and K.K. Chawla, *Mechanical Metallurgy principles and applications*, Prentice-Hall Inc., Englewood Cliffs, NJ, 691(1984).

57. M.A. Meyers and K.K. Chawla, *Mechanical Metallurgy principles and applications*, Prentice-Hall Inc., Englewood Cliffs, NJ, 692(1984).

58. G.E. Dieter, *Mechanical Metallurgy 3rd ed.*, McGraw-Hill Inc., 378(1986).

59. M.A. Meyers and K.K. Chawla, *Mechanical Metallurgy principles and applications*, Prentice-Hall Inc., Englewood Cliffs, NJ, 689(1984).

60. G.E. Dieter, *Mechanical Metallurgy 3rd ed.*, McGraw-Hill Inc., 379(1986).

61. M.A. Meyers and K.K. Chawla, *Mechanical Metallurgy principles and applications*, Prentice-Hall Inc., Englewood Cliffs, NJ, 695(1984).

62. M.A. Meyers and K.K. Chawla, *Mechanical Metallurgy principles and applications*, Prentice-Hall Inc., Englewood Cliffs, NJ, 697(1984).

63. G.E. Dieter, *Mechanical Metallurgy 3rd ed.*, McGraw-Hill Inc., 393(1986).

64. M. Kitano, T. Shimizu, T. Kumazawa, and Y. Ito, *Current Japanese Materials Res.*, Vol. 2, 235(1987).

65. H. Mavoori, S. Vaynman, J Chin, B. Moran, L.M. Keer, and M.E. Fine, *Mat. Res. Soc. Symp. Proc.*, Vol. 390, 161(1995).

66. S. Vaynman, M.E. Fine, and D.A. Jeannotte, *Solder Mechanics A State of the Art Assessment*, eds. D.R. Frear *et al.*, The Minerals, Metals & Materials Society (TMS), Warrendale, PA, 155(1991).

67. J.S. Hwang, *Modern Solder Technology for Competitive Electronic Manufacturing*, McGraw-Hill, New York, NY, 513(1996).

68. S. Vaynman, M.E. Fine, and D.A. Jeannotte, *Solder Mechanics A State of the Art Assessment*, eds. D.R. Frear *et al.*, The Minerals, Metals & Materials Society (TMS), Warrendale, PA, 156(1991).

69. S. Vaynman, M.E. Fine, and D.A. Jeannotte, *Solder Mechanics A State of the Art Assessment*, eds. D.R. Frear *et al.*, The Minerals, Metals & Materials Society (TMS), Warrendale, PA, 159(1991).

70. D.R. Frear, *Solder Mechanics A State of the Art Assessment*, eds. D.R. Frear *et al.*, The Minerals, Metals & Materials Society (TMS), Warrendale, PA, 193(1991).

71. S. Vaynman, M.E. Fine, and D.A. Jeannotte, *Solder Mechanics A State of the Art Assessment*, eds. D.R. Frear *et al.*, The Minerals, Metals & Materials Society (TMS), Warrendale, PA, 195(1991).

72. W. Englemaier, *Circuit World*, Vol. 11, 61(1985).

73. D. Tribula, D. Grivas, D.R. Frear, and J.W. Morris, Jr., *Welding Res. Supp. in Welding Journal*, Oct., **68**(10), 404s(1989).

74. D.R. Frear, *Solder Mechanics A State of the Art Assessment*, eds. D.R. Frear *et al.*, The Minerals, Metals & Materials Society (TMS), Warrendale, PA, 201(1991).

75. H.D. Solomon, *J. Electr. Packaging*, Vol. 113 June, 102(1991).

76. Z. Guo, A.F. Sprecher, Jr., H. Conrad, and M. Kim, *Materials Developments in Microelectronic Packaging : Performance and Reliability, Proceedings of the Fourth Electronic Materials and Processing Congress*, eds. P.J. Singh, ASM, 155(1991).

77. H. Mavoori, S. Vaynman, J Chin, B. Moran, L.M. Keer, and M.E. Fine, *Mechanics and Materials for Electronic Packaging : Vol. 1 – Design and Process Issues in Electronic Packaging*, Proceedings of 1994 International Mechanical Engineering Congress and Exposition, eds. W.T. Chen *et al.*, ASME, New York, 165(1994).

78. H. Mavoori and J. Chin, *1992 45th Electronic Components and Technology Conference (ECTC)*, IEEE, Piscataway NJ, 990(1992).

79. D. Shangguan, *Soldering & Surface mount Technology*, **11**(3), 27(1999).

80. D. Shangguan and A. Achari, *1994 IEEE/CPMT Int'l Electronics Manufacturing Technology Symposium*, IEEE, Piscataway NJ, 25(1994).

81. P.G. Harris, K.S. Chaggar, *Soldering & Surface Mount Technology*, **10**(3), 38(1998).

82. D.R. Frear, P.T. Vianco, *Metall. & Mater. Trans A*, Vol. 25A July, 1509(1994).

83. J. London and D.W. Ashall, Brazing and Soldering, no. 11, 49(1986).

84. H.D. Blair, T.Y. Pan, J.M. Nicholson, R.P. Cooper, S.W. Oh, A.R. Farah, *1996 IEEE/CPMT Int'l Electronic Manufacturing Technology Symposium*, IEEE, Piscataway, NJ, 282(1996).

85. G. Lucey, J. Marshall, C. Handwerker, D. Tench, and A. Sunwoo, *Proceedings of the Technical Program*, vol. 1, presented at National Electronic Packaging and Production Conference (NEPCON) WEST 91, Cahner Exhibition Group, Des Plains, IL, 3(1991).

86. W.K. Choi and H.M. Lee, *J. Electr. Mater.*, **29**(10), 1207(2000).

87. R.J. Field, S.R. Row, and G.K. Lucey, Jr., *The Metal Science of Joining*, eds. M.J. Cieslak *et al.*, The Minerals, Metals & Materials Society (TMS), Warrendale, PA, 165(1991).

88. H.P.R. Frederikse, R.J. Field, and A. Feldman, *J. Appl. Phys.*, 72(7), 2879(1991).

89. R.F. Pinizzotto, Y. Wu, E.G. Jacobs, and L.A. Foster, *Proceedings of the Technical Program*, vol. 3, presented at National Electronic Packaging and Production Conference (NEPCON) WEST 92, Cahner Exhibition Group, Des Plains, IL, 1284(1992).

90. Y. Wu, J.A. Sees, C. Pouraghabagher, L.A. Foster, J.L. Marshall, E.G. Jacobs, and R.F. Pinizzotto, *J. Electr. Mater.*, **22**(7), 769(1993).

91. D.R. Flanders, E.G. Jacobs, R.F. Pinizzotto, *J. Electr. Mater.*, **26**(7), 883(1997).

92. S.L. Choi, A.W. Gibson, J.L. McDougall, T.R. Bieler, and K.N. Subramanian, *Design & Reliability of Solders and Solder Interconnections*, Proceedings of a Symposium held during the TMS Annual Meeting, The Minerals, Metals & Materials Society (TMS), Warrendale, PA, 241(1994).

93. C.G. Guo, S.M.L. Sastry, and K.L. Jerina, *Microstructural and Mechanical Properties of Aging Material*, Proceedings eds. P.K. et al., The Minerals, Metals & Materials Society (TMS), Warrendale, PA, 409(1993).

94. C.G. Guo, S.M.L. Sastry, and K.L. Jerina, *Microstructural and Mechanical Properties of Aging Material*, Proceedings eds. P.K. et al., The Minerals, Metals & Materials Society (TMS), Warrendale, PA, 417(1993).

95. W.J. Tomlinson and N.J. Bryan, *J. Mater. Sci.*, Vol. 21, 103(1986).

96. C.T. Ho and D.D.L. Chung, *J. Mater. Res.*, **5**(6), 1266(1990).

97. J.L. Marshall, J. Calderon, J. Sees, G. Lucey, and J.S. Hwang, *IEEE Transactions on Components, Hybrids, and Manufacturing Technology (CHMT)*, **14**(4), 698(1991).

98. H.S. Betrabet, S.M. McGee, and J.K. McKinlay, *Scripta Metall. Mater.*, vol. 25, 2323(1991).

99. J.A. Wasynczuk and G.K. Lucey, *Proceedings of the Technical Program*, vol. 3, presented at National Electronic Packaging and Production Conference (NEPCON) WEST 92, Cahner Exhibition Group, Des Plains, IL, 1245(1992).

100. R.B. Clough, R. Patel. J.S. Hwang, and G. Lucey, *Proceedings of the Technical Program*, vol. 3, presented at National Electronic Packaging and Production Conference (NEPCON) WEST 92, Cahner Exhibition Group, Des Plains, IL, 1256(1992).

101. S.M.L. Sastry, T.C. Peng, R.J. Lederich, K.L. Jerina, and C.G. Kuo, *Proceedings of the Technical Program*, vol. 3, presented at National Electronic Packaging and Production Conference (NEPCON) WEST 92, Cahner Exhibition Group, Des Plains, IL, 1266(1992).

102. H.S. Betrabet and S. McGee, *Proceedings of the Technical Program*, vol. 3, presented at National Electronic Packaging and Production Conference (NEPCON) WEST 92, Cahner Exhibition Group, Des Plains, IL, 1276(1992).

103. J.L. Marshall, J. sees, and J. Calderon, *Proceedings of the Technical Program*, vol. 3, presented at National Electronic Packaging and Production Conference (NEPCON) WEST 92, Cahner Exhibition Group, Des Plains, IL, 1278(1992).

104. J.L. Marshall and J. Calderon, *Soldering & Surface Mount Technology*, no. 26, July, 22(1997).

105. J.L. Marshall and J. Calderon, *Soldering & Surface Mount Technology*, **9**(3), 6(1997).

106. J.L. Marshall and J. Calderon, *Soldering & Surface Mount Technology*, **9**(3), 11(1997).

107. C.M. Miller, I.E. Anderson, and J.F. Smith, *J. Electr. Mater.*, **23**(7), 595(1994).

108. K.F. Seeling and D.G. Lockard, US Patent Number 5 405 577, (1995).

109. Y. Kariya, Y. Hirata, and M. Otsuka, *J. Electr. Mater.*, **28**(11), 1263(1999).

110. Y.H. Pao, S. Badgley, R. Govila, and E. Jih, *Fatigue of Electronic Materials*, ASTM STP 1153, S.A. Schroeder and M.R. Mitchell, Eds., ASTM, Phil. PA, 60(1994).

111. R.K. Govila, E. Jih, Y.H. Pao, and C. Larner, *J. Electron. Packaging*, **116**, 83(1994).

112. Y.H. Pao, E. Jih, V. Siddapureddy, X. Song, and R. Liu, *Sensing, Modeling and Simulation in Emerging Electronic Packaging*, 1996 ASME Int'l Mechanical Engineering Congress and Exposition, Nov 17-22, 1996 Atlanta, GE, 1(1996).

113. D.R. Frear, D. Grivas, and J.W. Morris, Jr., *JOM*, **40**, 18(1988).

114. D.R. Frear, D. Grivas, and J.W. Morris, Jr., *J. Electr. Mater.*, **17**, 171(1988).

115. H. Mavoori and J. Chin, *1995 IEEE 45th ECTC*, 990(1995).

116. W. Engelmaier, *Design & Reliability of Solders and Solder Interconnections*, Proceedings of a Symposium held during the TMS Annual Meeting, The Minerals, Metals & Materials Society (TMS), Warrendale, PA, 9(1997).

117. W. Englemaier and A.I. Attarwala, *IEEE Trans. on CHMT*, **12**, 284(1989).

118. H.J. Frost and R.T. Howard, *IEEE Trans. on CHMT*, **13**, 727(1990).

119. T.Y. Pan, *J. Electronic Packaging*, **116**, 163(1994).

120. P.L. Hacke, A.R. Sprecher, and H. Conrad, *Thermomechanical Fatigue Behavior of Materials*, ASTM STP 1186, H. Sehitoglu, ed. ASTM, Phil. PA, 91(1993).

121. Q. Guo, E.C. Cutiongco, L.M. Keer, and M.E. Fine, *J. Electronic Packaging*, **114**, 145(1992).

122. Z. Guo and H. Conrad, *J. Electronic Packaging*, **118**, 49(1996).

123. C.H. Raeder, R.W. Messler, and L.F. Coffin, *J. Electr. Mater.*, **28,** 1045(1999).

124. P.T. Vianco, S.N. Burchett, M.K. Nielsen, J.A. Rejent, and D.R. Frear, *J. Electr. Mater.*, **9,** 1290(1999).

125. R.L. Schalek and L.T. Drzal, *ASM Advanced Materials & Processes*, **152**(1), 21(1997).

126. A. Gickler, C. Willi, and M. Loomans, *Surface Mount Technology*, **11**(11), 44(1997).

127. K.W. Moon, U.R. Kattner, W.J. Boetinger, and C.A. Handwerker, *Abstract in Final Program*, The Minerals, Metals & Materials Society (TMS) Fall Meeting, Cincinnati, OH, 32(1999).

128. L.G. Earle, *J. Inst. Metals*, **72**, 403(1946).

129. Z. Mei, P. Callery, D. Fisher, F. Hua, and J. Glazer, ASME *Advances in Electronic Packaging*, 2, 1543(1997).

130. Z. Mei, M Kaufmann, A. Eslambolchi, and P. Johnson, *1998 IEEE 48th ECTC*, 952(1998).

131. Z. Mei, P. Johnson, M. Kaufmann, and A. Eslambolchi, *1999 IEEE 49th ECTC*, 125(1995).

132. S. Jadhav, private communication.

133. A.J. Sunwoo, J.W. Morris, Jr., and G.K. Lucey, Jr., *Metall. Trans.*, **23A**, 1323(1992).

134. K.N. Tu, *Acta Metall.* **21**, 347(1973).

135. D. Grivas, D. Frear, L. Quan, and J.W. Morris, Jr., *J. Elect. Mater.*, **15**, 355(1986).

136. Z. Mei, A.J. Sunwoo, and J.W. Morris, Jr., *Metall. Trans.*, **23A**, 857(1992).

137. R.F. Pinizzotto, Y. Wu, E.G. Jacobs, and L.A. Foster, *Proc. Tech. Program, NEPCON West 92*, Feb 23-27, Anaheim, CA, 3(1992).

138. M.E. Warwick and S.J. Muckett, *Circuit World*, **9**, 5(1983).

139. J.O.G. Parent, D.D.L. Chung, and I.M. Berstein, *J. Mater. Sci.*, **23**, 2564(1988).

140. S.F. Dirnfeld and J.J. Ramon, *Weld. J. Res. Suppl.*, 373s(1990).

141. S. Choi, T.R. Bieler, J.P. Lucas, and K.N. Subramanian, *J. Elect. Mater.*, **28**(11), 1209(1999).

142. *Binary Alloy Phase Diagrams*, vol. 1, ed., T.B. Massalski, (Metals Park, OH : American Society for Metals), 1774(1986).

143. B.P. Richards, C.L. Levoguer, C.P. Hunt, K. Nimmo, S. Peters, and P. Cusack, "Lead-Free Soldering", UK's Department of Trade and Industry (DTI) publication, (1999).

144. J.P Lucas, F. Guo, J. McDougall, T.R. Bieler, K.N. Subramanian, and J.K. Park, *J. Electr. Mater.*, **28**(11), 1268(1999).

145. J. McDougall, S. Choi, T.R. Bieler, K.N. Subramanian, J.P. Lucas, *Mater. Sci. Eng.*, **A285**, 25(2000).

146. J.H. Schneibel and P.M. Hazzledine, *Scripta Metall.,* Vol. 11, 953(1977).

147. G.E. Dieter, *Mechanical Metallurgy 3rd ed.*, McGraw-Hill Inc., 434(1986).

148. C. Homer and B. Baudelet, *Scripta Metall.,* Vol. 11, 185(1977).

149. J.H. Schneibel and P.M. Hazzledine, *Acta Metall.,* Vol. 30, 1223(1982).

150. S.G. Jadhav, T.R. Bieler, K.N. Subramanian, and J.P. Lucas, *J. Electr. Mater.*, 30(9), 1197(2001).

151. Dongyi Seo, Ph.D. Dissertation, Michigan State University, 86(1998).

152. P. E. Krajewski, *Deformation, Processing, and Properties of Structural Materials*, Proceedings of a Symposium held during the TMS Annual Meeting, The Minerals, Metals & Materials Society (TMS), Warrendale, PA, 207(2000).

153. F. Guo, Ph.D. Dissertation, Michigan State University, (2002).